GPS Precise Positioning using Multisensor Data Fusion for Vehicular Communication

Jiachen Yin

School of Engineering

Newcastle University

A thesis submitted for the degree of

Doctor of Philosophy

September 2019

Abstract

The Global Positioning System (GPS) is a widely used timing, navigation and positioning system. However, its performance can be significantly degraded by the effects of the various sources of noises due to a highly dynamic multipath environment, signal blockage or attenuation due to ionospheric perturbation. Therefore, the aim of this research is to enhance the GPS signal acquisition and tracking ability to mitigate these effects. Furthermore, it is desirable to provide continuous and consistent positioning information under GPS-denied environments with assistance from multi-sensor data fusion techniques. In this thesis, a novel GPS signal acquisition approach for very dense multipath environments, using a low cost innovative dual polarization patch antenna attached to GPS receiver, is implemented. This reduces the acquisition processing time significantly compared to the conventional serial searching approach. Furthermore, it successfully acquires extra satellites in a dense multipath environment.

Furthermore, the GPS signal carrier tracking loop has been considered as one of the most important links in order to demodulate the navigation data frame. An innovative carrier tracking loop is also proposed that comprises two approaches, namely, the adaptive Kalman filter and the adaptive unscented Kalman filter, dynamically integrated with a third order phased locked loop respectively. The proposed two-carrier tracking loops are compared against the conventional carrier tracking loop and the results prove that the proposed approach is more robust and accurate. The carrier tracking performance employing this novel approach is improved, especially in highly dynamic and low CNR environments.

Finally, in order to integrate GPS and the sensors, GPS, IMU (inertial measurement unit) and LiDAR are combined for data fusion. A novel line feature extraction and mapping algorithm was designed for

LiDAR navigation with a low complexity that resulted in faster feature extraction. This was followed by an innovative integration scheme that combined GPS, IMU and LiDAR, which resulted in continuous, precise positioning data for vehicular communication, even when GPS signals are not available, in a harsh multipath environment.

Acknowledgements

Firstly, I would like to express my sincere gratitude to my supervisor Dr Rajesh Tiwari for the continuous support of my Ph.D study and related researching work, for his patience, motivation, and immense knowledge. His guidance helped me in all the time of research and writing of this thesis. His careful and professional editing contributed enormously to the production of this thesis.

I also thank Dr. Martin Johnston, for the academic support to carry out the research work. Dr Johnston has been very encouraging and supportive during my Ph.D studing life, and I express my gratitude to him.

I would appreciate Prof. Satnam Dlay, who took keen interest on my project work and guided me all along, till the completion of this project. I am extremely thankful to him for providing such a nice support and guidance.

The thesis would not have come to a successful completion without the help from the staff of the Electronic Lab. I would like to thank Paul and his colleagues, for their services in circuit design and equipment support.

My colleagues, Haicang Li, Handong Li, Scott Stainton, Yulong Chen, Zeyu Fu, Yang Sun, Yang Xian, Jiawei Yan have all extended their support in a very special way, and I gained a lot from them, through their personal and scholarly interactions, their suggestions at various points of my research program. I also acknowledge my old colleagues Zhen Mei and Yuanyi Zhao, for their best wishes.

I would like to express my gratitude and appreciation to my parents, who give me unconditional love and encourage me in my whole life, their support make all this happened since the beginning.

I would especially thanks to my wife, Suyi Li who has been extremely supportive of my entire PhD researching life and has made countless sacrifices to help me to this point.

Contents

List of Figures

List of Tables

List of Acronyms & Symbols

Symbols

α	Spread of sigma points UT process
β	Sharing Factor
κ	Scaling factor of UKF process
λ	Longitude
ω	Angular Velocity
ω_{ab}^{b}	Angular velocity of frame b with respect a represented in frame b
ϕ	Roll
ψ	Yaw
θ	Pitch
φ	Latitude
ξ	Innovation Sequence
B_n	Tracking Bandwidth
f_d	Doppler Frequency Shift
h	Height
R_m	Radii of Curvature in Meridian
R_n	Prime Vertical

Acronyms/Abbreviations

AKF	Adaptive Kalman Filter

BPSK	Binary Phase Shift Keying
C/A Code	Coarse Acquisition Code
CDMA	Code Division Multiple Access
CNR	Carrier to Noise Ratio
DCO	Digital Control Oscillator
DSSS	Direct Signal Spread Spectrum
ECEF	Earth Center Earth Fixed
ECI	Earth Center Inertial
EKF	Extended Kalman Filter
ENU	East North Up
FFT	Fast Fourier Transform
FLL	Frequency Lock Loop
GNSS	Global Navigation Satellite System
GPS	Global Position System
HOW	Hand Over word
IF	Intermediate Frequency
IMU	Inertial Measurement Unit
INS	Inertial Navigation Sensor
ITS	Intelligent Transport System
KF	Kalman Filter
LFSR	Linear Feedback Shift Register
LHCP	Left Hand Circular Polarization
LiDAR	Light Detection and Range
LMS	Least Mean Square

NCO	Numerical Control Oscillator
PLI	Phase Lock Indicator
PLL	Phase Lock Loop
RHCP	Right Hand Circular Polarization
RINEX	Receiver Independent Exchange Format
RMSE	Root Mean Square Error
SNR	Signal to Noise Ratio
TLM	Telemetry
UKF	Unscented Kalman Filter
USRP	Universal Software Radio Peripheral
V2V	Vehicle to Vehicle
VSWR	Voltage Standing Wave Ratio

Chapter 1

Introduction

1.1 Introduction

Precise and accurate location and navigation has been in demand throughout mankind's history. As can be seen in Figure 1.1, the earliest navigation approaches date back to around 3000BC, where for around 2000 years they observed the sun, stars, or landmarks in order to decide the direction and the distance. The compass was a revolutionary navigation device, invented in 206 BC, and after more than 1000 years, the compass is still used in sailing navigation and even today the digital compass is still familiar in many transportation systems as an aiding tool. In recent history, when the US launched 11 satellites in the period between 1978 to 1985, satellite based navigation schemes started to play a more dominant role in navigation. Now there are more than 100 satellites in space at any one time that aim to provide navigation, location and timing services anytime and anywhere. Nowadays, many applications depend on location and navigation such as aviation, sailing, road transportation and construction. As is almost always the case, opportunity comes hand in hand with challenge, this is the best era for navigation technology development and precise and accurate navigation performance is in demand more than ever before.

In this section, the background and the motivation of this research are provided such as the importance and the challenge of satellite navigation signal acquisition and tracking to GPS navigation. Furthermore, due to the limitation of satellite navigation, the importance of multisensor data fusion is also presented. The overview of the current approaches and their drawbacks are also discussed in this section. Finally, the outline of this thesis will be presented at the end of this section.

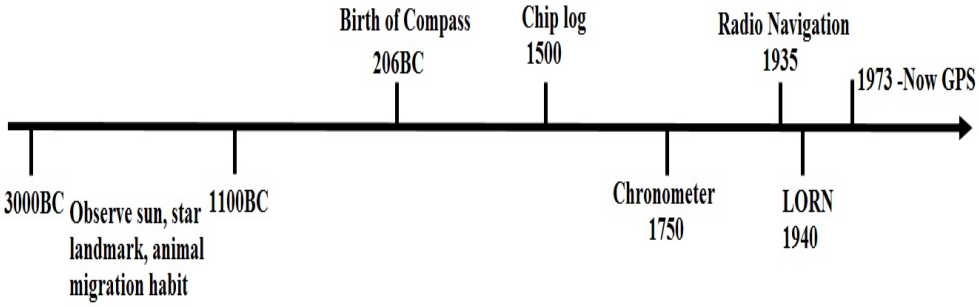

Figure 1.1: Evolution of Navigation

1.2 Background

Calculating the total number of vehicles in the world is an inexact science, however based on factory analysis, this number reached 1.2 billion in 2014 and is growing rapidly. By 2035, this number is estimated to be in excess of 2 billion. Because of the large number of vehicles on the road traffic systems become inefficient and dangerous. According to British Local Government Association (LGA) statistics, UK drivers waste an average of 31 hours during rush hours in a year at a cost of 1168 GBP to each motorist [1]. A road traffic injuries report from the world health organization indicated that in each year more than 1.25 million people die because of road traffic accidents, and these road traffic accidents cost around 3% of their gross domestic product [2].

As the economy and populations are growing in the world, the requirement of vehicles is irreversible. Therefore, an efficient and secure traffic management system is needed. Intelligent traffic systems (ITS) in a big picture sense aims to build a sustainable and efficient transportation system. This was initialised by Japan and carried on by the US in the 1980s and now it is considered by the entire world [3]. Vehicle-to-Vehicle(V2V) communication is considered as the most important part within ITS, and consistent and precise position information is the primary concern for V2V communication. Technically, satellite based navigation systems can provide position and navigation services under any circumstance.

The first satellite based navigation system, GPS was initialised by the US in 1973 and then Russia, European union, China, India, and Japan launched their own region or worldwide satellite based navigation system one after another. Now 32 GPS satellites are operating in space, which is the most complete operational navigation system. The performance of GPS can be degraded by multipath and Doppler effects,

and furthermore the availability of the GPS signal can be significantly diluted by surrounding buildings, overhead bridges, or even thick tree canopies. Therefore, an efficient and robust GPS receiver is essential for improving GPS positioning performance.

For a GPS receiver, successfully acquiring and consistently tracking the satellite signal is the first condition of obtaining the navigation message. In an urban environment, GPS signal strength could easily be reduced, therefore, sensitivity to weak satellite signals is a major concern. Furthermore, aiming to provide compensatory positioning information when GPS signal is unavailable, multisensor data fusion techniques become the optimal solution.

Common multisensor navigation for vehicles include GPS, inertial navigation sensors (INS) or inertial measurement units (IMU), magnetometer and LiDAR (light detection and ranging).

- GPS is a satellite based navigation system, where at least 4 satellites need to be successfully acquired and tracked in order to obtain 3D location information. The US government commits to the broadcast GPS signal accuracy being $\pm 7.8m$ with 95% probability. With a dual frequency method(L1+L2 or L1 +L5 frequency band) and augmentation system, GPS receiver can estimate the delay which generated by the ionosphere, the accuracy in the short term can reach to the centimeter level and in the long term measurements could reach to the millimeter level.

- IMU is an inertial measurement sensor that normally contains a gyroscope and an accelerometer. Gyroscopes can measure the angular velocity based on the inertial frame. Accelerometers are used to measure the specific force. Three gyroscopes and accelerometers are combined in an IMU in order to obtain 3 dimensional angular velocity and specific force.

- INS is the combination of the IMU measurement and mechanisation. Instead of the raw measurement of IMU, INS provides velocity, position, and attitude information.

- Magnetometers are used to measure the earth magnetism to provide the direction information, a compass is a type of magnetometer.

- LiDAR, also known as a laser scanner, is commonly used in surveying. It measures the distance and the angle between the object and the sensor.

1.3 Literature Review

Studies of improving the performance of the GPS stand alone receiver have been concidered for decades and many researchers have attempted to design an efficient signal acquisition scheme and a robust signal tracking loop to enhance the signal processing ability of the GPS receiver. [4] proposed a Fast Fourier Transform (FFT) based acquisition approach to increase the acquisition speed of the receiver. This method is efficient when used in a high Signal to Noise Ratio (SNR) environment. However, in a low SNR environment, this method is not effective since the FFT result is not sensitive to low SNR signals. In contrast, [5] presented a serial search approach in the time domain, which is sensitive to weak signals but the computional cost is high. Furthermore, in urban environments, the satellite signal reflection is unavoidable, and generates the multipath effect and degrades the accuracy of the pseudorange measurement. The most common multipath mitigation approach is to reject the reflected signal through hardware design. Conventional GPS antennas are designed to reject the reflected signal and receive the directed signal only. Nevertheless, nowadays people have realized the reflected signal is not completely without use. In [6] a dual polarization antenna is used to mitigate the mulitpath effect. A study reported in [7] implements a sensing method using the reflected signal. These two studies proved that the reflected signal could be implemented in real applications.

In GPS signal tracking procedures, there is a trade off between the tracking accuracy and the tracking ability [8], where greater tracking bandwidth can tolerate a higher Doppler frequency shifted signal but it is not sensitive to low strength signals. In contrast, a smaller tracking bandwidth is sensitive to the weak signals, but the tracking ability is reduced and it is not capable of tracking signals in highly dynamic environments. In vehicular communication, accurate tracking results and greater tracking bandwidth are required, therefore, aided tracking loop has been proposed in [9]. Kalman filters have been widely implemented in aided carrier tracking loops. Unlike the conventional carrier tracking loop, where the parameters of the loop filter are predefined, Kalman filter based carrier tracking loops [9] use the Kalman gain

to dynamically adjust the loop bandwidth according to the different circumstances. This approach can mitigate the trade off between the tracking accuracy and the tracking bandwidth. However, Kalman filters are restricted by the linear model, as in reality a nonlinear model is ubiquitous. Kalman filter based carrier tracking loops are inaccurate in some highly dynamic environments when the system model is highly nonlinear. Therefore, [10] and [11] implemented Extended Kalman Filters (EKF) instead of a conventional Kalman filter to aid the carrier tracking loop. In EKF based carrier tracking loops, a Jacobian matrix is implemented to linearise the nonlinear model. EKF based carrier tracking loops are more accurate compared to the KF based carrier tracking loop, however the computational cost of the Jacobian matrix is high. In order to reduce the computational cost, an unscented transform based Kalman filter also known as Unscented Kalman Filter (UKF) approach is proposed in [12]. Instead of linearising the nonlinear model using the Jacobian matrix, UKF linearise the distribution of the nonlinear model using an unscented transform. UKF can achieve an accuracy equal to the second order Taylor series expansion. However, as an open loop [12], UKF based carrier tracking loop is not sensitive to low Carrier to Noise Ratio (C/No) signal.

In a particular environment, such as tall trees, canopies, bridges or tunnels, GPS signals can be totally blocked or seriously degraded. Stand alone GPS receivers cannot provide any position or navigation information. Therefore, to mitigate these challenges, multisensor data fusion has been implemented in navigation applications. [13] [14]and [15] proposed the implementation of Inertial Navigation Sensors (INS) to compensate information when GPS signals are unavailable. In [16], an unscented Kalman filter is implemented to aid carrier tracking loop through IMU measurement. In [17] and [18], odometer and digital compasses are also implemented to aid INS/GPS in velocity and direction error correction. Furthermore, in [19], LiDAR is used to provide location information for indoor or GPS denied environments. Considering intergation approaches, the loosely and tightly integration approaches are the two major types of integration schemes, which will be discussed in detail in the following chapter. Kalman filter is the most common integration filter for both loose and tight integration. In [20], a standard Kalman filter was used to integrate GPS, INS and LiDAR for indoor navigation application. [17] and [18] implemented an extended Kalman filter and unscented Kalman filter respectively for INS/GPS loose integration. [15] used extended Kalman filter to linearise the

nonlinear pseudorange function to integrate IMU and GPS. [21], [22] [23] and [24] and [18] were used an unscented transformation instead of a Jacobian matrix to linearise the non-linear function and integrate IMU GPS and other sensors. Research results indicate that Kalman filters can achieve an optimal fusion result for linear models and unscented Kalman filters are superior to extended Kalman filter for nonlinear models. Furthermore, having additional sensors integrated with GPS, achieves a better performance.

1.4 Objectives

Due to the precise positioning requirement of vehicular communication. This thesis contributes to three aspects to improve the navigation performance in challenging environments. 1) Designing and implementing a modified serial search acquisition approach through a low cost dual polarization antenna to improve the acquisition ability of the stand alone GPS receiver. Then designing two efficient and robust carrier tracking approaches for highly dynamic environments and minimising the trade off between tracking ability and tracking accuracy to improve the tracking ability of the GPS stand alone receiver. 2) Designing an efficient and cost friendly multisensor data fusion approach which include GPS, IMU and LiDAR for vehicular communication in challenging environment.

- In order to improve the performance of a stand alone GPS receiver, the existing acquisition approaches are investigated. To improve the acquisition ability for urban environments, a low cost dual polarization patch antenna is proposed and designed.

- To compare and analyze the conventional FFT based and serial searching based acquisition approach, a novel modified serial searching acquisition approach has been implemented and attached to the low cost dual polarization path antenna.

- To evaluate the pros and cons of the conventional phase lock loop and the KF based carrier tracking loop. An efficient and robust carrier tracking loop is required to minimise the trade off between tracking accuracy and tracking ability.

- To investigate the mathematical model of carrier tracking loop and the limitation of Kalman filter. A adaptive Kalman filter and adaptive unscented Kalman filter based carrier tracking loop are proposed and implemented to improve the tracking performance.

- To evaluate the current multisensor integration schemes and analyze the characters of different navigation sensors. Then a low cost LiDAR aided dynamic integrated IMU/GPS navigation system is implemented.

- To compare the proposed approaches against existing methods, a hardware attached software testing platform is designed. Experiments are processed in a challenging outdoor environment.

1.5 Thesis Outline

This thesis is organized in six chapters.

Chapter 1 briefly introduces the background and the motivation of vehicular communication and the integrated navigation. Investigation and comparison of the existing GPS acquisition and tracking approach as well as the multisensor data fusion technique are also demonstrated in this chapter. At the end of this chapter, the objectives and the contributions are presented.

Chapter 2 starts from the the GPS signal structure and its processing algorithm. Then the overview of coordiate frames and their basic transform algorithm are also presented. Finally the error model of the IMU and the navigation mechanics of IMU and LiDAR are introduced.

Chapter 3 proposes a low cost dual polarization patch antenna and a modified serial searching acquisition approach. Through the modified serial search acquisition approach and the left hand polarization antenna, extra satellites signal can be successfully acquired in a very dense multipath environment. Furthermore, to evaluate the performance of the proposed patch antenna and the modified serial searching acquisition approach, a field experiment is conducted, and the results are analysed in this chapter.

Due to the requirement of greater tracking bandwidth and better tracking accuracy, chapter 4 presents two novel carrier tracking loops, hybrid KF integrated 3rd order PLL carrier tracking loop and adaptive UKF integrated 3rd order PLL carrier

tracking loop respectively. Meanwhile, in this chapter, the details of PLL, Kalman filter, unscented transform and adaptive filter are presented. To compare and analyse the proposed tracking approaches, an experiment is designed and presented in this chapter.

Chapter 5 describes the design and development of multisensor data fusion in integrated navigation. This integrated navigation scheme implements a dynamic federate Kalman filter to dynamically integrate GPS, IMU, Magnetometer and LiDAR. Furthermore, a novel line extraction scheme has also been presented in this chapter to improve the efficiency of the LiDAR processing. The performance is analysed and compared through a field experiment.

Chapter 6 draws conclusion of this research and its findings, and recommendations for future work are made.

1.6 Publications Related to the Thesis

1. Ahmed, A., Tiwari, R., Shah, M.A. and **Yin, J.**, 2016, July. GPS receiver phase jitter during ionospheric scintillation. In*Mechanical and Aerospace Engineering (ICMAE), 2016 7th International Conference on* (pp. 605-608). IEEE.

2. **Yin, J.**, R. Tiwari, and M. Johnston. "Low-cost dual polarized GPS antenna for effective signal acquisition in multipath environment." *Navigation Conference (ENC), 2017 European. IEEE, 2017.*

3. **Yin, J.**, R. Tiwari, and M. Johnston. "Adaptive Carrier Tracking for Vehicular Communication under High Dynamic Environment." *Navigation Conference (ENC), 2018 European. (Conference Digital Library)*

4. **Yin, J.**, Tiwari, R. and Johnston, M., 2018. Robust GPS Carrier Tracking Model using Unscented Kalman Filter for a Dynamic Vehicular Communication Channel. *IEEE Access.*

Chapter 2

System and Overview

2.1 Introduction

In this chapter, the structure of the GPS receiver and the generic GPS RF signal are reviewed. The structure of the GPS code and message are studied. To obtain the GPS navigation message, the schemes of GPS signal acquisition and carrier tracking are important, therefore several relevant acquisition and tracking schemes are reviewed in this chapter. Meanwhile, to implement multisensor data fusion technique on precise positioning, the background information of the relevant sensors are reviewed, such as IMU and LiDAR operational algorithm and their navigation mechanization.

2.2 GPS Receiver Outline

There are three parts within a GPS receiver, namely the RF front-end, baseband signal processing and navigation algorithm. The RF front-end works as the first part, it collects all in viewed GPS satellites signal and removes the noise and implement analog to digital conversion. Due to the Doppler effect which can cause carrier signal phase shift, and this phase shift is unpredictable, the local oscillator down grade the received signal to intermediate frequency (IF) signal instead of based band signal [8].

2.2.1 GPS Receiver RF Front-End

The center frequency of a GPS receiver front-end is usually set to be 1575.42 MHz corresponding to the GPS L1 band. Then the collected signal will be down grade

to IF signal since the IF signal is more desired than baseband signal. The received signal center frequency will be converted to be 1.2. The GPS L1 band signal is 1575.42 MHz and has bandwidth of 2 MHz. Based on the Nyquist law, the sampling frequency should be at least twice of the bandwidth, as there is no ideal filter, it is usually recommended to choose 2.5 times of the bandwidth in order to mitigate the filter roll off effect [25]. Therefore, 5 MHz is chosen for GPS L1 band.

2.2.2 GPS Signal Format

In a received GPS signal, there are two types of code are modulated, namely PRN (pseudorandom-noise) code and navigation code respectively. The following sections are briefly introduced these two types of code.

2.2.2.1 PRN code

Binary phase shift keying (BPSK) is known as one of the most popular sample modulation scheme in digital communication. BPSK encode the carrier signal to either 'as it' or 180° in difference. The extension scheme of the BPSK is called direct signal spread specturm (DSSS), a DSSS signal is consisted of navigation code, PRN code and RF signal. This DSSS signal is named PRN wave, since the frequency of the PRN code is much higher than the navigation code. Each satellite uses unique PRN code (C/A code for civil and P code for military) to implement CDMA. In this project, only C/A code is used. C/A code stands for coarse acquisition code which belong to the family of gold pseudorandom noise code. One advantage of the gold code is the strong autocorrelation and cross correlation properties. C/A code generator contains two 10 bit liner feedback shift registers(LFSR), two LFSRs feedback taps are defined by the generator polynomials as Eq.(2.1):

$$\begin{aligned} G1(X) &= 1 + X^3 + x^{10} \\ G2(X) &= 1 + X^2 + X^3 + X^6 + X^8 + X^9 + X^{10} \end{aligned} \tag{2.1}$$

Two generators generates pseudorandom codes with a length of $2^{10} - 1 = 1023$ bits, all bits are initialled to be 1. A simplified autocorrelation function of a C/A code can be presented as Eq.(2.2) :

$$R_{ca}(\tau) = \int_{\infty}^{\infty} CA_i(t)CA_i(t+\tau)dt, \tag{2.2}$$

where CA_i is the C/A code for the i^{th} satellite and τ is the time shift. The autocorrelation function is used to synchronize the received C/A code and the replica code. Meanwhile, cross correlation with any two C/A does are minimal for any phase, the ideal cross-correlation as below:

$$R_{ij}(\tau) = \int_{\infty}^{\infty} CA_j(t)CA_i(t+\tau)dt = 0 \tag{2.3}$$

where CA_i and CA_j are the CA code from different satellite, however due to the different delays and Doppler offsets, cross correlation value is not zero. Due to these characteristics, C/A code play a significant impotent role in GPS signal acquisition and tracking. The detail of GPS signal acquisition and tracking will be presented in the next two chapters.

2.2.2.2 Navigation message and RINEX format

Navigation message is 1500 bits long with 5 subframe in 300 bits each. Each subframe contains 10 words with 30 bits each, the last 6 bits of each word are used of parity check with Hamming code is employed. First two words of each subframe are *TLM* and *HOW*, fixed preamble 8 bits 10001011 in TLM never change [8].

As GPS position solution is determined by range between the obtained satellites and the receiver in three dimension [8]. Range measurement play an impotent role in GPS positioning, and the time, pseudotrange and phase information in RINEX filter are used to calculate a precise range measurement. RINEX stands for Receiver Independent Exchange Format was developed by University of Berne for easily exchange GNSS data from different GNSS receivers of different manufactures. Up till now two major versions of RINEX have been developed and published, namely version 2.x and version 3.x [26]. In RINEX file time, phase, and range are three fundamental quantities which need to be defined.

- Time: Time measurement is the receiver time of the received signal and it is identical for measurement of phase and range.
- Pseudo-Range: Pseudo-range (PR) is the distance between the receiver antenna to the satellite antenna. The reason of naming pseudo range is because of the distance contains the clock offset and atmospheric delay.
- Phase: Phase is the carrier-phase measured in whole cycles. Phase can be con-

verted to range using the frequency and the light of speed in vacuum. Furthermore, phase measurement is more accurate than pseudo range measurement, thus, phase measurement can be used as precise positioning.

RINEX file contains three ASCII file types, which are the observation file, the navigation file and the Meteorological data file respectively [27]. Each file contains a header section and a data section. As Figure 2.1 presented, observation file contains all the information of GNSS observation values such as satellite system identifier, (G for GPS, R for GLONASS, E for Galileo and C for BeiDou), pseudo range measurement in meter, phase circle measurement and signal strength. The navigation file is presented as Figure 2.2 presented, it contains the almanac and ephemeris information of the satellites in order to calculate the space position of each satellites.

2.2.3 Source of Inaccurate

GPS receiver normally needs to receive 7 to 8 satellites to provide a location information with an accuracy of $\pm 10m$. With less than 4 satellites, the GPS receiver will not be able to provide any position information. As with positioning, the accuracy of GPS is depended on many factors, and these factors are the motivation of our research. In the following sections, several main inaccurate source of GPS positioning are reviewed.

2.2.3.1 Satellites and Receiver clock error

On of the major inaccuracy sources is the clock bias between the GPS receiver and the GPS satellites. GPS device use the distance between the satellites and the receiver to calculate the user position. Within 1 nanosecond of satellite time inaccuracy can cause 30 centimeters of error in positioning. To mitigate the effect of the clock error, beside a very precise atomic clock is equipped on GPS satellite, the ground monitor station need to calculate the accumulated error and update the time error to the satellites. Even though, the clock error is still retain a few nanosecond and will cause about 1 meter inaccurate.

Furthermore, it is not practical to install a precise atomic clock to GPS receiver as it is installed to the satellites. Normally, a GPS receiver could have a few milliseconds clock drift within a second. To mitigate the effect of receiver drift, a common method is to use a reference satellites to estimate the clock drift of the receiver. Therefore,

```
     3.03           OBSERVATION DATA    M                   RINEX VERSION / TYPE
sbf2rin-13.0.1                         20180807 145519 UTC PGM / RUN BY / DATE
SEPT                                                       MARKER NAME
Unknown                                                    MARKER NUMBER
Unknown             Unknown                                OBSERVER / AGENCY
3023039             SEPT POLARX5E       5.2.0              REC # / TYPE / VERS
Unknown             Unknown                                ANT # / TYPE
  3666954.7414  -103408.0602  5200235.2269                 APPROX POSITION XYZ
        0.0000        0.0000        0.0000                 ANTENNA: DELTA H/E/N
G    9 C1C L1C C1W C2W L2W C2L L2L C5Q L5Q                  SYS / # / OBS TYPES
SEPTENTRIO RECEIVERS OUTPUT ALIGNED CARRIER PHASES.        COMMENT
NO FURTHER PHASE SHIFT APPLIED IN THE RINEX ENCODER.       COMMENT
G L1C                                                      SYS / PHASE SHIFT
G L2W                                                      SYS / PHASE SHIFT
G L2L  0.00000                                             SYS / PHASE SHIFT
G L5Q  0.00000                                             SYS / PHASE SHIFT
     0.050                                                 INTERVAL
  2018     8     7    14    53    7.6500000     GPS        TIME OF FIRST OBS
  2018     8     7    14    55   35.5500000     GPS        TIME OF LAST OBS
    28                                                     # OF SATELLITES
 C1C    0.000 C2C    0.000                                 GLONASS COD/PHS/BIS
  6 R03  5 R04  6 R11  0 R18 -3 R19  3 R20  2              GLONASS SLOT / FRQ #
                                                           END OF HEADER
> 2018 08 07 14 53  7.6500000  0 22
G01  20416362.444 7 107288752.06007  20416362.064 5  20416364.505 5  83601590.47405
G03  23047165.996 3
G08  21827217.612 6 114702835.95806  21827216.919 3  21827220.380 3  89378815.33703
G10
G11  20000383.028 7 105102749.39807  20000382.335 4  20000381.371 4  81898222.81304
G18  19773515.453 7 103910583.47407  19773514.975 4  19773514.575 4  80969257.99704
G22  21583987.050 7 113424661.02507  21583985.861 4  21583983.109 4  88382802.66604
G27
G28  22580517.783 3
G32  22511263.592 5 118297455.08005  22511263.534 1  22511265.506 1  92179868.86501
> 2018 08 07 14 53  7.7000000  0 22
G01  20416349.479 7 107288683.86607  20416349.099 5  20416351.528 5  83601537.33705
G03  23047132.365 3
G08  21827244.606 6 114702977.59706  21827243.913 3  21827247.331 3  89378925.70403
G10
G11  20000378.378 7 105102724.85807  20000377.685 4  20000376.698 4  81898203.68904
G18  19773519.576 7 103910605.00007  19773519.098 4  19773518.671 4  80969274.76904
G22  21583964.950 7 113424545.07007  21583963.761 4  21583961.042 4  88382712.31204
G27  24462794.472 3
G28  22580519.683 3
G32  22511259.984 5 118297435.81405  22511259.926 1  22511261.844 1  92179853.85201
```

Figure 2.1: RINEX Observation File

```
     3.03           N: GNSS NAV DATA    G: GPS              RINEX VERSION / TYPE
sbf2rin-13.0.1                         20180807 145519 UTC PGM / RUN BY / DATE
GPSA   4.6566E-09  1.4901E-08 -5.9605E-08 -5.9605E-08       IONOSPHERIC CORR
GPSB   7.7824E+04  4.9152E+04 -6.5536E+04 -3.2768E+05       IONOSPHERIC CORR
GPUT -9.3132257462E-10-3.552713679E-15 405504 2013          TIME SYSTEM CORR
    18                                                      LEAP SECONDS
                                                            END OF HEADER
G01 2018 08 07 16 00 00-7.390603423119E-05-4.092726157978E-12 0.000000000000E+00
     8.900000000000E+01-8.550000000000E+01 4.230533361553E-09 1.181865583091E+00
    -4.272907972336E-06 8.071259828284E-03 1.047365367413E-05 5.153671751022E+03
     2.304000000000E+05-6.891787052155E-08 2.282511683591E+00 1.061707735062E-07
     9.721869011553E-01 1.848125000000E+02 6.754623654788E-01-7.934973380634E-09
    -4.143029716675E-11 1.000000000000E+00 2.013000000000E+03 0.000000000000E+00
     2.800000000000E+00 0.000000000000E+00 5.587935447693E-09 8.900000000000E+01
     2.248080000000E+05 4.000000000000E+00
G03 2018 08 07 16 00 00 1.179017126560E-04 5.911715561524E-12 0.000000000000E+00
     3.200000000000E+01 8.250000000000E+00 4.734125766769E-09 2.203545577604E-01
     3.911554813385E-07 1.619163551368E-03 7.867813110352E-06 5.153699182510E+03
     2.304000000000E+05 5.587935447693E-09-2.958213401485E+00 2.235174179077E-08
     9.617163312540E-01 2.251562500000E+02 5.364815184486E-01-8.080693736186E-09
     3.310852195998E-10 1.000000000000E+00 2.013000000000E+03 0.000000000000E+00
     2.000000000000E+00 0.000000000000E+00 1.862645149231E-09 3.200000000000E+01
     2.258280000000E+05 4.000000000000E+00
G08 2018 08 07 13 59 44-1.108469441533E-04-1.364242052659E-12 0.000000000000E+00
     5.600000000000E+01-6.909375000000E+01 4.693766942805E-09 2.658968945529E+00
    -3.445893526077E-06 3.466341877356E-03 2.890825271606E-06 5.153607307434E+03
     2.231840000000E+05-7.078051567078E-08 1.216946629272E+00 1.881271600723E-07
     9.693288258993E-01 3.281562500000E+02-4.019537750338E-01-8.382134863848E-09
    -1.525063525017E-10 1.000000000000E+00 2.013000000000E+03 0.000000000000E+00
     2.000000000000E+00 0.000000000000E+00 5.122274160385E-09 5.600000000000E+01
     2.163660000000E+05 4.000000000000E+00
G08 2018 08 07 16 00 00-1.108562573791E-04-1.364242052659E-12 0.000000000000E+00
     5.700000000000E+01-6.040625000000E+01 4.648765068296E-09-2.571543758594E+00
    -3.036111593246E-06 3.467153408565E-03 2.954155206680E-06 5.153605821609E+03
     2.304000000000E+05-1.061707735062E-07 1.216886270735E+00 1.862645149231E-08
     9.693284499293E-01 3.281250000000E+02-4.020687472286E-01-8.272844597184E-09
    -9.071806448581E-11 1.000000000000E+00 2.013000000000E+03 0.000000000000E+00
     2.000000000000E+00 0.000000000000E+00 5.122274160385E-09 5.700000000000E+01
     2.248080000000E+05 4.000000000000E+00
G10 2018 08 07 14 00 00 1.874673180282E-04-1.023181539495E-12 0.000000000000E+00
     9.400000000000E+01 1.381250000000E+01 4.522688388125E-09-1.897148303659E+00
     7.450580596924E-07 3.671505488455E-03 8.385628461838E-06 5.153660322189E+03
     2.232000000000E+05-6.332993507385E-08-2.961567202624E+00-3.725290298462E-08
     9.617936713441E-01 2.199375000000E+02-2.772568722719E+00-7.915686862988E-09
     4.193031799462E-10 1.000000000000E+00 2.013000000000E+03 0.000000000000E+00
     2.000000000000E+00 0.000000000000E+00 1.862645149231E-09 9.400000000000E+01
     2.164260000000E+05 4.000000000000E+00
G10 2018 08 07 16 00 00 1.874598674476E-04-1.023181539495E-12 0.000000000000E+00
     9.500000000000E+01 3.625000000000E+00 4.564833000760E-09-8.465238649111E-01
     2.980232238770E-08 3.671790938824E-03 8.745118975639E-06 5.153663402557E+03
```

Figure 2.2: RINEX Navigation File

four satellites are the minimum requirement to provide 3D location information, as three for positioning and one for time reference.

2.2.3.2 Multipath Effect

When the satellites signal transmit from the satellites to the receiver, not only the direct signal are received. In addition to the directed signal, reflected signal from building, ground or trees are received by the receiver as well. These delay reflected signal can generate the uncertainty of the time which travel from the satellites to the receiver and dilute the positioning accuracy.

2.2.3.3 Weak Signal

GPS satellites is approximate 22 thousand kilometers away from the receiver. The received signal is typically as weak as $-125dBm$ to $-130dBm$. This weak signal is a challenge to the GPS device, partial black or reduce the signal strength can cause the GPS device fail to lock the satellites. In the ideal environment, C/No of the received signal is around $37dB-Hz$ to $45dB-Hz$, the receiver tracking C/No is $25dB-Hz$ and the acquisition is $35dB-Hz$, since acquisition is less sensitive to tracking. New method in [28], can reach the C/No as lower as $15dB-Hz$, but the computational cost has been significantly increased.

2.2.3.4 Doppler Effect

Relevant movement between the GPS satellites and the receiver can generate Doppler effect. Doppler effect can generate maximum $5kHz$ due to the satellite motion (when satellite move toward or away from the receiver), meanwhile receiver motion can also generate Doppler effect in $1.46Hz$ per $1Km/h$ [8]. Doppler effect value and sign depend on angle between signal line of vector and motion vector. Receiver oscillator offset can also generate Doppler effect in $1.575KHz/ppm$, typical oscillator offset is ± 1 ppm to ± 3 ppm. The total Doppler shift is roughly ± 10 KHz, therefore the GPS receiver needs to search 20 KHz band for visible satellite signal. Typically, the entire frequency searching range is divided into 41 band and each band is $500Hz$.

2.3 Reference frames

In positioning and navigation system, different sensors are located and measured in the different reference frames. Navigation system required the transformation of measurement and computed quantities from one frame to another. Therefore, several coordinate frames are used in this work will be reviewed in this section.

2.3.1 Earth Center Inertial Frame

Earth center inertial (ECI) frame is a reference frame which is applied in Newton's law. ECI frame is defined either in stationary or moving in a constant velocity. GNSS satellites location and velocity are defined in this frame.

- Center is at the mass of the earth
- z_i axis alongside with the Earth spin axis
- x_i axis points toward to the vernal equinox
- y_i completes the right-hand coordinate system

2.3.2 Earth Center Earth Fixed Frame

Earth Center earth fixed (ECEF) frame rotates relative to ECI frame in $7.292115 \times 10^{-5} rad/sec$ denote as σ [29].

- Center is at the mass of the Earth
- z_e axis along side with the Earth spin axis
- x_e axis points toward to the Mean meridian of Greenwich.
- y_e axis completes the right handed coordinates system.

2.3.3 Local Frame

Local frame is refereed as East-North-Up (ENU) frame which serve as the representation of the attitude and velocity when the vehicle is on or near the earth surface.

- Center is at the center of the reference frame
- Z axis (Up) point upward along the ellipsoid normal

- x axis (East) point toward to the geodesic East
- y axis (North) point toward to the geodesic North

There three reference frames are demonstrated as Figure.2.3.

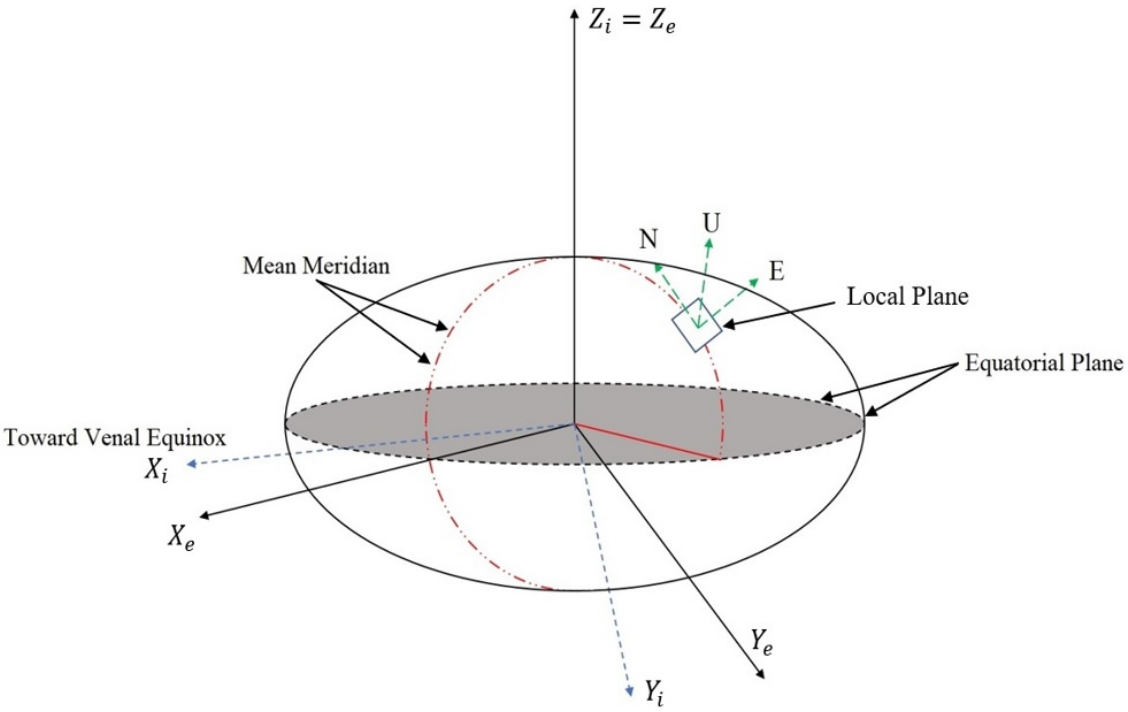

Figure 2.3: ECI, ECEF and Local frame

2.3.4 Body Frame

In navigation application, the aim is to determine the position and the velocity base on the various sensors which attached on the platform, and this platform is referred as a body frame

- Center is at the center of the sensor.
- z axis is point upword refer as the yaw
- x axis is toward to right of the move object refer as the pitch
- y axis is toward to the frond of the moving object refer as roll

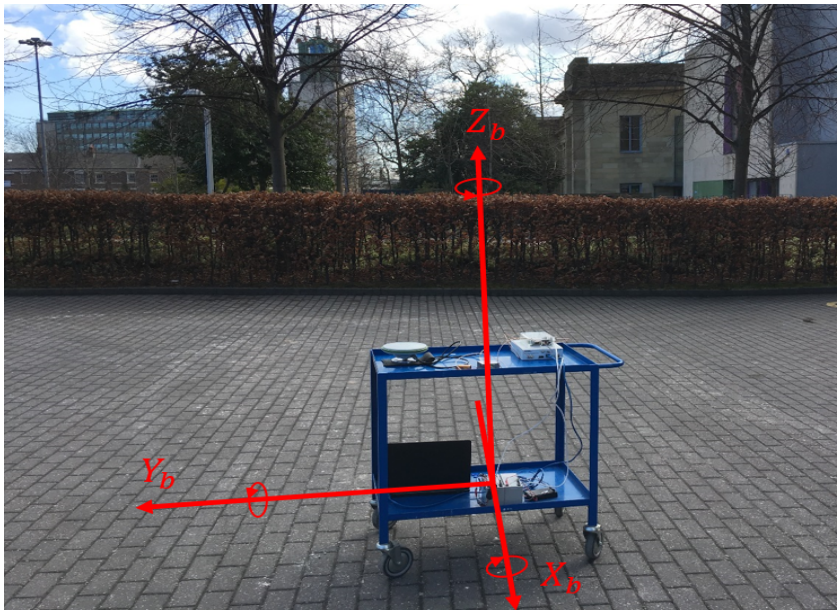

Figure 2.4: Body Frame

2.3.5 WGS84

The world geodetic system 1984 is defined and maintained by the United States National Geospatial-Intelligence Agency (NGA). All the GPS measurement results is based on WGS84.

- Center is a the center of the mass of the Earth.
- h denotes the attitude above the reference ellipsoid
- φ denotes the latitude
- λ denotes the longitude

2.4 Coordinate Frame Transformation

As we mentioned before, coordinate frame transformation play an impotent role in navigation system since different sensors operate under different reference frame. A vector transform from one frame to another frame can use direction cosine, Euler angle and quaternion. All of these methods are required rotation matrix which is named transformation matrix or direction consin matrix (DCM).

2.4.1 Transformation between ECI and ECEF

The transformation from ECI frame (denote as i-frame) to ECEF frame (denotes as e-frame), is to rotate i-frame by ω_e degree about z-axis as Figure 2.5 illustrated. ω_e is the magnitude of the earth rotation. The rotation matrix is denoted as

$$R_i^e = \begin{bmatrix} cos\omega_e t & sin\omega_e t & 0 \\ -sin\omega_e t & cos\omega_e t & 0 \\ 0 & 0 & 1 \end{bmatrix} \tag{2.4}$$

where t is the time since the reference epoch. The transformation from e-frame to i-frame is the inverse matrix of R_i^e.

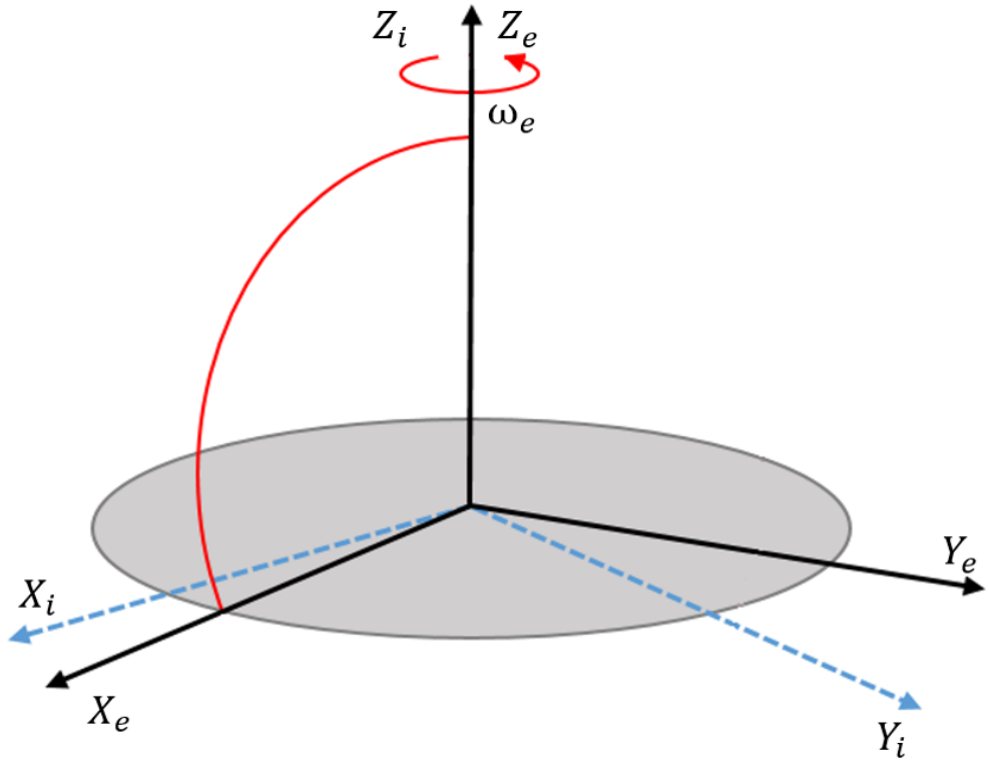

Figure 2.5: ECI to ECEF frame

2.4.2 Transformation between ENU and ECEF Frame

The transformation from ENU frame to e-frame contains two steps. First, ENU frame rotate $\varphi - 90$ degree around its x-axis. In the second step, ENU frame rotates

$-90-\lambda$ degree around its z-axis. The rotation matrix can be expressed as

$$R^e_{ENU} = \begin{bmatrix} cos(-90-\lambda) & sin(-90-\lambda) & 0 \\ -sin(-90-\lambda) & cos(-90-\lambda) & 0 \\ 0 & 0 & 1 \end{bmatrix} \begin{bmatrix} 1 & 0 & 0 \\ 0 & cos(\varphi-90) & sin(\varphi-90) \\ 0 & -sin(\varphi-90) & cos(\varphi-90) \end{bmatrix} \tag{2.5a}$$

$$R^e_{ENU} = \begin{bmatrix} -sin\lambda & -cos\lambda & 0 \\ cos\lambda & -sin\lambda & 0 \\ 0 & 0 & 1 \end{bmatrix} \begin{bmatrix} 1 & 0 & 0 \\ 0 & sin\varphi & -cos\varphi \\ 0 & cos\varphi & sin\varphi \end{bmatrix} \tag{2.5b}$$

$$R^e_{ENU} = \begin{bmatrix} -sin\lambda & -sin\varphi cos\lambda & cos\varphi cos\lambda \\ cos\lambda & -sin\varphi sin\lambda & cos\varphi sin\lambda \\ 0 & cos\varphi & sin\varphi \end{bmatrix} \tag{2.5c}$$

Then the transformation from e-frame to ENU frame is

$$R^e_{ENU} = (R^{ENU}_e)^T \tag{2.6}$$

In contrast, the position vector in ECEF frame can be defined as

$$P = [\varphi, \lambda, h] \tag{2.7}$$

The rate of position change can be expressed as

$$\begin{aligned} \dot{\varphi} &= \frac{v_n}{R_m + h} \\ \dot{\lambda} &= \frac{v_e}{(R_n + h)cos\varphi} \\ \dot{h} &= v_u \end{aligned} \tag{2.8}$$

where R_m is the radii of curve in Meridian and the R_n is the Prime vertical. v_n, v_e and v_u are the velocity in ENU frame. Figure 2.6 illustrated the detail of the transformation from ENU frame to ECEF frame.

2.4.3 Transformation between ENU and Body Frame

This rotation matrix of the transformation from Body frame(b-frame) to ENU frame can be defined by a series of three plane rotation. In this research we use ϕ represents

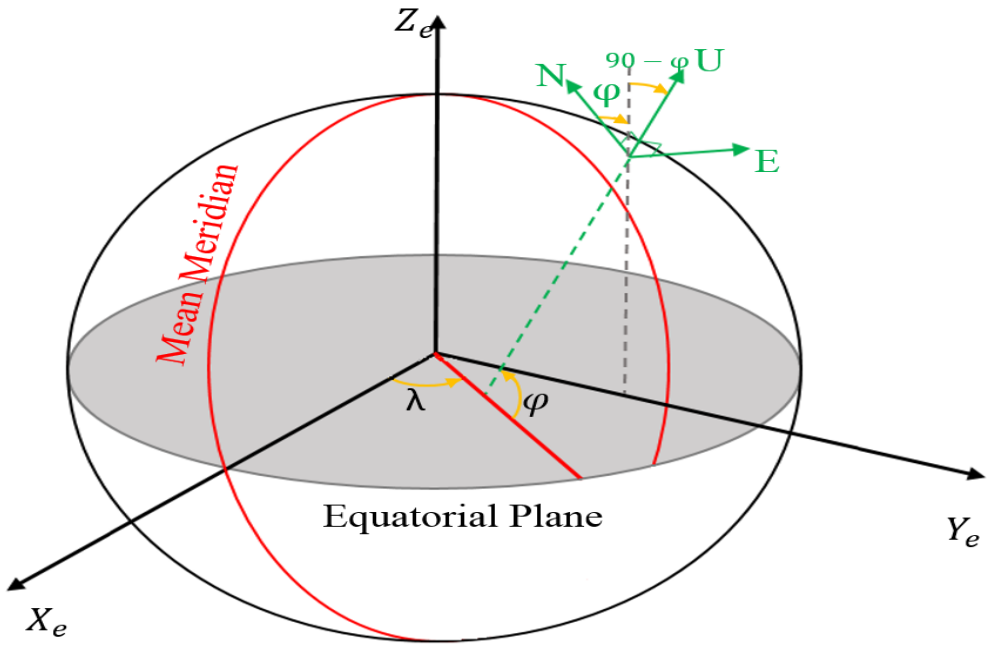

Figure 2.6: ENU to ECEF

roll, θ represents pitch and ψ represents yaw. The rotation matrix is defined as

$$R_b^{ENU} = \begin{bmatrix} cos\psi & sin\psi & 0 \\ -sin\psi & cos\psi & 0 \\ 0 & 0 & 1 \end{bmatrix}^T \begin{bmatrix} 1 & 0 & 0 \\ 0 & cos\theta & sin\theta \\ 0 & -sin\theta & cos\theta \end{bmatrix}^T \begin{bmatrix} cos\phi & 0 & -sin\phi \\ 0 & 1 & 0 \\ sin\phi & 0 & cos\phi \end{bmatrix}^T \tag{2.9a}$$

$$R_b^{ENU} = \begin{bmatrix} cos\psi & -sin\psi & 0 \\ sin\psi & cos\psi & 0 \\ 0 & 0 & 1 \end{bmatrix} \begin{bmatrix} 1 & 0 & 0 \\ 0 & cos\theta & -sin\theta \\ 0 & sin\theta & cos\theta \end{bmatrix} \begin{bmatrix} cos\phi & 0 & sin\phi \\ 0 & 1 & 0 \\ -sin\phi & 0 & cos\phi \end{bmatrix} \tag{2.9b}$$

$$R_b^{ENU} = \begin{bmatrix} cos\psi cos\phi - sin\psi sin\theta sin\phi & -sin\psi cos\theta & cos\psi sin\phi + sin\psi sin\theta cos\phi \\ sin\psi cos\phi + cos\psi sin\theta sin\phi & cos\psi cos\theta & sin\psi sin\phi - cos\psi sin\theta cos\phi \\ -cos\theta sin\phi & sin\theta & cos\theta cos\phi \end{bmatrix} \tag{2.9c}$$

The value of Roll, Pitch and Yaw can be calculated as

$$\phi = -tan^{-1}[\frac{R_b^{ENU}(3,1)}{R_b^{ENU}(3,3)}] \tag{2.10a}$$

$$\theta = -tan^{-1}\left\{\frac{R_b^{ENU}(3,2)}{\sqrt{[R_b^{ENU}(1,2)]^2 + [R_b^{ENU}(2,2)]^2}}\right\} \tag{2.10b}$$

$$\psi = -tan^{-1}[\frac{R_b^{ENU}(1,2)}{R_b^{ENU}(2,2)}] \tag{2.10c}$$

The Transformation from ENU frame to body frame can be calculated by the inverse of rotation matrix R_b^{ENU}.

$$R_b^{ENU} = (R_{ENU}^b)^T \tag{2.11}$$

2.4.4 Transformation between ECEF and WGS84

The transformation from ECEF to WGS84 is presented as below Eq.(2.12) [29]

$$\begin{bmatrix} x \\ y \\ z \end{bmatrix} = \begin{bmatrix} (R_n + h)cos(\phi)cos(\varphi) \\ (R_n + h)cos(\phi)sin(\lambda) \\ [R_n(1 - e^2) + h]sin(\varphi) \end{bmatrix} \tag{2.12}$$

2.5 Attitude Mechanization

Attitude estimation is about estimating the attitude in the body-frame respect to the n-frame. The common methods are Euler Angel, Direct cosine Matrix and Quaternion [30].

2.5.1 Euler Angle

The most common way to express the attitude of the rigid body is the euler angle, since it is easy to use and understand. A vector (x,y,z) rotate in a fixed coordinate can be considered as a combination of the three rotation around three axis. First it rotate ψ angle around z-axis, the rotation matrix $C_n^b(\psi)$ can be represented as

$$C_n^b(\psi) = \begin{bmatrix} cos\psi & sin\psi & 0 \\ -sin\psi & cos\psi & 0 \\ 0 & 0 & 1 \end{bmatrix} \tag{2.13}$$

Then rotate θ angle around y-axis, the rotation matrix $C_n^b(\theta)$ can be expressed as

$$C_n^b(\theta) = \begin{bmatrix} cos\theta & 1 & -sin\theta \\ 0 & 1 & 0 \\ sin\theta & 0 & cos\theta \end{bmatrix} \tag{2.14}$$

Then rotate ϕ angle around x-axis, the roation matrix $C_n^b(\phi)$

$$C_n^b(\phi) = \begin{bmatrix} 1 & 0 & 0 \\ 0 & cos\phi & sin\phi \\ 0 & -sin\phi & cos\phi \end{bmatrix} \tag{2.15}$$

The integrated rotation matrix $C_n^b(\phi, \theta, \psi) = C_n^b(\phi) \cdot C_n^b(\theta) \cdot C_n^b(\psi)$ in matrix form

$$C_n^b(\phi, \theta, \psi) = \begin{bmatrix} cos\psi cos\theta & cos\theta sin\psi & -sin\theta \\ cos\psi sin\phi sin\theta - cos\phi sin\phi & cos\phi cos\psi + sin\phi sin\psi sin\theta & cos\theta sin\phi \\ sin\phi sin\psi + cos\phi cos\psi sin\theta & cos\phi sin\psi sin\theta - cos\psi sin\phi & cos\phi cos\theta \end{bmatrix} \tag{2.16}$$

while ϕ, ψ, θ are refer as roll, yaw and pitch.

Euler angle is the most simple and intuitive approach, however, there is a limitation of Euler angle, when θ angle is 90°,

$$\begin{aligned} C_n^b &= \begin{bmatrix} 0 & 0 & -1 \\ cos\psi sin\phi - cos\phi sin\psi & cos\phi cos\psi + sin\phi sin\psi & 0 \\ sin\phi sin\psi + cos\phi cos\psi & cos\phi sin\psi - cos\psi sin\phi & 0 \end{bmatrix} \\ &= \begin{bmatrix} 0 & 0 & -1 \\ sin(\phi - \psi) & cos(\phi - \psi) & 0 \\ cos(\phi - \psi) & -sin(\phi - \psi) & 0 \end{bmatrix} \end{aligned} \tag{2.17}$$

Roll ϕ and Pitch ψ angle are equivalent. This is called gimbal lock.

2.5.2 Direction Cosine Matrix

Considering a vector $a = \{\overrightarrow{a}_1, \overrightarrow{a}_2, \overrightarrow{a}_3\}$ rotate from n-frame to body-frame then, the rotated vector $b = \left\{\overrightarrow{b}_1, \overrightarrow{b}_2, \overrightarrow{b}_3\right\}$, the rotation process can be expressed as

$$\begin{bmatrix} \overrightarrow{b}_1 \\ \overrightarrow{b}_2 \\ \overrightarrow{b}_3 \end{bmatrix} = \begin{bmatrix} C_{11} & C_{12} & C_{13} \\ C_{21} & C_{22} & C_{23} \\ C_{31} & C_{32} & C_{33} \end{bmatrix} \begin{bmatrix} \overrightarrow{a}_1 \\ \overrightarrow{a}_2 \\ \overrightarrow{a}_3 \end{bmatrix} \tag{2.18}$$

where C_{ij} is the direction cosine matrix, and the three elementary rotation matrix respect to the first second and third rotation axis can be expressed as Eq.(2.19)

$$
\begin{aligned}
C_1(\theta_1) &= \begin{bmatrix} 1 & 0 & 0 \\ 0 & cos\theta_1 & sin\theta_1 \\ 0 & -sin\theta_1 & cos\theta_1 \end{bmatrix} \\
C_2(\theta_2) &= \begin{bmatrix} cos\theta_2 & 0 & -sin\theta_2 \\ 0 & 1 & 0 \\ sin\theta_2 & 0 & cos\theta_2 \end{bmatrix} \\
C_3(\theta_2) &= \begin{bmatrix} cos\theta_3 & sin\theta_3 & 0 \\ -sin\theta_3 & cos\theta_3 & 0 \\ 0 & 0 & 1 \end{bmatrix}
\end{aligned}
\tag{2.19}
$$

Given pitch, roll and yaw, then direction cosine matrix (DCM) can be expressed in

$$
\begin{aligned}
C_1C_2C_3 &= \begin{bmatrix} 1 & 0 & 0 \\ 0 & cos\phi & sin\phi \\ 0 & -sin\phi & cos\phi \end{bmatrix} \begin{bmatrix} cos\theta & 0 & -sin\theta \\ 0 & 1 & 0 \\ sin\theta & 0 & cos\theta \end{bmatrix} \begin{bmatrix} cos\psi & sin\psi & 0 \\ -sin\psi & cos\psi & 0 \\ 0 & 0 & 1 \end{bmatrix} \\
&= \begin{bmatrix} cos\psi cos\theta & cos\theta sin\psi & -sin\theta \\ cos\psi sin\phi sin\theta - cos\phi sin\phi & cos\phi cos\psi + sin\phi sin\psi sin\theta & cos\theta sin\phi \\ sin\phi sin\psi + cos\phi cos\psi sin\theta & cos\phi sin\psi sin\theta - cos\psi sin\phi & cos\phi cos\theta \end{bmatrix}
\end{aligned}
\tag{2.20}
$$

DCM can avoid gimble lock, but DCM need multiple sine and cosine computation, the compuation cost is very high.

2.5.3 Quaternion

Quaternion parametrization is less initiative compare to Euler angle, but the quaternion approach is a preferred implementation approach since it is lack of singularity and trigonometric functions compare to the Euler angle approach in the integration routine and small number of parameters compare to the DCM approach.

A quaternion is defined as a combination of a scale q_0 and a vector $\mathbf{q} = (q_1, q_2, q_3)$;

$$
q = q_0 + \mathbf{q} = q_0 + q_1 i + q_2 j + q_3 k \tag{2.21}
$$

The relationship of the i, j and k are introduced as Eq.(2.22)

$$\begin{aligned} i^2 = j^2 = k^2 = ijk \\ ij = -ji = k \\ jk = -kj = j \\ ki = ik = j \end{aligned} \tag{2.22}$$

There are four ways to represent quaternion.

- In vector combination form, quaternion $\mathbf{Q}$ can be expressed as

$$\mathbf{Q} = q + \mathbf{q} \tag{2.23}$$

- In complex number form,

$$\mathbf{Q} = q_0 + q_1 i + q_2 j + q_3 k \tag{2.24}$$

  and its conjugate is

$$\mathbf{Q}^* = q_0 - q_1 i - q_2 j - q_3 k \tag{2.25}$$

- In triangle form,

$$\mathbf{Q} = cos\frac{\theta}{2} + \mathbf{u}cos\frac{\theta}{2} \tag{2.26}$$

  where $\mathbf{u}$ is the unit vector.

- In matrix form,

$$\mathbf{Q} = \begin{bmatrix} q_0 \\ q_1 \\ q_2 \\ q_3 \end{bmatrix} \tag{2.27}$$

2.5.3.1 Quaternion Addition and Deduction

Considering quaternion q add quaternion p, quaternion p is denoted as

$$p = p_0 + p_1 i + p_2 j + p_3 k \tag{2.28}$$

Adding two quaternions acts component wise, quaternion $p \pm q$ is presented as below

$$q \pm p = (q_0 \pm p_0) + (q_1 \pm p_1)i + (q_2 \pm p_2)j + (q_3 \pm p_3)k \tag{2.29}$$

2.5.3.2 Quaternion Multiplication

The product of a vector a and a quaternion q are presented as

$$aq = aq_0 + aq_1 i + aq_2 j + aq_3 k \tag{2.30}$$

The product of two quaternions $p \times q$ are presented as

$$\begin{aligned} q \times p &= (q_0 + q_1 i + q_2 j + q_3 k) \times (p_0 + p_1 i + p_2 j + p_3 k) \\ &= (q_0 p_0 - q_1 p_1 - q_2 p_2 - q_3 p_3) + (q_1 p_0 + q_0 p_1 + q_3 p_2 - q_2 p_3) i \\ &+ (q_2 p_0 + q_0 p_2 + q_1 p_3 - q_3 p_1) j + (q_3 p_0 + q_0 p_3 + q_2 p_1 - q_1 p_2) k \end{aligned} \tag{2.31}$$

Wrote in matrix form

$$q \times p = \begin{bmatrix} q_0 & -q_1 & -q_2 & -q_3 \\ q_1 & q_0 & -q_3 & q_2 \\ q_2 & q_3 & -q_0 & -q_1 \\ q_3 & -q_2 & q_1 & q_0 \end{bmatrix} \begin{bmatrix} p_0 & -p_1 & -p_2 & -p_3 \\ p_1 & p_0 & -p_3 & p_2 \\ p_2 & p_3 & p_0 & -p_1 \\ p_3 & -p_2 & p_1 & p_0 \end{bmatrix} \tag{2.32}$$

From Eq.(2.32), we can see the first column of the matrix q and p are the quaternion q and p themselves and the fist row are the conjugate of the quaternion q and p, the lower 3×3 matrix is the core of the quaternion q and p product [31].

2.5.3.3 Quaternion Division-Inversion

If $P \times R = 1$, then quaternion R is the inversion of quaternion P, denotes as $P = R^{-1}$ or $R = P^{-1}$. Base on the norm rule,

$$\begin{aligned} P \times P^* &= (P_0 + P_1 i + P_2 j + P_3 k) \times (P_0 - P_1 i - P_2 j - P_3 k) \\ &= P_0^2 + P_1^2 + P_2^2 + P_3^3 \\ &= \|\mathbf{P}\| \end{aligned} \tag{2.33}$$

Since,

$$P \times \frac{P^*}{\|\mathbf{P}\|} = 1 \tag{2.34}$$

the inversion of quaternion P is

$$P^{-1} = \frac{P^*}{\|\mathbf{P}\|} \tag{2.35}$$

2.5.3.4 Quaternion Rotation

Consider a frame **a** align with a frame **b**, then frame **a** rotates θ degree base on vector **E**. Quaternion **b** represents the transformation matrix.

$$\mathbf{b} = \begin{bmatrix} cos\frac{\theta}{2} \\ \mathbf{E}cos\frac{\theta}{2} \end{bmatrix} \tag{2.36}$$

The unit quaternion **b** has the normalirity property that $\|\mathbf{b}\| = 1$.

Cosidering the $v = C_a^b z$ represents the coordinate z in frame **a**, v is the coordinate z which represents in frame **b**. Quaternion v and z are represent as

$$q_v = \begin{bmatrix} 0 \\ v \end{bmatrix} \tag{2.37}$$

$$q_z = \begin{bmatrix} 0 \\ z \end{bmatrix} \tag{2.38}$$

In quaternion matrix

$$\begin{aligned} q_v &= \mathbf{b} q_z \mathbf{b}^* \\ q_v &= \begin{bmatrix} b_0 & -b_1 & -b_2 & -b_3 \\ b_1 & b_0 & -b_3 & b_2 \\ b_2 & b_3 & b_0 & -b_1 \\ b_3 & -b_2 & b_1 & b_0 \end{bmatrix} \begin{bmatrix} b_0 & b_1 & b_2 & b_3 \\ -b_1 & b_0 & -b_3 & b_2 \\ -b_2 & b_3 & b_0 & -b_1 \\ -b_3 & -b_2 & b_1 & b_0 \end{bmatrix} \begin{bmatrix} 0 \\ z \end{bmatrix} \end{aligned} \tag{2.39}$$

The product is

$$\mathbf{b} \times \mathbf{b}^* = \begin{bmatrix} 1 & 0 & 0 & 0 \\ 0 & b_0^2 + b_1^2 - b_3^2 - b_2^2 & 2(b_1 b_2 - b_0 b_3) & 2(b_1 b_3 + b_0 b_2) \\ 0 & 2(b_1 b_2 + b_0 b_3) & b_0^2 - b_1^2 + b_3^2 - b_2^2 & 2(b_2 b_3 - b_0 b_1) \\ 0 & 2(b_1 b_3 - b_0 b_2) & 2(b_0 b_1 + b_2 b_4) & b_0^2 - b_1^2 - b_3^2 + b_2^2 \end{bmatrix} \tag{2.40}$$

Therefore, the transformation matrix C_a^b can be simplified as

$$C_a^b = \begin{bmatrix} b_0^2 + b_1^2 - b_3^2 - b_2^2 & 2(b_1 b_2 - b_0 b_3) & 2(b_1 b_3 + b_0 b_2) \\ 2(b_1 b_2 + b_0 b_3) & b_0^2 - b_1^2 + b_3^2 - b_2^2 & 2(b_2 b_3 - b_0 b_1) \\ 2(b_1 b_3 - b_0 b_2) & 2(b_0 b_1 + b_2 b_4) & b_0^2 - b_1^2 - b_3^2 + b_2^2 \end{bmatrix} \tag{2.41}$$

Converting the quternion back to the Euler angle, the ϕ, θ, ψ

$$\begin{aligned} \phi &= atan2(2(b_2 b_3 - b_0 b_1), 1 - 2(b_1^2 + b_2^2) \\ \theta &= sin^{-1}(2(b_1 b_3 - b_0 b_2)) \\ \psi &= atan2(2(b_1 b_2 - b_0 b_3), 1 - 2(b_2^2 + b_3^2) \end{aligned} \tag{2.42}$$

2.5.3.5 Quaternion Derivative

As mentioned before, a quaternion can be represented in triangle form as

$$\mathbf{Q} = cos\frac{\theta}{2} + \mathbf{u}cos\frac{\theta}{2} \tag{2.43}$$

Within Δt time, the change of the quaternion Δt can be expressed as

$$\Delta\mathbf{Q} = cos\frac{\Delta\theta}{2} + \hat{\omega}sin\frac{\Delta\theta}{2} \tag{2.44}$$

This change can be considered as rotating about the instantaneous axis $\hat{\omega} = \frac{\omega}{\|\omega\|}$, with $\Delta\theta$ angle. Therefore, Eq.(2.44) can be expressed as

$$\Delta\mathbf{Q} = cos\frac{\|\omega\|\,\Delta t}{2} + \hat{\omega}sin\frac{\|\omega\|\,\Delta t}{2} \tag{2.45}$$

since $\Delta\theta = \|\omega\|\,\Delta t$.

The rotation quaternion at time $t + \Delta t$, $\mathbf{Q}(t + \Delta t)$ can be expressed as

$$\mathbf{Q}(t + \Delta t) = \Delta\mathbf{Q}\mathbf{Q}(t) \tag{2.46}$$

From Eq.(2.45) and Eq.(2.46), the difference of quaternion within Δt time can be represented as

$$\begin{aligned} \mathbf{Q}(t + \Delta t) - \mathbf{Q}(t) &= (cos\frac{\|\omega\| \Delta t}{2} + \hat{\omega} sin\frac{\|\omega\| \Delta t}{2})\mathbf{Q}(t) - \mathbf{Q}(t) \\ &= -2sin^2\frac{\|\omega\| \Delta t}{2}\mathbf{Q}(t) + \hat{\omega} sin\frac{\|\omega\| \Delta t}{2}\mathbf{Q}(t) \end{aligned} \tag{2.47}$$

Skip the higher order [32], the derivative of quaternion $\mathbf{Q}$,can be expressed

$$\begin{aligned} \dot{\mathbf{Q}} &= \lim_{\Delta t \to 0} \mathbf{Q}(t + \Delta t) - \mathbf{Q}(t) \\ &= \hat{\omega} \lim_{\Delta t \to 0} \frac{sin\frac{\|\omega\| \Delta t}{2})}{\Delta t}\mathbf{Q}(t) \\ &= \hat{\omega}\frac{\mathrm{d}}{\mathrm{d}x} sin(\frac{\|\omega\| \Delta t}{2})|_{t=0}\mathbf{Q}(t) \\ &= \frac{1}{2}\omega(t)\mathbf{Q}(t) \end{aligned} \tag{2.48}$$

The last part of Eq.(2.48) is commonly used in quaternion update algorithm.

2.6 IMU Mechanization

As the IMU name presented, the measurements of the IMU are angular velocity and specific force. These measurements contain huge amount of noise and earth gravity, therefore the measurement of IMU cannot use directly, a series of algorithms are required to obtain the navigation information [33]. These series of algorithms is named as IMU mechanization.

2.6.1 IMU Measurement Model

The acceleration $\tilde{f^b}$ and the angular velocity $\tilde{\omega}$ can be measured by IMU, and the results are presented as Eq.(2.49b)

$$\tilde{f^b} = f^b + \Delta f^b \tag{2.49a}$$

$$\tilde{\omega} = \omega_{ib}^b + \Delta\omega_{ib}^b \tag{2.49b}$$

where Δf^b and $\Delta\omega_{ib}^b$ represent the error of specific force and inertial relative angular rate measurement. If there is no error in IMU measurement, which is impossible in reality, the relationship between the position $\dot{r}^n$ and the velocity v^n are presented as below

$$\dot{r}^n = D^{-1}v^n \tag{2.50}$$

where $\dot{r}^n$ is in navigation frame which contains ϕ is the latitude, λ is the longitude, and h is the height above the earth surface;

$$D^{-1} = \begin{bmatrix} \frac{1}{R_m+h} & 0 & 0 \\ 0 & \frac{1}{(R_n+h)cos\alpha} & 0 \\ 0 & 0 & -1 \end{bmatrix} \tag{2.51}$$

where R_m and R_m are the radii of curvature in the meridian and prime vertical and computed as Eq.(2.52)

$$\begin{aligned} R_M &= \frac{a(1-e^2)}{(1-e^2\cdot sin^2\varphi)^{3/2}} \\ R_N &= \frac{a}{(1-e^2\cdot sin^2\varphi)^{1/2}} \end{aligned} \tag{2.52}$$

where $a = 6378317.0m$ and $e = 0.0818$ are the semi-major axis length and the eccentricity of the WGS-84 ellipsoid [34].

The velocity model can be expressed as Eq.(2.53)

$$\dot{v}^n = R_b^{ENC}(f^b - b_a) - (2\omega_{ie}^n + \omega_{en}^n)v^n + g^n \tag{2.53}$$

$\dot{v}^n = [v_N, v_E, v_D]$ is the platform velocity, R_b^{ENC} is the transformation matrix from body-frame to local-frame and R_{ENC}^b for vice versa. f^b is the specific force measured by accelerometer; ω_{ie}^n and ω_{en}^n are the Earth turn rate in local-frame and the turn rate of the local-frame with the respect to the Earth;

$$\omega_{ie}^n = \begin{bmatrix} 0 & \sigma cos\phi & \sigma sin(\phi) \end{bmatrix}^T \tag{2.54}$$

The local frame rotate rate respect to ECEF frame ω_{en}^n can be obtained as

$$\omega_{en}^n = \begin{bmatrix} \frac{-v_n}{R_M+h} & \frac{v_E}{R_N+h} & \frac{v_E tan\phi}{R_N+h} \end{bmatrix} \tag{2.55}$$

where g is the local gravity vector, b_a is the drift of the accelerometer. Attitude mechanization ω_{nb}^b can be expressed as below Eq.(2.56)

$$\omega_{nb}^b = \omega_{ib}^b - R_{ENC}^b(\omega_{ie}^n + \omega_{en}^n)b_g \tag{2.56}$$

ω_{ib}^b is the body angular rate measured by gyroscopes expressed in the b-frame, b_g is the drift of the gyroscope.

In our project, the IMU provides the measurements of accelerometer and gyroscope in 6 degree of freedom. Through these measurements, the orientation of the IMU can be estimated using Kalman filter. The orientation results are presented as Figure 2.7.

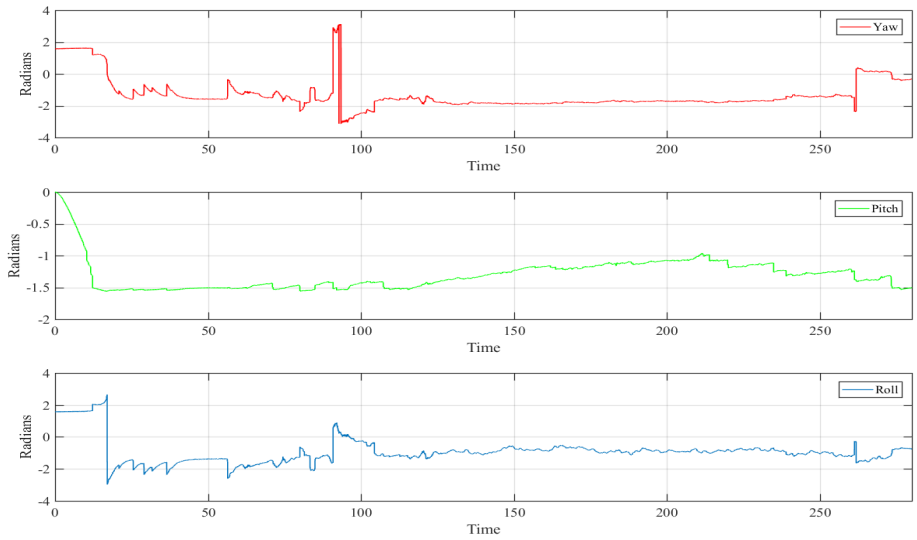

Figure 2.7: Orientation Estimation

2.6.2 INS Error Model

There is no doubt that IMU measurement contains error and these errors drift the IMU navigation results. Since the IMU error could be accumulated with time, the IMU error propagation model need to work alongside with the system motion model in order to further correct the error. The following sections analysis the error model of IMU measurement.

2.6.2.1 Position Error Model

The relationship between geodetic coordinate change and velocity can be expressed as Eq.(2.57)

$$\begin{bmatrix} \dot{\phi} \\ \dot{\lambda} \\ \dot{h} \end{bmatrix} = \begin{bmatrix} \frac{V_N}{R_M+h} \\ \frac{V_E}{cos(\phi)(R_N+h)} \\ -V_U \end{bmatrix} \tag{2.57}$$

Position change ϕ, λ, h are represent Longitude Latitude and Height respectively. Velocity are in NEU frame. Since Eq.(2.57) is a nonlinear function, Eq.(2.57) can also be simplified as

$$\begin{aligned} \dot{P} &= f_p(P, v) \\ \dot{\hat{P}} &= f_p(\hat{P}, \dot{\hat{v}}) \end{aligned} \tag{2.58}$$

The parameters with ffl represent the measurement value. Linearised $\dot{P}$ around $\dot{\hat{P}}$, and neglected the higher order, the rest is presented as Eq.2.59)

$$\dot{P} = f_p(\hat{P}, \hat{v}) + F_{rr}\delta P + F_{rv}\delta v + F_{r\varepsilon}\varepsilon \tag{2.59}$$

Therefore, position error can be formulated as

$$\Delta P = F_{rr}\delta P + F_{rv}\delta v + F_{r\varepsilon} + \delta\varepsilon \tag{2.60}$$

Detail of matrix $F_{rr}, F_{rv}, F_{r\varepsilon}$ are demonstrated as below.

$$F_{rr} = \begin{bmatrix} 0 & 0 & \frac{-\hat{v}_n}{(R_M+h)^2} \\ \frac{\hat{v}_e sin(\hat{\varphi})}{(R_N+\hat{h})cos(\hat{\varphi})^2} & 0 & \frac{-\hat{v}_e}{(R_N+\hat{h})^2 cos(\hat{\varphi})} \\ 0 & 0 & 0 \end{bmatrix} \tag{2.61a}$$

$$F_{rv} = \begin{bmatrix} \frac{1}{(R_M+\hat{h})} & 0 & 0 \\ 0 & \frac{1}{(R_N+\hat{h})cos(\hat{\varphi})} & 0 \\ 0 & 0 & -1 \end{bmatrix} \tag{2.61b}$$

$$F_{r\varepsilon} = \begin{bmatrix} 0 & 0 & 0 \\ 0 & 0 & 0 \\ 0 & 0 & 0 \end{bmatrix} \tag{2.61c}$$

2.6.2.2 Velocity Error Model

The velocity change under geographic frame can be estimated as Eq.(2.62) present

$$\dot{\hat{V}}_e^n = f^n - Pf^n + \hat{R}_b^n \Delta f^b + g^n - \delta g^n - (\hat{\omega}_{en}^n + 2\hat{\omega}_{ie}^n)\hat{V}^n \tag{2.62}$$

Subtract Eq.(2.62) − Eq.(2.53),and linearised the result, the velocity error can be expressed as

$$\delta\dot{V} = F_{vr}\delta P + F_{vv}\delta V + F_{v\varepsilon}\varepsilon - R_b^n \delta f^b \tag{2.63}$$

where $P = \varepsilon(\times)$, and the F_{vr}, F_{vv} and $F_{v\varepsilon}$ can be expressed as

$$F_{vr} = \begin{bmatrix} 2\sigma(V_u sin\varphi + V_N cos\varphi) + \frac{V_E V_N}{(R_N+h)cos^2\varphi} & 0 & \frac{V_E V_U}{(R_N+h)^2} - \frac{V_E V_N tan\varphi}{(R_N+h)^2} \\ -2\sigma V_E cos\varphi - \frac{V_E^2}{(R_N+h)cos^2\varphi} & 0 & \frac{V_{R_N} V_U}{(R_M+h)^2} + \frac{V_E^2 tan\varphi}{(R_N+h)^2} \\ -2\sigma V_E sin\varphi & 0 & -\frac{V_E^2}{(R_N+h)^2} - \frac{V_{R_N}^2}{(R_M+h)^2} + \frac{2g}{R+h} \end{bmatrix} \tag{2.64a}$$

$$F_{vv} = \begin{bmatrix} \frac{V_N tan\varphi}{R_N+h} - \frac{V_U}{R_N+h} & 2\sigma sin\varphi + \frac{V_E tan\varphi}{R_N+h} & -2\sigma cos\varphi - \frac{V_E}{R_N+h} \\ -2\sigma sin\varphi - \frac{2V_E tan\varphi}{R_N+h} & -\frac{V_U}{R_M+h} & -\frac{V_N}{M+h} \\ 2\sigma cos\varphi + \frac{2V_E}{R_N+h} & \frac{V_N}{R_M+h} & 0 \end{bmatrix} \tag{2.64b}$$

$$F_{v\varepsilon} = \begin{bmatrix} 0 & f_U & -f_N \\ -f_U & 0 & f_E \\ f_N & -f_E & 0 \end{bmatrix} \tag{2.64c}$$

2.6.2.3 Attitude Error Model

From Eq.(2.56), the attitude error model can be expressed in linear model as the Eq.(2.65) presented below:

$$\dot{\varepsilon} = \hat{R}_b^n(\delta\omega_{ib}^b - \delta\omega_{in}^b) \tag{2.65}$$

The following steps aim to linearise the Eq.(2.65) with respect to $\delta P, \delta V$ and $\delta\varepsilon$ and the gyro sensor error $\delta\omega_{ib}^b$,

The inertial rotation represent in body-frame with respect in n-frame can be expressed as

$$\omega_{in}^b = R_n^b \omega_{in}^n \tag{2.66}$$

The derivation of $\delta\omega_{in}^{b}$ can be formed as Eq.(2.67),

$$\delta\omega_{in}^{b} = \hat{R}_{n}^{b}(\delta\omega_{in}^{n} - P\hat{\omega}_{in}^{n}) \tag{2.67}$$

Substitute Eq.(2.67) to Eq.(2.65),

$$\dot{\varepsilon} + \hat{\omega}_{in}^{n}\varepsilon = -\delta\omega_{in}^{n} + R_{b}^{n}\delta\omega_{ib}^{b} \tag{2.68}$$

since $\delta\omega_{in}^{n} = \omega_{in}^{n} - \hat{\omega}_{in}^{n}$, after Taylor expansion

$$\delta\omega_{in}^{n} = [\frac{\partial\hat{\omega}_{in}}{\partial\hat{\varepsilon}}, \frac{\partial\hat{\omega}_{in}}{\partial\hat{V}}] \begin{bmatrix} \delta\varepsilon \\ \delta V \end{bmatrix} \tag{2.69}$$

Therefore, finally,

$$\dot{\varepsilon} = F_{\varepsilon P}\delta P + F_{\varepsilon V}\delta V + F_{\varepsilon\varepsilon}\delta\varepsilon + \hat{R}_{b}^{n}\delta\omega_{ib}^{b} \tag{2.70}$$

Where

$$F_{\varepsilon r} = \begin{bmatrix} 0 & 0 & -\frac{V_N}{(R_M+h)^2} \\ \sigma sin\varphi & 0 & \frac{V_E}{(R_N+h)^2} \\ -\sigma cos\varphi - \frac{V_E}{(R_N+h)cos^2\varphi} & 0 & \frac{V_E tan\varphi}{(R_N+h)^2} \end{bmatrix} \tag{2.71a}$$

$$F_{\varepsilon v} = \begin{bmatrix} 0 & \frac{1}{R_M+h} & 0 \\ -\frac{1}{R_N+h} & 0 & 0 \\ -\frac{tan\varphi}{R_N+h} & 0 & 0 \end{bmatrix} \tag{2.71b}$$

$$F_{\varepsilon\varepsilon} = \begin{bmatrix} 0 & \sigma sin\varphi + \frac{V_E tan\varphi}{R_N+h} & -\sigma cos\varphi - \frac{V_E}{R_N+h} \\ \sigma sin\varphi - \frac{V_E tan\varphi}{R_N+h} & 0 & \frac{V_N}{R_M+h} \\ \sigma cos\varphi + \frac{V_E}{R_N+h} & \frac{V_N}{R_M+h} & 0 \end{bmatrix} \tag{2.71c}$$

2.7 LiDAR Mechanization

LiDAR transmit and receive the light signal to measure the distance and angle between the sensor and surrounded obstacles. Obviously, these collected data cannot be used in navigation directly. A series of navigation algorithms are required to process scanning and matching technique [20] which is the common technology in LiDAR navigation. The following sections introduce the relevant theories of LiDAR navigation.

2.7.1 Polar Coordinates and Euclidean Coordinates

The distance and angle which measured by LiDAR are expressed in polar coordinate (ρ, α). To convert the polar coordinate to euclidean coordinate,the relationship between the polar coordinate and the euclidean coordinate can be expressed as

$$x = \rho \times cos\alpha \tag{2.72a}$$

$$y = \rho \times sin\alpha \tag{2.72b}$$

Figure 2.8 also present the relationship between the polar coordinate and euclidean coordinate.

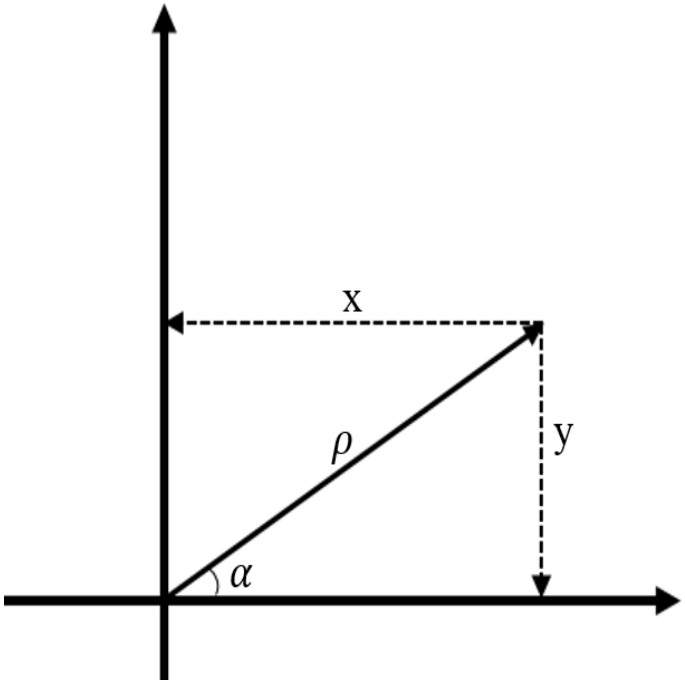

Figure 2.8: Polar Coordinate and Euclidean Coordinate

2.7.2 LiDAR Navigation Mechanization

Unlike the satellite based absolute navigation, the LiDAR navigation is a relative navigation. This relative navigation approach is demonstrated as Figure 2.9, the blue squares represent the location of the LiDAR sensor at time i and $i+1$ respectively, the position of the perpendicular intersection point in Cartesian coordinate can be expressed as (x_i, y_j) corresponding to LiDAR measurement is (ρ_i, α_i). At time $i+1$, the position of the perpendicular intersection point in Cartesian coordinate is (x_{i+1}, y_{j+1}) with corresponding Polar coordinate $(\rho_{i+1}, \alpha_{i+1})$.

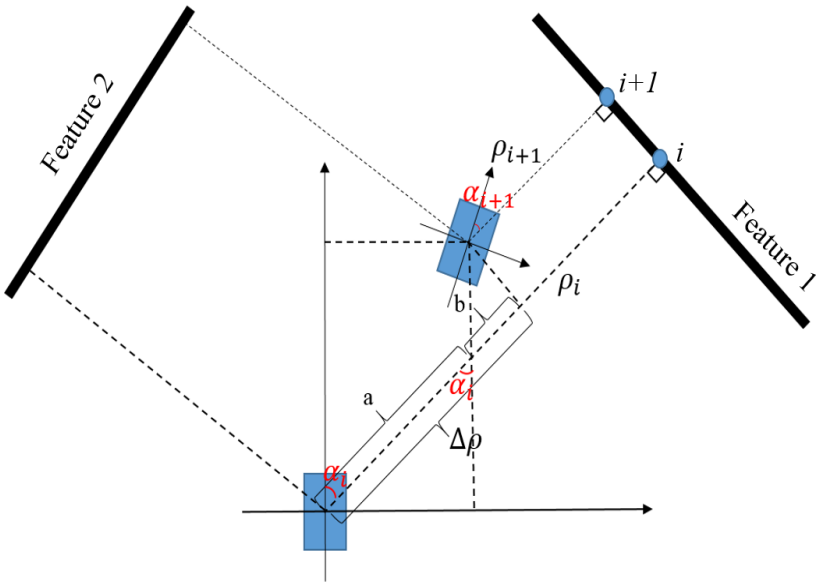

Figure 2.9: LiDAR Operation Diagram

As Figure 2.9 shows, the feature 1 and feature 2 are the extracted line feature from the surround obstacle which are considered as the reference location. The position change of LiDAR sensor from time i to time $i+1$ is equal to $(\Delta x, \Delta y)$ in Cartesian coordinate. The perpendicular distance difference between the same feature to the LiDAR sensor $\Delta\rho$ from time i to $i+1$ is expressed as Eq.(2.73)

$$\begin{aligned} \Delta\rho &= \rho_i - \rho_{i+1} \\ &= a + b \end{aligned} \tag{2.73}$$

where

$$a = \frac{\Delta x}{sin\alpha} \tag{2.74a}$$

$$b = \Delta\rho - a \tag{2.74b}$$

As Figure 2.9 illustrated, Δy can be expressed as Eq.(2.75),

$$\Delta y = a \cdot cos\alpha + \frac{b}{cos\alpha} \tag{2.75}$$

Substitute Eq.(2.74) into Eq.(2.75), Eq.(2.75) can be represented as Eq.(2.76)

$$\Delta y = \frac{\Delta x}{sin\alpha} \cdot cos\alpha + (\Delta\rho - \frac{\Delta x}{sin\alpha}) \cdot \frac{1}{cos\alpha} \tag{2.76}$$

Finally we have the relationship between the relative Cartesian coordinate $(\Delta x, \Delta y)$ and the Polar coordinate $(\Delta\rho, \Delta\alpha)$

$$\begin{aligned} cos\alpha sin\alpha\Delta y &= -sin^2\alpha\Delta x + sin\Delta\rho \\ \Delta\rho &= cos\alpha\Delta y + sin\alpha\Delta x \end{aligned} \tag{2.77}$$

The azimuth difference can be expressed as

$$\Delta\alpha = \alpha_{i+1} - \alpha_i \tag{2.78}$$

In relative positioning, at least two non-collinear line features are required for the displacement vector estimation. The measurement matrix can be denoted as

$$z = \begin{bmatrix} \rho_i(1) - \rho_{i+1}(1) \\ \dots \\ \rho_i(n) - \rho_{i+1}(n) \end{bmatrix} \tag{2.79}$$

where n represents the total number of the extracted line in one scanning circle. The transient matrix H can be expressed as

$$H = \begin{bmatrix} cos(\alpha_i)(1) & sin(\alpha_i)(1) \\ \dots & \\ cos(\alpha_i)(n) & sin(\alpha_i)(n) \end{bmatrix} \tag{2.80}$$

Then in the matrix form, if there are n number lines can be extracted, the LiDAR navigation equation can be expressed as Eq.(2.81)

$$\begin{bmatrix} \rho_i(1) - \rho_{i+1}(1) \\ \dots \\ \rho_i(n) - \rho_{i+1}(n) \end{bmatrix} = \begin{bmatrix} cos(\alpha_i)(1) & sin(\alpha_i)(1) \\ \dots & \\ cos(\alpha_i)(n) & sin(\alpha_i)(n) \end{bmatrix} \begin{bmatrix} \Delta x \\ \Delta y \end{bmatrix} \tag{2.81}$$

2.8 Summary

This chapter introduced the structure of the GPS receiver and signal. As a BPSK modulated signal, a better understanding of the characteristics of the modulated code and message can benefit the design of an efficient acquisition and tracking approach. Furthermore, several GPS inaccurate sources have been discussed and

evaluated in order to avoid or reduce the error and inaccuracies which are generated by these sources. In addition, to design a robust and efficient multisensor integrated navigation scheme, several sensors and their related theory are reviewed, such as the concepts of different coordinate frames and their transformation algorithms, IMU navigation mechanization and its error model, relevant navigation theory and Line feature extraction for LiDAR navigation. All this relevant information and theory will feature in the following chapters.

Chapter 3

Effective Signal Acquisition through Low-cost Dual Polarized GPS antenna

3.1 Introduction

As mentioned before, a 50 bps navigation code and a pseudorandom code are modulated on a 1575.42 MHz L1 band carrier frequency. The civilian pseudorandom codes are called Coarse and Acquisition (C/A) codes and the frequency is 1.023 MHz. Benefiting from the C/A codes high correlated characteristic, even when the transmission distance between the receiver and the satellites is more than 22,000 km, the receiver still can distinguish each individual satellite signal.

The GPS L1 band signal is a right hand circular polarized(RHCP) electromagnetic(EM) wave. Conventional GPS antennas could collect this EM wave in order to allow the receivers to process the acquisition and tracking, eventually decoding the navigation message and calculating the user location. However, in a very dense multipath environment, the RHCP EM wave could become the LHCP EM wave after several occurrences of reflection. Normally, the anti-multipath antenna are designed to reject the reflected signal to reduce the multipath effect, however this method could reduce the quantity of the acquired satellites. As we mentioned in the previous chapter, the more satellites signal received, the better positioning accuracy can be achieved. Therefore, acquiring more satellites is the main concern to improve the positioning performance especially under the harsh environment.

It is intuitive that in a very dense multipath environment, when the RHCP signal is rare, a LHCP signal become sufficient. Simply rejecting the LHCP signal is not an efficient method to obtain better performance in multipath environments. Studies such as [35] [7], thus successfully implement a LHCP signal in sensing and altimetry, have proved that LHCP signal is not completely useless. Therefore, using LHCP signal to provide aiding information when direct signal is not strong is an optimal and efficient approach. To collect the LHCP signal, a dual polarization patch antenna is designed. The dual polarization patch antenna is low cost and able to collect both direct and reflected signals. Furthermore, implementation of the software based GPS receiver [36] can provide an excellent research platform for investigating the performance of the dual polarization patch antenna with the novel acquisition approach. The acquisition approach is the first step of the GPS baseband signal processing and the condition of the navigation message decoding. A sensitive and efficient acquisition approach can benefit the performance of the GPS receiver.

In this chapter, several conventional GPS signal acquisition approaches have been reviewed, e.g., serial searching, and FFT based parallel searching. Furthermore, after comparing and analyzing the existing acquisition approach, a modified serial searching approach and a dual polarization antenna are designed and implemented in order to acquire the weak signal in a very dense multipath environment.

3.2 Acquisition Approaches

Within GPS signal processing, acquisition is the primary and crucial process to coarsely estimate the code phase and Doppler frequency band. The performance of the GPS receiver is highly depended on the speed and the accuracy of the acquisition result. The following sections will review and evaluate several conventional acquisition approaches and propose a novel acquisition approach named modified serial searching acquisition approach.

3.2.1 Signal Serial Searching Acquisition

GPS acquisition is a processing of 3D searching include 41 frequency searching band, 32 sequence of C/A code, and 1023 chips within a C/A code. Serial searching is the most simplest and straightforward acquisition algorithm. A non-coherent correlator

is used since the phase of the received signal is random. As the Figure 3.1 illustrate, first of all, the received IF signal will multiply the replicated CA which is generated by the local generator [5]. Local CA code generator creates 32 sequence of CA code correspond to 32 satellites from 0-1022, total is 32736 code. Then the local oscillator generate two local carrier frequency signal with 90° difference. The incoming IF signal x_t mix with the replica C/A code and the local carrier frequency signal to generate I and Q component. Afterwards the I and Q signal will be integrated for a specific length of time. Typically, the integration length is 1 ms to correspond 1 C/A code length.

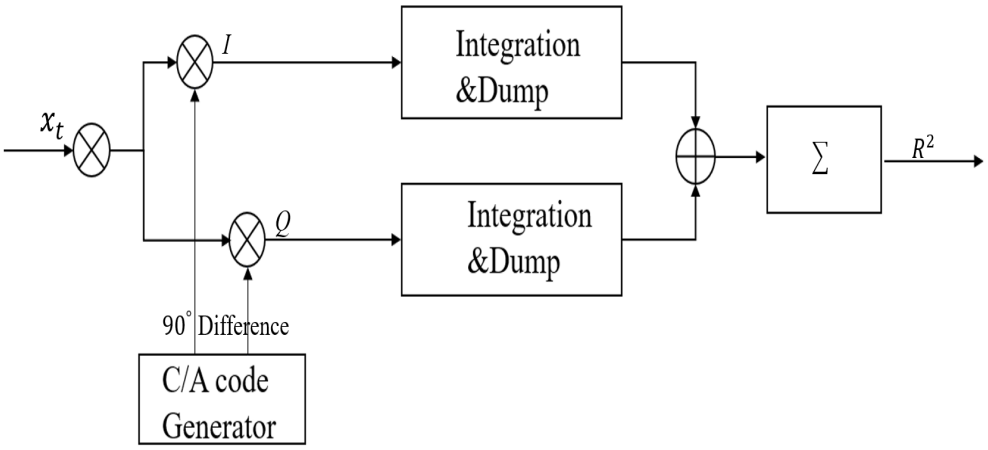

Figure 3.1: Generic serial searching Acquisition

Normally, the Doppler shift is roughly $\pm 10KHz$, therefore the receiver must search in $20KHz$ band for visible GPS signal in order to cover all the Doppler shift. The optimal Doppler frequency searching bin size is $500Hz$ this gives total 41 different frequencies to be searched for a band of $20KHz$. Next step of serial searching acquisition is integration and squaring, integration perform sum function of all points corresponding to the length of the processed data. Squaring is introduced to obtain the signal power. Finally the I and Q components are sum together. If the replica code is well aligned with the incoming code, the result will significantly higher than the others. The serial searching result R can be presented as Eq.(3.1)

$$R = \sum_{j=0}^{K-1} \left(\left[\sum_{t=jNL}^{(j+1)NL-1} x[t] \cdot CA[t] \cdot cos[\Omega t] \right]^2 + \left[\sum_{t=jNL}^{(j+1)NL-1} x[t] \cdot CA[t] \cdot sin[\Omega t] \right]^2 \right) \tag{3.1}$$

where t represent th t_{th} sample, L is the total samples within one period of C/A code.

N represents the total number of the period need to be integrated. Serial searching acquisition is a deep and complete searching approach, thus it is very sensitive to weak signal however the computation cost is high since it needs to search all 41 frequency band and 2046 code total in 83886 unit.

3.2.2 Parallel Frequency Space Search Acquisition

In [37], a parallel frequency searching approach has been presented. Instead of searching 41 frequency band one by one, this fast Fourier transform (FFT) based parallel searching approach can search all 41 band in one time. As Figure 3.2 presents, the IF signal x_t perform correlation process with the replica C/A code, the correlation result will process a Fourier transform, therefore the correlation result in time domain become frequency strength in frequency domain.

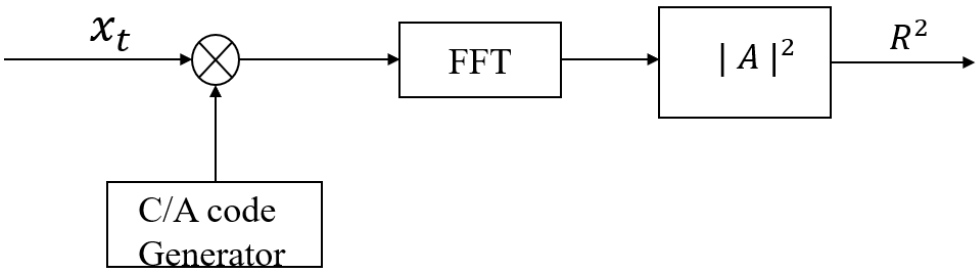

Figure 3.2: Parallel Frequency Space search Acquisition

If the incoming signal has a well align with the local generate PRN code, the outcome signal will become continuous and have a distinct peak in magnitude. The accuracy of the determined frequency depends on the length of the DFT.

3.2.3 Parallel Code Phase Search Acquisition

Parallel frequency space search reduce the 41 $\times$ 2046 combinations to 1 $\times$ 2046 combinations via Fast Fourier transform. However, it is obviously that the amount of code phase dimension is larger than frequency dimension, therefore reduce the number of code searching can significantly improve the acquisition speed.

As the Figure.3.3 presents, digitized IF signal will be multiplied by a local oscillator generated carrier signal with 90° phase shifted. Therefore, the input signal x_t represent in discrete form is $x(n)$, the complex form can be expressed as $x(n) = I(n) + jQ(n)$, then the FFT of this input signal need to be computed, the FFT result multiply with the complex conjugate of CA code. This is because of

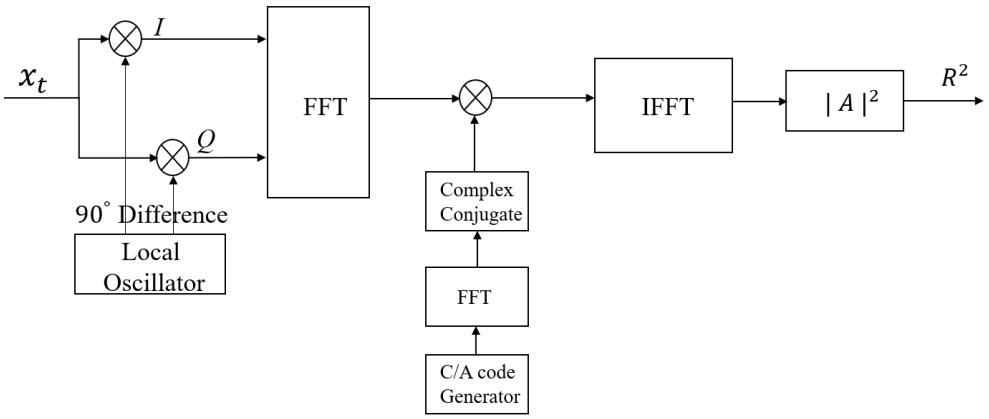

Figure 3.3: Parallel Code phase search Acquisition

the process of autocorrlation in time domain is equivalent to the process of multiplication in frequency domain. Finally, the product of income signal and PRN code conjugate will convert back to time domain by Inverse Fast Fourier transform. In one PRN code and 41 frequency band, phase of CA code does not need to be shifted, therefore, the replica PRN code can be stored and reused in different frequency.

The equivalence of autocorrelation and Fourier transform is presents as Eq.(3.2-3.4) The correlation value $z(n)$ of two periodic sequence number $x(n)$ and $y(n)$ are presented as Eq.3.2:

$$z(n) = \frac{1}{N}\sum_{m=0}^{N-1} x(m)y(m-n) \tag{3.2}$$

Based on the discrete Fourier transform

$$X_m = \sum_{n=0}^{N-1} x_n e^{-2\pi jnm/N} \tag{3.3}$$

The result of correlation value $z(n)$ perform DFT

$$\begin{aligned} Z(k) &= \sum_{n=0}^{N-1} z_n e^{-2\pi jnm/N} \\ &= \frac{1}{N}\sum_{m=0}^{N-1} x(m)y(m-n)e^{-2\pi jnm/N} \\ &= \frac{1}{N}\sum_{m=0}^{N-1} x(m)e^{-2\pi jnm/N}\sum_{m=0}^{N-1} y(m-n)e^{-2\pi jnm/N} \\ &= \frac{1}{N}X(K)\bar{Y}(K) \end{aligned} \tag{3.4}$$

In Eq.(3.4) $X(k)$ and $Y(k)$ are and DFFT result of $x(n)$ and $y(n)$, and $\bar{Y}(k)$ is the

conjugate value of complex number $y(n)$. Equation 7 proves the correlation value of two sequences in time domain equal the product of these two sequence's DFT value in frequency domain. Vice versa, product of two DFT values $X(k)\bar{Y}(k)$ equal the correlation value $z(n)$ in time domain. Once the receiver obtain the value $z(n)$ through inverse Fourier transform, then the rest parts are the same as serial search approach.

The computational time of parallel code phase search approach is significantly reduced compared to the previous two approach [38], however code phase searching approach needs to perform two times of Fourier transform algorithm for every frequency band search. In order to reduce the computational time, two methods can be deployed: first the CA code is not changed if it is from the same satellite, therefore the Fourier transform value and its conjugate value can be stored in receiver. Second, input IF signal is constant no matter which frequency band needs to be searched, therefore the Fourier transform result multiply the carrier signal is a constant as well, this result can be shared by different satellite PRN code searching within same frequency band.

3.3 A Modified GPS Serial Searching Approach

After comparing and analysing the pros and cons of the parallel searching and serial searching acquisition approaches, a modified serial searching based approach is proposed in order to acquire low strength GPS signals. Furthermore, a dual polarization patch antenna is designed in order to acquire left hand polarization signal. As we have discussed previously, serial searching acquisition is simpler to implement and more sensitive to weak signals, but the computational cost is relatively higher compare to FFT based parallel searching. Therefore, we propose a step jumping serial searching acquisition method to reduce serial searching computation cost while still retaining sensitivity to weak signals.

In our proposed algorithm, the input signal $x[n]$ is sampled at f_s Hz and correlated with the locally generated replica C/A code, unlike the conventional serial searching processing which every single bit need to be processed, a sliding step size i is implement to reduce the computation cost. This is mathematically given as

Eq.(3.5),

$$R^2[m] = \sum_{j=0}^{(K-1)N/i} ([\sum_{n=ij+1}^{(j+1)NL-1+ij} x[n]\mathbf{Re}CA[n]cos(2\pi f_c)]^2 + [\sum_{ij+1}^{(j+1)NL-1+ij} x[n]\mathbf{Im}CA[n]sin(2\pi f_c)]^2) \tag{3.5}$$

The input signal $x[n]$, which range is identified from $x[1]$ to $x[NL]$ to perform the correlation process with the same length replica C/A code. Unlike the conventional serial searching approach, in step jumping method, if the beginning sample is not found in the first range then the input signal jumps to the next range from $x[ji+1]$ to $x[NL+ji]$. Due to the C/A code high correlative property, the correlation results will retain the same even a reasonable size i of bits is skipped. Therefore the the computation cost can be reduced i times compare to the conventional serial searching method. A higher step size can reduce the computation cost but the sensitivity will be effected at the same time. In order to mitigate this trade off, the maximum step value needs to be carefully chosen. The beginning of the C/A code could be missed if the step size value exceed the number of the samples in one chip. Due to the chip rate of the C/A code being $1.023MHz$, the maximum step i equals $\frac{fs}{1.023\times10^6}$. An experiment which aims to compare processing time was conducted with a sampling frequency f_s equal to $8MHz$, meaning the maximum step value was 8. The comparison results are illustrated in Figure 3.4 and the step jumping method with a step value equal to 5 and 8 are much faster than conventional serial searching, especially when the number of periods N is more than 1. Therefore, the step jump searching reveals a significant advantage compared to conventional serial searching when N is a higher value. Figure 3.5 and Figure 3.6 demonstrate the C/A code correlation result of PRN 4, the results indicate that the with a significantly improve the processing time, the results still retain the same.

3.4 Dual Polarization Patch Antenna Design and Testing

To adopt the GPS signal acquisition under a very massive multipath environment, we propose a dual polarization attach to collect both direct and reflect GPS signal,

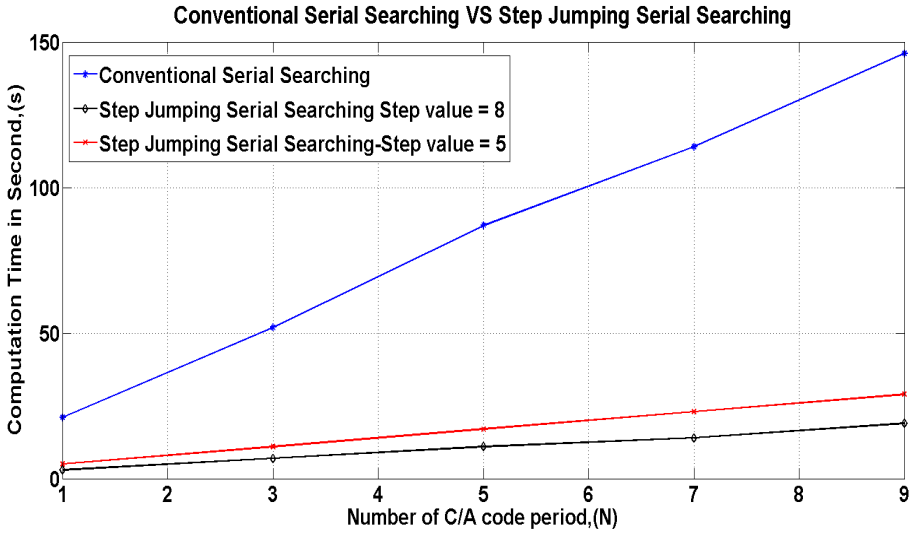

Figure 3.4: Processing Time Comparison

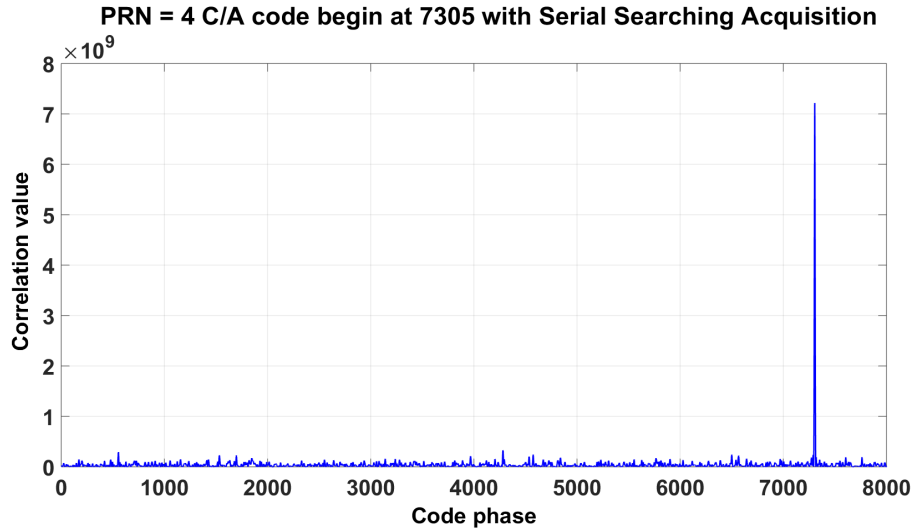

Figure 3.5: Acquisition Results from Conventional Approach

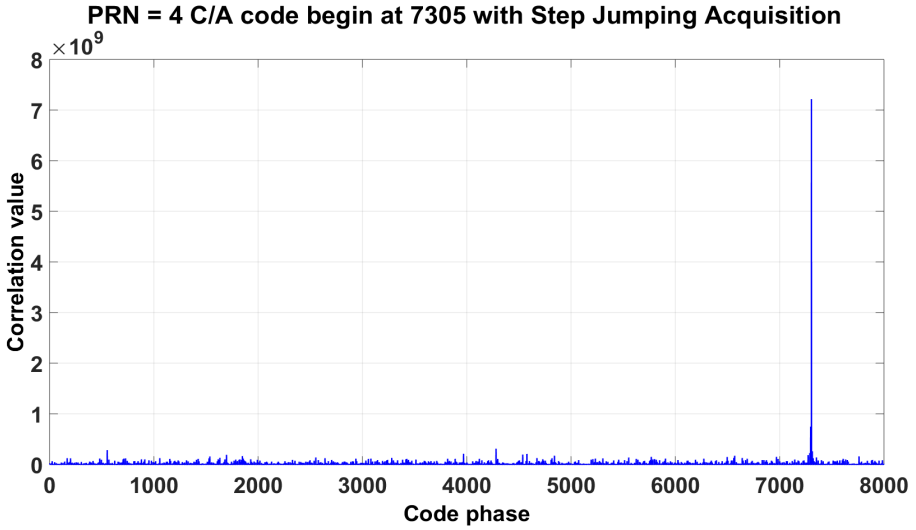

Figure 3.6: Acquisition Results from Step Jumping Approach

a dual polarization patch antenna is designed and tested in the following sections.

3.4.1 Patch Antenna Design

As we know, a directly received GPS signal is a right hand polarization electromechanical (EM) wave. However, after several times of reflection, GPS signal may become left hand polarization, especially under a very dense multipath environment. Conventional GPS antenna is a RHCP antenna which aims to reject LHCP signal to reduce the multipath effect. Therefore, in order to improve the acquisition ability of the GPS receiver under a multipath environment, a dual polarization antenna is proposed and designed. To reduce the antenna cost, this dual polarization antenna is designed as a patch antenna.

A patch antenna, also known as a microstrip antenna, to ensure the transmission wave is available, a matched load needs to be added at the end of the microstrip antenna [39]. To avoid the dual polarization interference effect, the technical parameters of the designed patch antenna need to be carefully selected. Since the designed antenna aims to collect the GPS L1 band, its center frequency 1575.42 MHz is one of the concern to the designed patch antenna. In another word, the frequency range of the patch antenna need to correspond to the center frequency of the GPS L1 band.

The Voltage standing wave ratio(VSWR) is another crucial parameter, in which decided by reflected coefficient. To an antenna, a small amount of the energy will be reflected when EM waves are transmitted from one medium to another. The ideal value of VSWR is 1, means that the reflection coefficient is zero and there is no reflection from the antenna. The value of VSWR can be obtained as Eq.(3.6) Eq.(3.6)

$$VSWR = \frac{1 + |\Gamma|}{1 - |\Gamma|} \tag{3.6}$$

FR4 is a typical PCB material which is commonly used as a substrate in patch antennas. FR4 is a low cost and general material with permittivity ε_r of is 4.7 and its thickness is 1.55 mm [40]. The sizes of the GPS patch antenna are calculated

using Eq.(3.7) and Eq.(3.8)

$$W = \frac{c}{2f_r}\sqrt{\frac{2}{\varepsilon_r + 1}} \tag{3.7}$$

$$L = L_{eff} - 2\Delta L \tag{3.8}$$

where W and L are the width and length of the patch antenna, ε_r is the permittivity of FR4 which is equal to 4.7, c is the velocity of light, f_r is the resonate frequency, ΔL is the length of the radiation slots and L_{eff} is the length of the radiation defined as Eq.(3.9) presented

$$L_{eff} = \frac{C}{2f_r\sqrt{\varepsilon_{eff}}} \tag{3.9}$$

where ε_{eff} is the effective electric constant that can be calculated as below

$$\varepsilon_{eff} = \frac{(\varepsilon_r + 1) + (\varepsilon_r - 1)\sqrt{\frac{1+12h}{W}}}{2} \tag{3.10}$$

h is the thickness of the substrate and it is given as 1.55 mm. Since the electric constant has been calculated, radiation slots can also be obtained by [41].

$$\Delta L = 0.412h\frac{(\varepsilon_{eff} + 0.3)(\frac{W}{h} - 0.264)}{(\varepsilon_{eff} - 0.258)(\frac{W}{h} + 0.8)} \tag{3.11}$$

Since we are designing a dual polarization antenna, both LHCP and RHCP antenna are attaches on the same substrate, the interference from each individual antenna need to be considered and minimized. To reduce the interference effect from two antennas, one wavelength distance from one patch antenna center to another center is required.

Furthermore, the GPS signal is EM wave, to reduce the patch size and enhance the bandwidth, each patch antenna need to truncate a corner [42]. The truncated size ΔS and truncated length l are dependent on the patch size S and Q-factor

which can be calculated use Eq.(3.12) and Eq.(3.13)

$$\Delta S| = \frac{S}{2Q} \tag{3.12}$$

$$l = L\sqrt{\frac{\Delta S}{S}} \tag{3.13}$$

where Q is the unloaded quality factor of the patch and associate to cavity mode 14 [43].

$$Q = \frac{C\sqrt{\varepsilon_r}}{4f_r h} \tag{3.14}$$

Through the calculations, the parameters of the patch antenna is listed as Table 3.1 The technique drawing of the patch antenna is presented as Figure 3.7

Table 3.1: Parameter of Patch Antenna

Width	55.8mm
Length	46mm
Truncated Size	19.4mm
Truncated Length	3.9mm

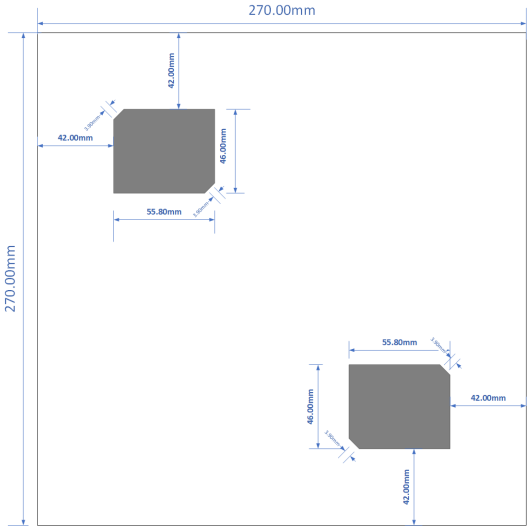

Figure 3.7: Antenna Technique Drawing

3.4.2 Patch Antenna Testing

To evaluate the performance of this designed patch antenna, a Miscowave CST studio is used. The testing results indicated that the designed patch antenna is

suitable for GPS L1 band LHCP and RHCP signal. The S11 indicates the amount of the power is reflected from the antenna. And this is also known as reflection coefficient Γ. As Figure 3.8 Figure 3.8 and Figure 3.9 Figure 3.9 indicate that the antenna radiates best at around 1.575 GHz and S11 is -30 dB. And rest of them will radiate nothing.

From the Figure 3.10 and Figur. 3.11 and their enlarged view Figure.3.10(B) and Figure 3.11(B),the VSWR is 1.06 for RHCP and 1.07 for LHCP.

One of the most important parameter for antenna design is the antenna radiation main lobe and side lobe. As Figure3.12 presents, the far field polar chart, the main lobe magnitude of RHCP is 7.18 dB and the side lobe is -18.8 dB and the main lobe magnitude of LHCP is 7.17 dB and the side lobe is -18.8 dB. This is proof that this dual patch antenna is suitable for GPS L1 band direct and reflected signal collection.

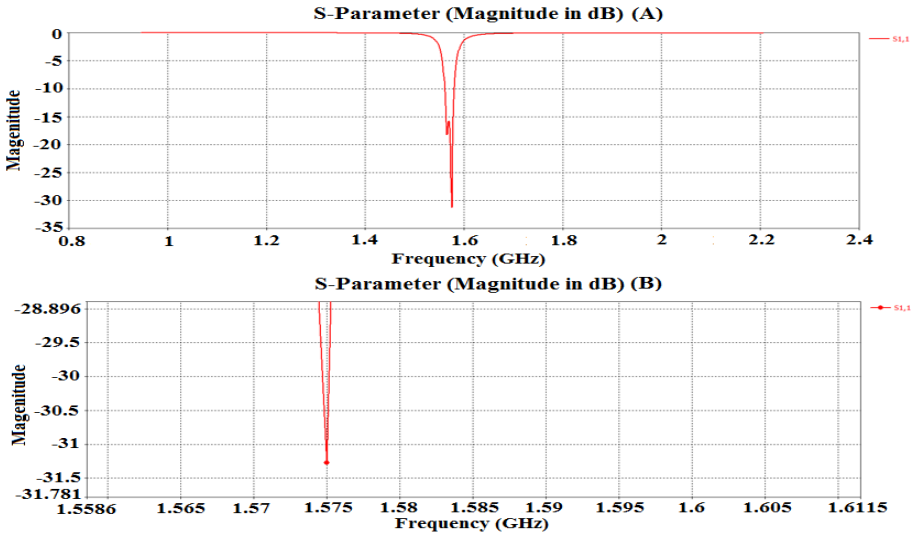

Figure 3.8: S parameter of RHCP signal

The simulation results has confirmed that this dual polarization patch antenna is suitable for the GPS L1 band and its reflected signal. Thus, the technique drawing of the patch antenna is presented as Figure 3.7 manufactured antenna is shown in Figure 3.13. In order to test the performance of the antenna, especially for reflected LHCP signal acquisition, a field test will be performed, a very dense multipath environment is chose to collect LHCP signal.

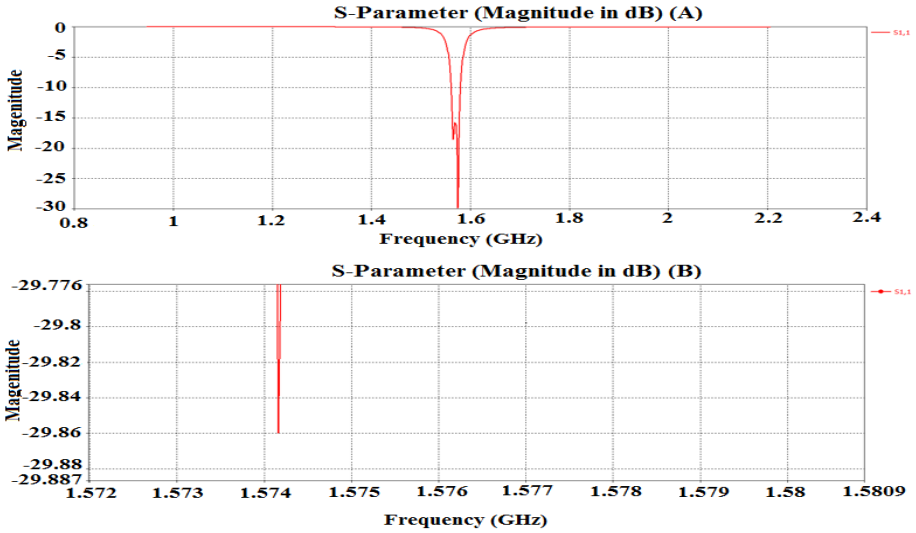

Figure 3.9: S Parameter of LHCP signal

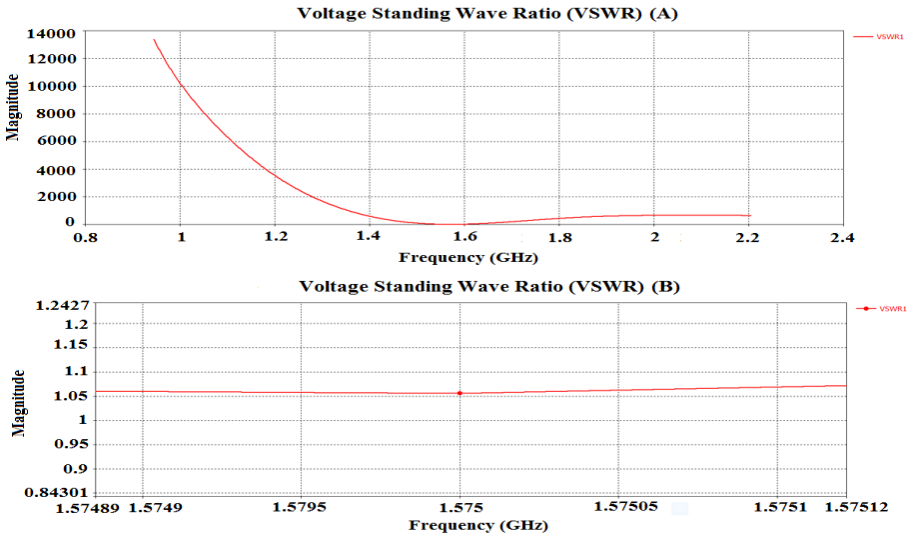

Figure 3.10: VSWR of RHCP signal

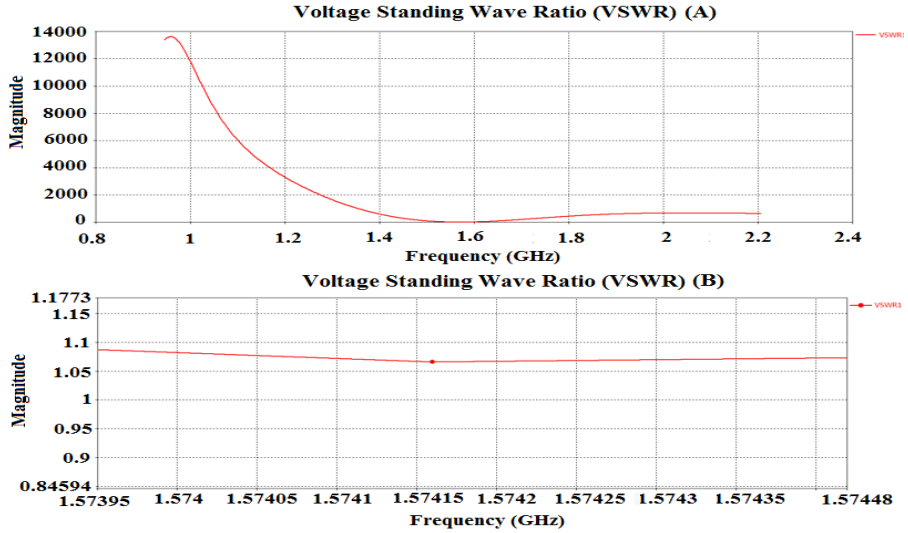

Figure 3.11: VSWR of LHCP signal

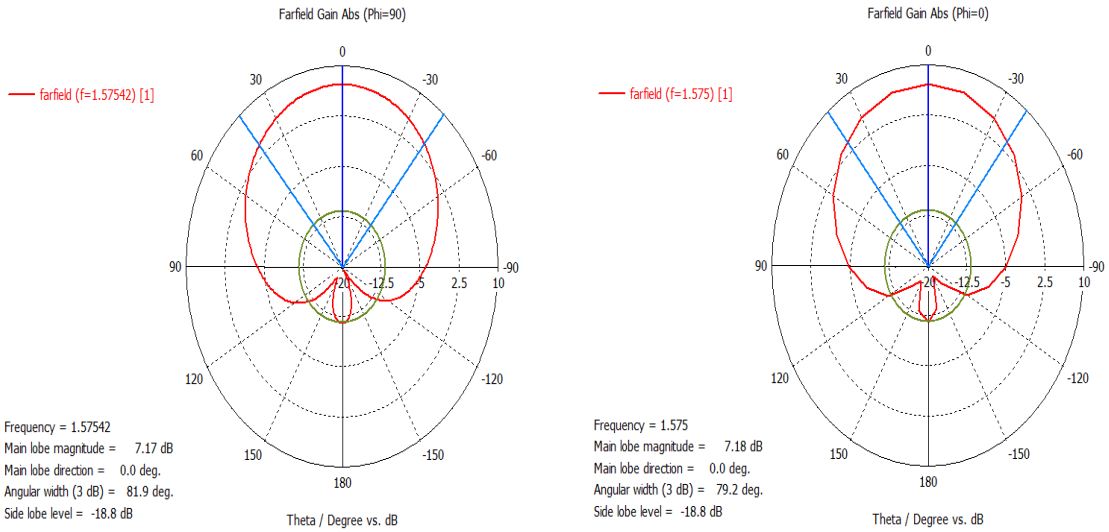

Figure 3.12: Left Hand Far Field Polar Chart vs Right Hand Far Field Polar Chart

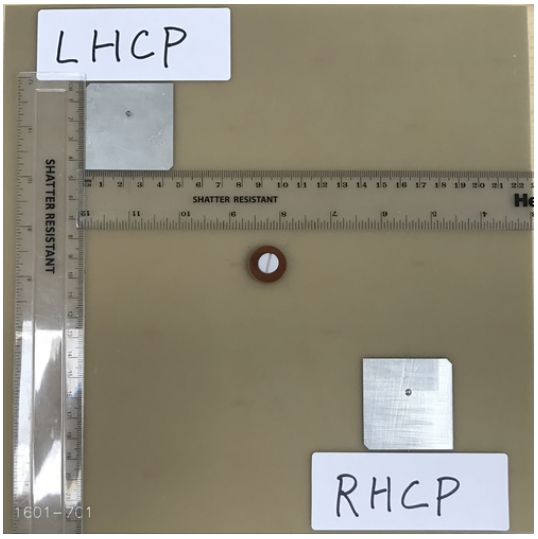

Figure 3.13: Passive Patch Antenna

3.5 Experiment Setup and Results Analysis

In order to implement GPS raw data collection, a USRP based GPS receiver is implemented and compared against a commercial GPS receiver as Figure 3.14 presented. The USRP receiver is consisted of a self designed dual-polarization patch antenna and a USRP. The USRP is used as a radio frequency front-end device. In our experiment, the USRP 2930 is chose, as the operation frequency is from 500 Hz to 2.2 GHz. Therefore, it is sufficient to process 1575.42 MHz GPS L1 band signal. The results are compared with a NovAtel GNSS stationary receiver which is attached by a Leica AC1203+ GNSS antenna. To obtain the same time error, the USRP based receiver is synchronized with NovAtel receiver.

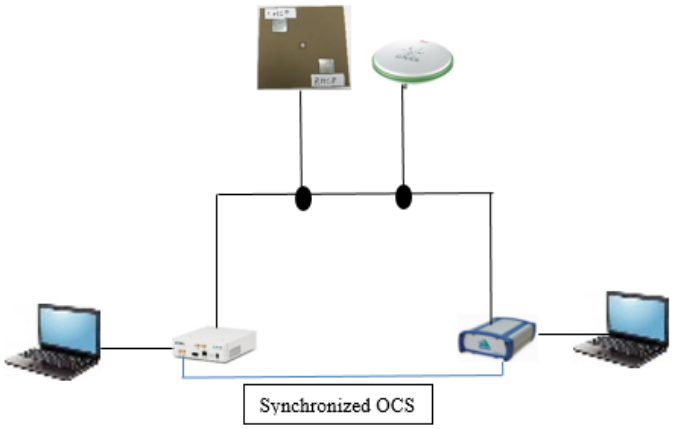

Figure 3.14: Connection Diagram

3.5.1 Experiment Setup and Location

The experiment was conducted in the center yard of Merz Court in Newcastle University as Figure 3.15 and Figure 3.16 demonstrated, this location is surrounded by tall buildings and considered as a very dense multipath environment. Under this kind of environment, directed GPS signal is much less than reflected signal. Due to the rapidly movement of the satellites, the different elevation angles play a significant role on the performance of acquisition. In order to test the reliability of the proposed acquisition approach, the experiment was undertaken for 3 successive days at the same time 12:40 pm to acquire the same satellites at uniform elevation angle. The GPS signal was recorded by both USRP based receiver and NovAtel commercial receiver.

The sampling frequency is set to be 5MHz since the C/A code is 2.045 MHz.

Figure 3.15: Experiment location

Figure 3.16: Experiment Environment and Data Collection

The center frequency is set to be 1575.42MHz corresponding to L1 band signals. The USRP based front-end collects the broad band signal and down-convert to intermediate frequency (IF) without any resolution lost, the received LHCP IF signal is collected and plotted in the time and frequency domain as Figure 3.17 and Figure 3.18 present. The IF signal appears as noise because of the high noise level. From Figure 3.18 we can see the center frequency of the IF signal is at $1.25MHz$, so based on the aforementioned Doppler effect, the Doppler searching domain $1.25MHz \pm 10kHz$ will be sufficient.

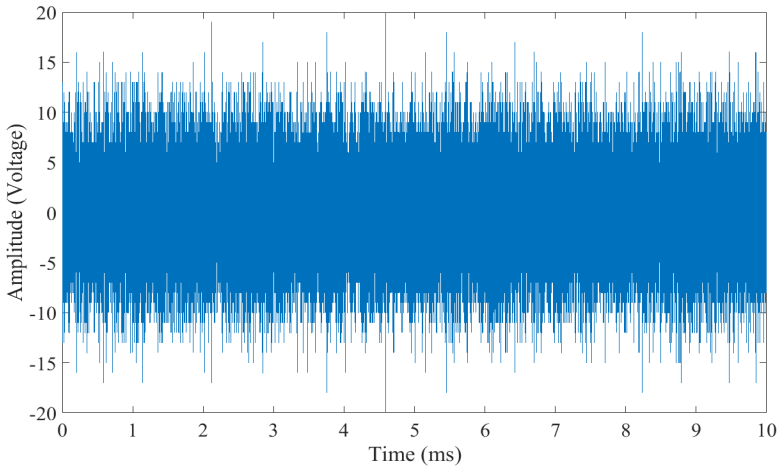

Figure 3.17: Raw IF GPS signal in Time Domain

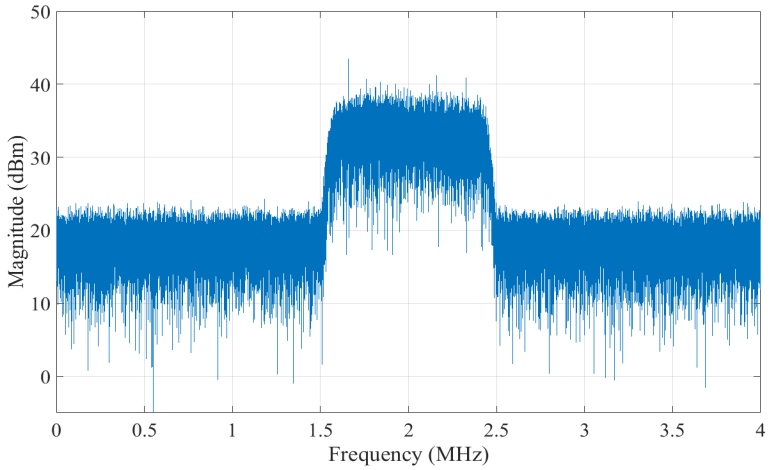

Figure 3.18: Raw IF GPS signal in Frequency Domain

3.5.2 Acquisition result Comparison and Analysis in Multi-path Environment

Acquisition results comparison are analyzed based on the commercial GPS receiver and USRP based receiver respectively. Consequently, the NovAtel GNSS receiver GUI (Graphic User Interface) in Figure 3.19 shows that only one satellite has successfully been acquired through the LHCP patch antenna under such an extreme environment.

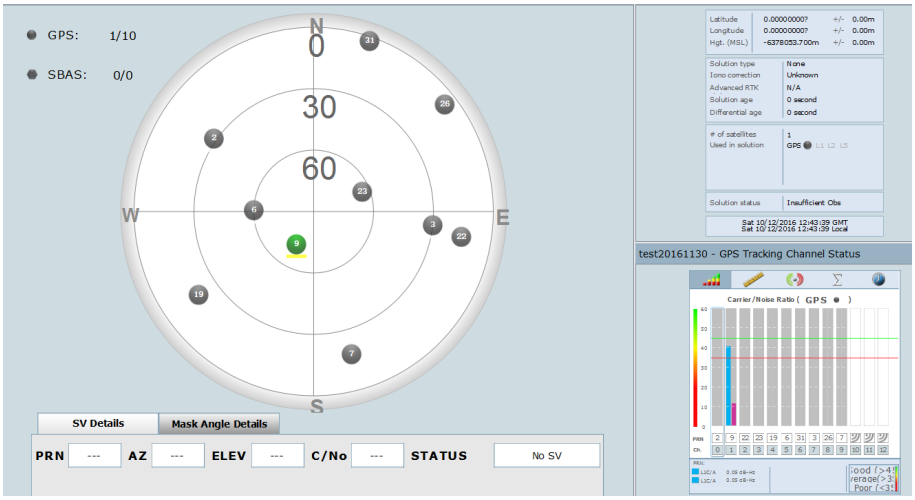

Figure 3.19: NovAtel GUI

Commercial GNSS receivers such as NovAtel, commonly implement FFT based parallel searching acquisition method to reduce the processing time, however under such an extreme environment, the received signal strength is lower than the noise level, the FFT output is obvious and cause the acquisition result fail. Nevertheless, step jumping serial searching method belong to the family of the serial searching can adopt in this scenario, since serial searching acquisition approach is sensitive to the low C/N_o signal.

The acquisition results of the raw data processing are presented in Figure 3.20-3.23. With the help of step jumping serial searching method, not only RN No. 9 has been successfully acquired, PRN No.7 also been acquired. The Figure 3.22 and 3.23 have presented the beginning of the code the is 3481 with frequency 1.2545 MHz. The acquisition result prove the advantages of the step jumping method and the superior performance compare to the commercial receiver.

The modified GPS signal acquisition approach through a dual polarization patch antenna has been introduced, the experiment results have proved the superior perfor-

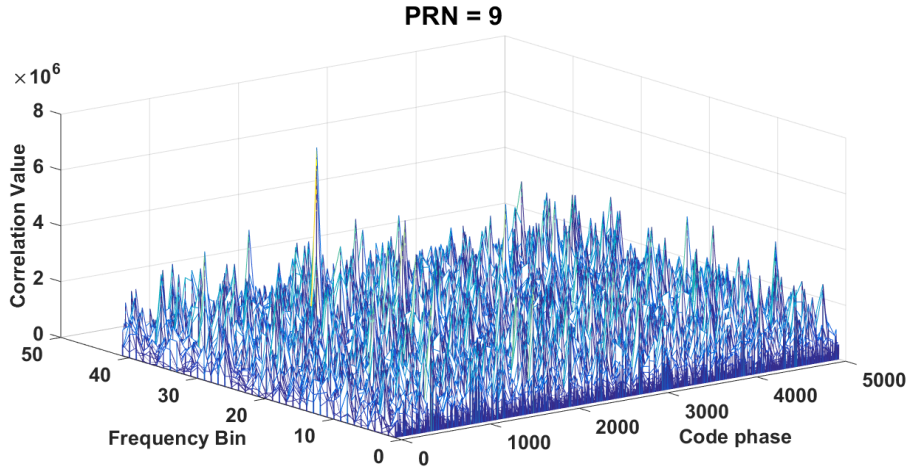

Figure 3.20: Acquisition matrix output from PRN 9

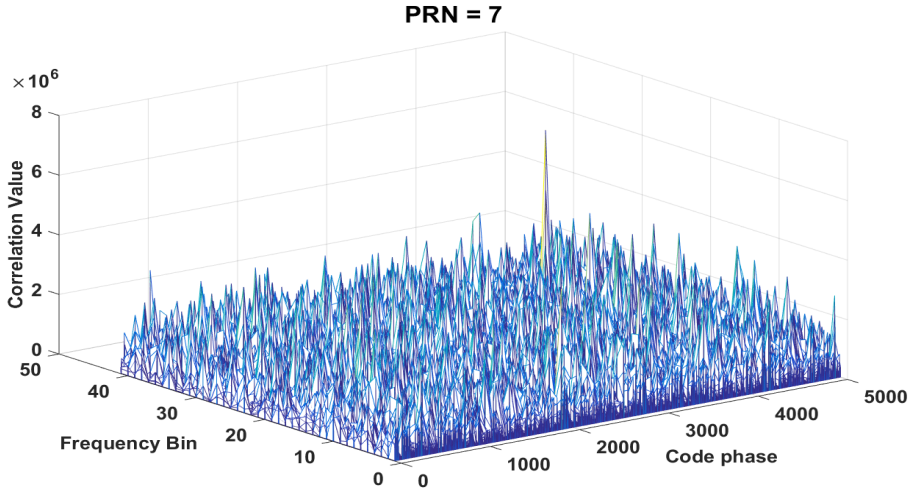

Figure 3.21: Acquisition matrix output from PRN 7

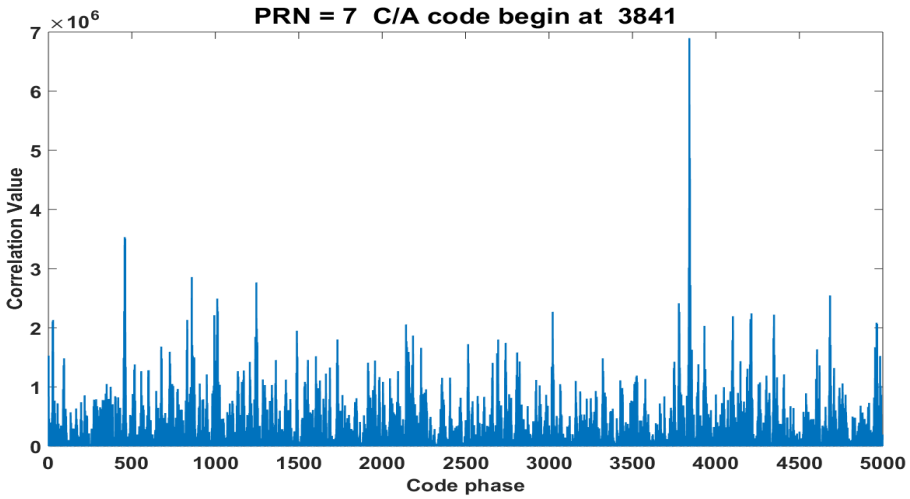

Figure 3.22: Code Phase Diagram

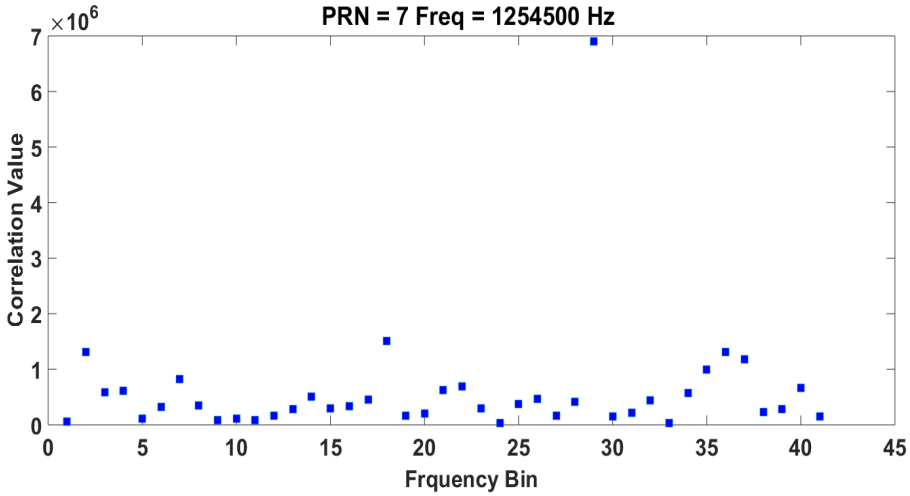

Figure 3.23: Doppler Frequency Shift Diagram

mance compare to the commercial receiver. The proposed method is more efficient to weak signal acquisition and can provide compensate signal source to aid GPS positioning

As we know, at least 4 satellites are successfully acquired, the GPS receiver can obtain a 3D location information. But in urban environment, this is a challenging condition, since multipath effects and low C/N_o are the frequently faced challenges, and degrade the GPS receiver performance. To mitigate these challenges, a dual polarization patch antenna with a step jump serial searching approach have been proposed and implement, as the experiment results indicate with the proposed solution, extra satellites signal can be successfully acquired. As the first step of GPS signal processing, acquisition is essential and critical, success acquire the extra GPS signal can significantly improve the performance of the GPS performance.

3.6 Summary

First, this chapter introduced the procedure of several GPS signal acquisition approaches and summarized their advantages and disadvantages. Furthermore, the main challenge of the GPS signal acquisition has also been analysed. Based on the analysed result, a dual polarization patch antenna with step jumping serial searching approach has been proposed to acquire GPS signal under a massive multipath environment.

The analysed results indicated that the signal strength is one of the main challenges in an urban environment. To overcome the low C/N signal which is col-

lected by the patch antenna in an urban environment, a step jumping acquisition approach is proposed to enhance the sensitivity to weak signals. Simulation and field experiment results indicated that with the step jumping acquisition approach, the acquisition speed is much faster than the conventional serial searching method and benefits from the new acquisition approach. The USRP based GPS receiver is more sensitive than the commercial GPS receiver and more suitable in a challenging environment.

Chapter 4

Robustness Kalman Filter Based GPS L1 Band Carrier Tracking Approaches

4.1 Introduction

The carrier tracking loop in a GPS receiver is considered to be an important process but also the weakest link since signal loss of lock can occur in a variety of situations. Due to the superior noise rejection and lower steady-state error, a third-order PLL (Phase Lock Loop) is recommended in this research project. However, as mentioned before the trade off between the tracking ability and the tracking accuracy can not be neglected for a conventional third-order PLL. On a vehicular communication channel, both greater tracking bandwidth and better tracking accuracy are required in order to successfully lock the carrier signal in a harsh environment.

Aided carrier tracking approaches have been proposed recently, such as the implementation of a Kalman filter (KF) [9], extended Kalman filter (EKF) [10,11,44] or unscented Kalman filter (UKF)-based carrier tracking loops [12], in order to improve the carrier phase tracking ability.

Through a comparative study of KF, EKF and UKF [45], in this chapter we propose two novel and robust carrier tracking methods by dynamically integrating the adaptive Kalman filter, the unscented Kalman filter and the third-order PLL using a decentralized information sharing technique. The proposed approach utilizes the linear system model to reduce the computational cost and due to the equivalence

of the third order PLL and Kalman filter based carrier tracking loop which has been studied in [46–48], the proposed approach dynamically integrates these two tracking loops to obtain an optimal tracking result.

4.2 Carrier Tracking Loop

Once the GPS signal has been successfully acquired, receiver has only roughly estimated the parameters of the frequency and code phase. Thus, the signal tracking play an impotent role in the next step. The main purpose of signal tracking is to refine these value in order to demodulate the navigation message and obtain the measurement of pseudorange, phase and time. To perfectly track and demodulate one specific GPS signal, GPS receiver needs to generate a replica carrier frequency signal and a series of pseudorandom code to synchronize with the incoming IF signal. However, due to the relevant movement between the GPS receiver and the satellite as well as the offset of the receiver and satellites clock, the frequency and phase of the income signal may change frequently and unpredictably.

The aim of the carrier tracking loop is to generate a replica carrier signal and synchronize its frequency with the incoming GPS signal in order to peel the carrier signal through the low pass filter and convert the IF signal back to baseband signal.

As we mentioned before, satellite and its receiver are relevant moving, therefore the GNSS receiver receives the signal frequency f_r is not equal to the satellite emit signal frequency f, the received GNSS signal frequency is $f + f_d$, and this f_d is called Doppler frequency shift. Base on electromagnetic propagation theory, f_d equal:

$$f_d = \frac{\upsilon}{\lambda} cos\beta = \frac{\upsilon}{c} f cos\beta \tag{4.1}$$

where β is the incidence angle between the receiver moving direction and satellite income signal. When receiver moves toward to the satellite incoming direction, β is greater than zero, then the received signal frequency is higher than transmit signal frequency, otherwise the received signal frequency is lower.

To generate the replica carrier signal, GPS receiver does not generate a constant frequency signal, but generate every replica frequency signal by different time through carrier tracking loop. Carrier tracking loop adjusts the frequency and phase of the local signal generator in order to synchronize with the transmit signal. There-

fore, the generated replica signal is dynamic synchronize with the income signal.

There are two types of carrier tracking loop, if the carrier tracking loop can check the phase difference between replica carrier signal and the income signal then adjust the replica signal phase in order to synchronize replica signal and income signal, this approach is called phase lock loop (PLL). If the carrier tracking loop check the frequency difference between replica carrier signal and the income signal and adjust the replica carrier signal frequency, this approach is called frequency lock loop (FLL).

4.2.1 Phase Lock Loop

This research work is more focus on the PLL instead of FLL, since PLL outperform FLL the measurement accuracy [49]. In general, PLL is an electrical control loop which can generate a periodic signal and adjust its output signal phase in order to synchronize with the input signal.

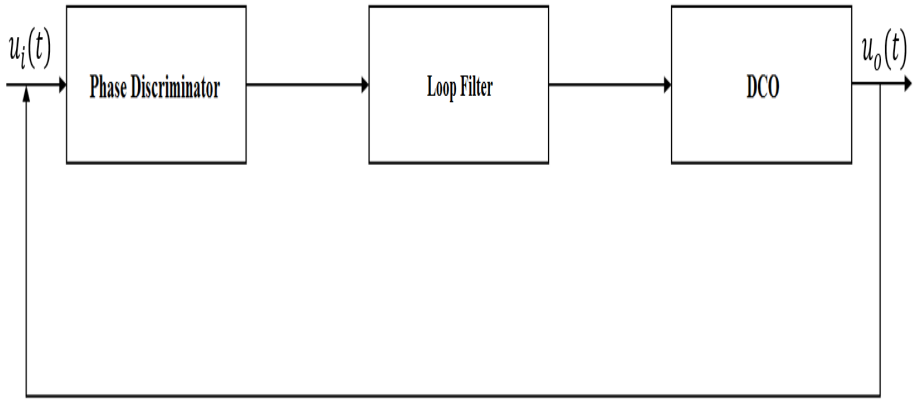

Figure 4.1: Generic PLL Diagram

Figure 4.1 illustrates that a generic PLL consist a phase discriminator, a phase filter and a digital control oscillator (DCO). To the system, a input signal $u_i(t)$ with angular frequency ω_i and phase θ_i and the output signal $u_o(t)$ with angular frequency ω_o and phase θ_o can be expressed in time domain as Eq.(4.2) presents

$$\begin{aligned} u_i(t) &= U_i sin(\omega_i t + \theta_i) \\ u_o(t) &= U_o cos(\omega_o t + \theta_o) \end{aligned} \tag{4.2}$$

where, U_i and U_o are the attitude of the input and output signal. As mentioned before, PLL aims to synchronize $u_o(t)$ and $u_i(t)$ by adjusting the phase of U_i. In

order to detect the phase difference between $u_i(t)$ and $u_o(t)$, phase discriminator can be simply treated as a multiplier. The result $u_d(t)$ is represented as Eq.(4.3)

$$\begin{aligned} u_d(t) &= u_i(t)u_o(t) \\ &= U_iU_o sin(\omega_i t + \theta_i)cos(\omega_o t + \theta_o) \\ &= K_d \left\{ sin\left[(\omega_i + \omega_o)t + \theta_i + \theta_o\right] + sin\left[(\omega_i - \omega_o)t + \theta_i - \theta_o\right] \right\} \end{aligned} \tag{4.3}$$

The gain of the phase discriminator K_d is presented as below,

$$K_d = K_d = \frac{1}{2}U_iU_o \tag{4.4}$$

when PLL is stable angular frequency ω_o is very close to ω_i, the first part of Eq.(4.3) can be expressed as Eq.(4.5)

$$f_H = sin\left[(\omega_i + \omega_o)t + \theta_i + \theta_o\right] \tag{4.5}$$

F_H is a high frequency signal and the second part is a low frequency signal as eq.(4.6)

$$f_L = sin\left[(\omega_i - \omega_o)t + \theta_i - \theta_o\right] \tag{4.6}$$

The loop filter is a low pass filter, since the output signal $u_d(t)$ contains both high and low frequency component and only the low frequency component is desire, the output signal $u_d(t)$ with be filtered by a Loop filter to remove the high frequency component. The the filtered output signal $u_f(t)$ contains only the low frequency part of $u_d(t)$

$$u_f(t) = K_dK_f sin(\theta_e(t)) \tag{4.7}$$

coefficient K_d is the gain of loop filter and the phase error $\theta_e(t)$ equals $\theta_i - \theta_o$, when the loop is stable, $\omega_i - \omega_o$ is close to zero, phase is very close as well, then Eq.(4.7) can be expressed as below .

$$u_f(t) \approx K_dK_f\theta_e(t) \tag{4.8}$$

The output signal $u_f(t)$ will work as a input signal to the digital control oscillator. DCO hereby generates a periodic signal $u_o(t)$, the variance of this periodic signal

relate to $u_f(t)$, the relationship is demonstrated as below

$$\frac{\mathrm{d}\omega_o(t))}{\mathrm{d}t} = K_o u_f(t) \tag{4.9}$$

where K_o is the gain of DCO. $\theta_o(t)$ is the instant angular frequency of DCO. Integration of angular frequency based time is the the phase variance. The initial phase of DCO signal $u_o(t)$

$$\theta_o(t) = \int_0^t \frac{\mathrm{d}\omega_o(t)}{\mathrm{d}t} dt = K_o \int_0^t u_f(t) dt \tag{4.10}$$

4.3 Signal Model and Third order PLL Model

The generic carrier tracking loop has been presented in the previous section. In this section, the complex mode of the received GPS signal will be reviewed, furthermore, the structure of third order PLL is also introduced.

4.3.1 Complex Model of GPS Signal

Unlike Eq.(4.2), the received GPS signal u_i at time t can be formed as (4.11) with navigation and C/A code are added.

$$u_i(t) = AN_{(t)}C/A_{(t-\tau)}cos[(\omega_c + \omega_d)t + \phi_i] + n(t) \tag{4.11}$$

where A is the signal amplitude, N is the navigation bits, $C/A_{(t-\tau)}$ is the coarse acquisition code with delay τ . ω_c is the intermediate frequency of the carrier signal, ω_d is the Doppler frequency shift and $n(t)$ is the noise.

The local oscillator generates replica in-phase (I) and quadrature (Q) carrier signal in prompt time can be represented as (4.12), the I and Q carrier signal is in 90° difference as Eq.(4.12) presents .

$$\begin{aligned} i_{(t)} &= cos[(\omega_c^r)t + \phi^r] \\ q_{(t)} &= sin[(\omega_c^r)t + \phi^r] \end{aligned} \tag{4.12}$$

meanwhile

$$\omega_c^r = \omega_c + \hat{\omega}_d \tag{4.13}$$

where the ω_c^r is the replica carrier radian frequency, $\hat{\omega}_d$ is the replica Doppler frequency shift, ϕ^r is the replica phase in radians. The local replica signal is multiplied by the incoming signal u_i and accumulated with time T in order to generated correlated signal, this processing can be presented as below.

$$\begin{aligned} I &= AN_{(t)}\Lambda(t-\tau)sinc(\Delta\omega_c T)cos(\Delta\phi)+n \\ Q &= AN_{(t)}\Lambda(t-\tau)sinc(\Delta\omega_c T)sin(\Delta\phi)+n \end{aligned} \tag{4.14}$$

where $\Delta\omega_c$ and $\Delta\phi$ are frequency and phase differences between the local oscillator and the incoming signal respectively and $\Lambda(t-\tau)$ is the correlation result. If the carrier tracking loop successfully locks the incoming signal, the difference between the frequency and the phase is approximately equal to zero, then I component contains the navigation message and noise, and the Q component contains the noise only.

Under a dynamic environment, the average phase difference within an integration time is not a constant value, as Eq.(4.15) presented

$$\Delta\bar{\phi} = \Delta\phi_0 + \frac{T}{2}\omega_d + \frac{T^2}{6}\omega_a \tag{4.15}$$

the average phase difference equal the summation of $\Delta\phi_0$, ω_d and ω_a, namely, the carrier phase difference, Doppler frequency shift, and Doppler frequency shift rate respectively.

4.3.2 Model of Third order Phase Lock Loop

As we mentioned, the aim of the PLL is to generate replica carrier signal with same phase and frequency. In the discrete time format, the state model $[\phi, \omega_d, \omega_a]^T$ in conventional third order PLL can be presented as Eq.(4.16)

$$\begin{bmatrix} \hat{\phi} \\ \hat{\omega}_d \\ \hat{\omega}_a \end{bmatrix}_{t+1} = \begin{bmatrix} 1 & T & 0 \\ 0 & 1 & T \\ 0 & 0 & T \end{bmatrix} \begin{bmatrix} \hat{\phi} \\ \hat{\omega}_d \\ \hat{\omega}_a \end{bmatrix}_t + \begin{bmatrix} bw_n \\ aw_n^2 \\ w_n^3 \end{bmatrix} \times \Delta\phi_{t+1} T \tag{4.16}$$

where $\hat{\phi}$ is the phase of the replica carrier signal, and Doppler frequency shift $\hat{\omega}_d$ and shift rate $\hat{\omega}_a$ are corresponding to the estimation of velocity and acceleration.

A Laplace transformed of the loop filter F(s) can be expressed as

$$F(s) = \frac{1}{K}(b_3\omega_n + \frac{1}{s}a_3\omega_n^2 + \frac{1}{s^2}\omega_n^3) \tag{4.17}$$

The z transform is implemented to evaluate the loop filter in discrete form. A bilinear transform is implemented to transform the loop filter from S domain. The transferred loop filter F(z)can be represented as

$$F(z) = \frac{1}{K}(b_3\omega_n + \frac{T_s}{2}\frac{1+z^{-1}}{1-z^{-1}}a_3\omega_n^2 + \frac{T_s^2}{4}(\frac{1+z^{-1}}{1-z^{-1}})^2\omega_n^3) \tag{4.18}$$

Block diagram Figure 4.2 represents the discrete 3rd order phase lock loop, the loop filter which presents in the red dish block is associate with the

As Figure 4.2 presents, b, a and w_n are the fixed parameters of the low pass filter whose values are decided by the tracking bandwidth [50]. As previously mentioned, due to the trade off the performance of the phase lock loop is highly dependent on the noise bandwidth B_n as Eq.(4.19) present.

$$B_n = \frac{(a_3b_3^2 + a_3^2 + b_3)}{4(a_3b_3 - 1)} \tag{4.19}$$

Parameters a_3 and b_3 are decided by the nature frequency in radiance ω_o the relationship is showed as Eq.(4.20)

$$\begin{aligned} a_3\omega_o^2 &= 1.1\omega_o^2 \\ b_3\omega_o &= 2.4\omega_o \end{aligned} \tag{4.20}$$

The small noise bandwidth means less noise can enter to the loop filter, therefore the tracking performance can be accurate. However the smaller noise bandwidth is not efficient for high dynamic signal tracking. Past experience has demonstrated that 18 Hz is the widest noise bandwidth for 3rd order PLL under stable and all dynamics conditions [51]. In general, the performance of the PLL can be measured by the variance of the phase jitter as Eq.(4.21) [50].

$$\sigma_{PLL}^2 = \sigma_{thermal}^2 + \sigma_{\Delta\phi}^2 \tag{4.21}$$

where σ_{PLL} is the total phase jitter which is consisted of the thermal noise $\sigma_{thermal}$

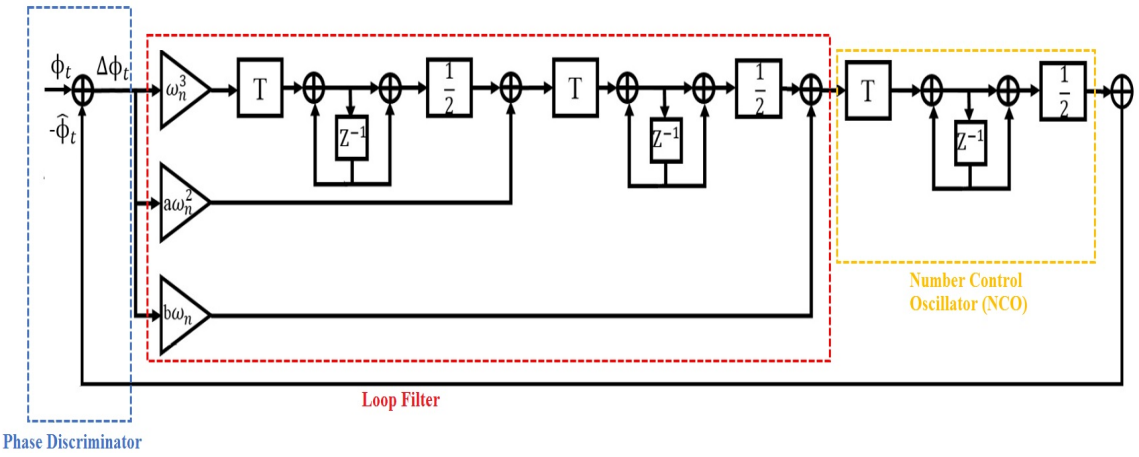

Figure 4.2: Third Order Phase Lock Loop Block Diagram

and the input variance $\sigma_{\Delta\phi}$. The thermal noise jitter can be computed as

$$\sigma_t = \frac{180}{\pi}\sqrt{\frac{B_n}{C/N_o}(1+\frac{1}{2TC/N_o})} \tag{4.22}$$

where B_n is the tracking bandwidth, C/N_o is the carrier to noise ratio and T is the integration time, in our case, we choose 0.001 s. As study [52] presented, the input variance $\sigma_{\Delta\phi}$ can be calculated by the summation of the correlated sources σ_{corr} and the dynamic stress error θ_e as (4.23a) and (4.23b) demonstrate,

$$\sigma_{\Delta\phi} = \sqrt{\sigma_{corr}^2} + \frac{\theta_e}{3} \tag{4.23a}$$

$$\sigma_{corr}^2 = \sigma_{oci}^2 + \theta_A^2 \tag{4.23b}$$

where σ_{oci} is the oscillator phase error which can be calculated by (4.24) [50], and the Allan deviation of the third order PLL σ_A can be obtained as (4.25) in radians [53].

$$\theta_{oci} = \frac{360 f_L}{2\pi}\sqrt{\int_{f_{max}}^{f_{min}} S_{oci}^2 \frac{P(f_m)}{f_m^2} df_m} \tag{4.24}$$

where f_L is equal to 1575.42 MHz which corresponds to the GPS L1 band, S_{oci}^2 is the oscillator vibration sensitivity of $\Delta f/f_L$ per g as a function of f_m, and f_m is the random vibration modulation frequency in Hz. $P(f_m)$ is the power curve of random vibration in g^2/Hz and g is the gravitational acceleration.

$$\theta_A^2 = 2\pi^2 f_{L1}^2 (\frac{\pi^2 h_{-2}}{3\omega_n^3} + \frac{\pi h_{-1}}{3\sqrt{3}\omega_n^2} + \frac{h_0}{6\omega_n}) \tag{4.25}$$

where f_{L1} is the L1 band carrier frequency, and ω_n is the natural frequency. The value of h_0, h_{-1}, h_{-2} are listed in Table (4.1) [54].

Table 4.1: Allan variance parameters for various clocks

Osicallator type	$h_0(Hz)$	$h_1(Hz)$	$h_2(Hz)$
Crystal	2×10^{-19}	7×10^{-21}	2×10^{-20}
Ovenized Crustal	8×10^{-20}	2×10^{-21}	4×10^{-23}
Rubidium	2×10^{-20}	7×10^{-24}	4×10^{-29}

As we discussed above, the error of the correlated source is induced by the local oscillator which has only been minorly effected by the relative movement. The transient response of the third order PLL corresponding with relative movement such as step, acceleration and jerk can be mainly characterized by dynamic stress error.

$$\theta_e = 0.4828 \frac{d^3R/dt^3}{B_n^3} \tag{4.26}$$

where d^3R/dt^3 is the maximum LOS jerk dynamics. As (4.26) presents, the third order PLL is sensitive to jerk and dynamic stress error is decided by tracking bandwidth.

4.3.3 Standard Kalman Filter Algorithm

Kalman filter uses prier information to obtain the optimal estimate value in linear model [55]. Kalman filter has been widely used in navigation and data fusion applications. The dynamic linear state model can be expressed as

$$x_t = Fx_{t-1} + n_{t-1} \tag{4.27}$$

State matrix x_t at time t contains the term of interests, F is the state transition matrix, n_{t-1} is the system noise with 0 mean and covariance matrix is Q, denote as $n \sim (0, Q)$. The measurement model

$$z_t = Hx_t + v_t \tag{4.28}$$

where z_t is the measurement value at time t, H is the transfer matrix, v_t is the measurement noise with 0 mean and the covariance matrix is R, denote a $v \sim (0, R)$.

Two major processes in Kalman filter, which are prediction and update. In

prediction step:

$$\hat{x}_{t|t-1} = F_t \hat{x}_{t-1|t-1} \tag{4.29a}$$

$$\hat{p}_{t|t-1} = F_t P_{t-1|t-1} F_t^T + Q \tag{4.29b}$$

P is the variance associate with true value x_t and the estimate value $x_{t|t-1}$ can be expressed as.

$$P_{t|t-1} = E[(x_t - x_{t|t-1})(x_t - x_{t|t-1})^T] \tag{4.30}$$

In the update step, measurement value will be implement to calibrate the estimate value as Eq.(4.31)

$$\hat{x}_{t|t} = \hat{x}_{t|t-1} + K_t(z_t - H_t \hat{x}_{t|t-1}) \tag{4.31}$$

Then variance matrix P and Kalman gain can be obtained as Eq.(4.32) and Eq.(4.33)

$$P_{t|t} = P_{t|t-1} - K_t H_t P_{t|t-1} \tag{4.32}$$

$$K = P_{t|t-1} H_t^T (H_t P_{t|t-1} H_t^T + R_t)^{-1} \tag{4.33}$$

This section clearly indicates that the performance of the Kalman filter is highly depend on the measurement value integrity and the accuracy of the prier information R and Q.

4.3.4 Kalman Filter based Carrier Tracking Loop

Kalman filter based carrier tracking loops have been widely deployed in GPS carrier tracking loops, as [48] present, the structure of Kalman filter is equivalent to 3rd order PLL. However, the conventional loop filter has a static tracking bandwidth, unlike the conventional third order PLL, the bandwidth of a Kalman filter based carrier tracking loop can be adjusted by the Kalman gain. Therefore, the carrier tracking loop get rid of the limitation of having a fixed bandwidth requirement. The discrete time Kalman filter based carrier tracking loop state model can be represented as Eq.(4.34).

$$\begin{bmatrix} \Delta\hat{\phi} \\ \hat{\omega}_c \\ \hat{\omega}_a \end{bmatrix}_{t+1} = \begin{bmatrix} 1 & T & \frac{T^2}{2} \\ 0 & 1 & T \\ 0 & 0 & 1 \end{bmatrix} \begin{bmatrix} \Delta\hat{\phi} \\ \hat{\omega}_c \\ \hat{\omega}_a \end{bmatrix}_t - \begin{bmatrix} T & \frac{T^2}{2} \\ 0 & 0 \\ 0 & 0 \end{bmatrix} \begin{bmatrix} \omega_{NCO,t} \\ \omega_{a,NCO,t} \end{bmatrix} \omega_{NCO,t} + w_t \tag{4.34}$$

Comparing the state matrix in the KF based carrier tracking loop $[\Delta\hat{\phi}, \hat{\omega}_c, \hat{\omega}_a]^T$ against the state matrix in the 3rd order PLL $[\hat{\phi}, \hat{\omega}_c, \hat{\omega}_a]^T$, the output of the phase difference $\Delta\phi$ is the only different vector. $\omega_{NCO,t}$ is the local oscillator Doppler frequency shift and w_t is the state noise with $w_t \sim (0, Q)$. As (4.15) presented, the measurement model in matrix form can be modelled as

$$\Delta\bar{\phi} = \begin{bmatrix} 1 & \frac{T}{2} & \frac{T^2}{6} \end{bmatrix} \begin{bmatrix} \Delta\phi \\ \omega_c \\ \omega_a \end{bmatrix} - \begin{bmatrix} \frac{T}{2} & \frac{T^2}{6} \end{bmatrix} \begin{bmatrix} \omega_{NCO,t} \\ \omega_{a,NCO,t} \end{bmatrix} + v_t \tag{4.35}$$

where $\Delta\phi$ is the phase difference between the incoming signal and the local oscillator which can be obtained through the phase discriminator. v_t is the measurement noise denoted as $v_t \sim (0, R)$. Comparing Figure (4.2) and Figure (4.4), within the KF based carrier track loop, the Kalman filter works as the loop filter in the third order PLL with time-varying parameters, since the parameters K_1, K_2, K_3 can be adjusted through Kalman gain varying.

According to [56], the equivalent noise bandwidth of Kalman filter can be obtained as Eq.(4.36).

$$B_n = \frac{C_3}{4} + \frac{C_1^2}{4(C_2C_3 - C_2)} \tag{4.36}$$

where

$$\begin{aligned} C_1 &= \frac{2\pi K_3}{T} \\ C_2 &= 2\pi K_3 + \frac{2\pi K_2}{T} \\ C_3 &= \frac{T\pi K_3}{3} + \pi K_2 + \frac{K_1}{T} \end{aligned} \tag{4.37}$$

In [57], the equivalent noise bandwidth of the Kalman filter based phase lock loop can be obtained by Kalman gain. The vectors within the Kalman gain matrix represent the relative uncertainty between the measurement and the estimation value. As Eq.(4.36) shows, the bandwidth of the KF based carrier tracking loop is decided by

the Kalman gain instead of a predefined parameters. As Figure 4.3 presented, the variance of the noise bandwidth and the Kalman gain is positive correlation. To address the variation of the Kalman gain, a square root value of the Kalman gain vector is used to represent the equivalent Kalman gain, As Figure 4.3 present, the noise bandwidth start from a large value in order to tolerant the Doppler frequency shift meanwhile the Kalman gain start from a greater value. After several times of iteration, the Kalman gain retain to a stable and small value and the noise bandwidth narrow down and retain to a small value in order to process fine tracking.

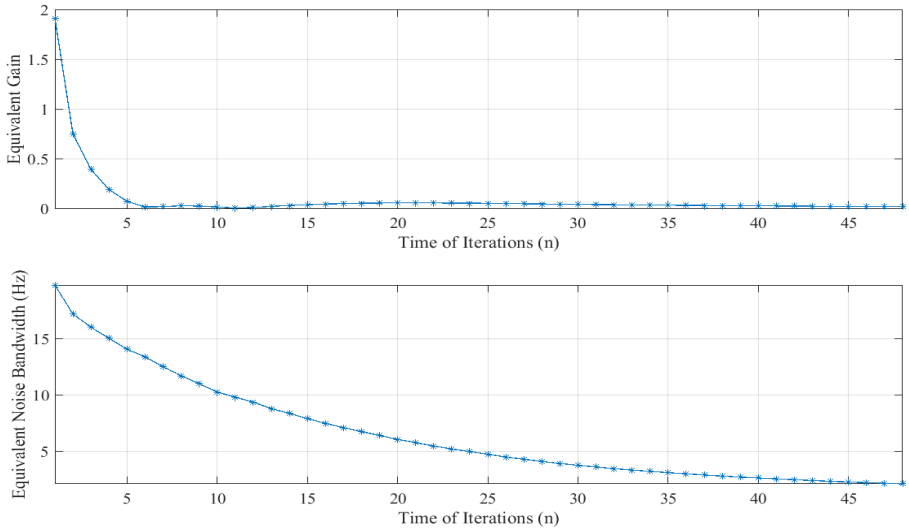

Figure 4.3: Bandwidth adjusted based on Kalman Gain

Kalman filter based carrier tracking loops can self adjust the tracking bandwidth in order to obtain an optimal tracking performance. However the performance of the Kalman filter is not only decided by the tracking bandwidth but also dependent on the prior information accuracy. without a precise prior information, the estimated results from the Kalman filter can be significantly degraded.

4.4 Adaptive Kalman Filter Integrated Third Order PLL Based Carrier Tracking Loop

4.4.1 Adaptive Kalman Filter

In general, the prior information of Kalman filter is defined by rule of thumb. Nevertheless, this prior information is not precise and accurate especially under high dynamic environment. Therefore, the inaccurate prior information could lead to the

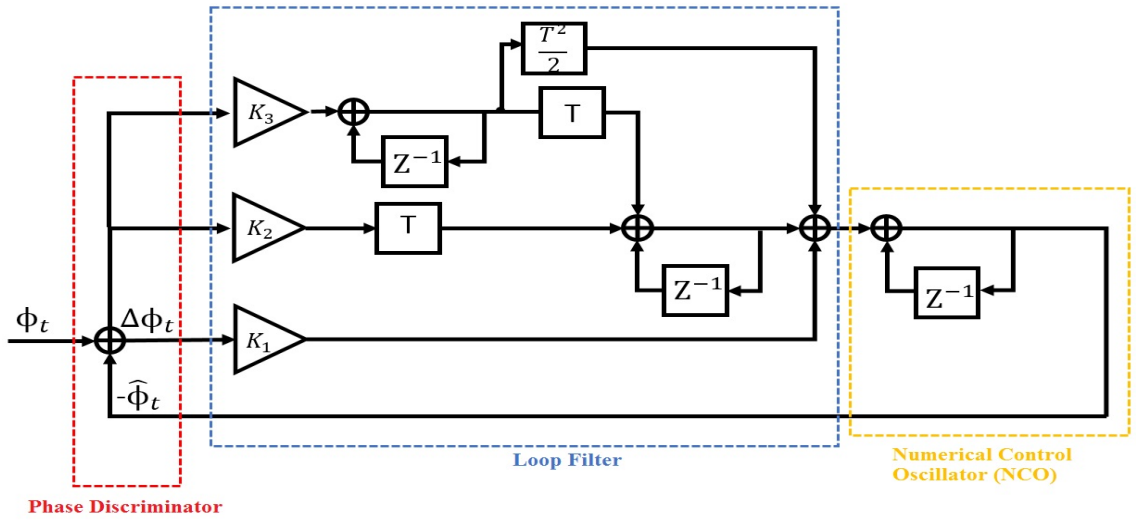

Figure 4.4: Kalman filter Based Carrier Tracking Loop Block Diagram

performance of the Kalman filter being degraded. To overcome this challenge, adaptive Kalman filter has been proposed and implemented in many applications [58] [59].

In this project, we are inspired by the concept of the adaptive Kalman filter, a self estimating the measurement noise covariance Kalman filter has been implement to replace the conventional loop filter. In this project, the system noise covariance Q has been properly defined in [44]. The measurement noise covariance R is estimated through measurement update as Eq.(4.38) present,

$$\hat{x}_{t|t} = \hat{x}_{t|t-1} + K(z - H_t\hat{x}_{t|t-1}) \tag{4.38}$$

where $\hat{x}_{t|t}$ is corresponded to $[\Delta\hat{\phi}, \hat{\omega}_c, \hat{\omega}_a]^T_{t|t}$ which are the posterior estimation of phase difference, carrier frequency and carrier frequency acceleration.

and $\hat{x}_{t|t-1}$ is the prior estimation at time $t-1$, K is Kalman gain, and z is a measurement value which corresponds to $\Delta\bar{\phi}$. The innovation sequence denotes as ξ can be expressed as Eq.(4.39)

$$\begin{aligned} \xi &= z - H_t\hat{x}_{t|t-1} \\ &= H_t x_t + V_t - H_t\hat{x}_{t|t-1} \\ &= H_t(x_t - \hat{x}_{t|t-1}) + V_t \end{aligned} \tag{4.39}$$

A study [60] has proved that the covariance of the innovation sequence ξ is

independent from time and it is approximate to its sample covariance C_t as Eq.(4.40) presents

$$\begin{aligned} C_t &\equiv E\left\{\xi_t \xi_{t-\tau}^T\right\} \\ C_t &= \frac{1}{N}\sum_{t=\tau}^{N} \xi_t \xi_{t-\tau}^T \end{aligned} \tag{4.40}$$

where τ represents τ time back from t, N represents the number of sample points.

The estimated covariance $\hat{C}_t$ can be obtained as Eq.(4.41)

$$\hat{C}_t = (z_t - H_t \hat{x}_{t|t-1})(z_t - H_t \hat{x}_{t|t-1})^T \tag{4.41}$$

Substituting the measurement model into the innovation sequence, ξ can be expressed as Eq.(4.42)

$$\xi = Hx_t + v_t - H\hat{x}_{t|t-1} \tag{4.42}$$

Substituting Eq.(4.42) into Eq,(4.41), the estimated covariance $\hat{C}$ can be expressed as Eq.(4.43)

$$\begin{aligned} \hat{C}_t &= E\left\{(H(x_t - \hat{x}_{t|t-1}) + v_t)(H(x_t - \hat{x}_{t|t-1}) + v_t)^T\right\} \\ &= HE\left\{(x_t - \hat{x}_{t|t-1})(x_t - \hat{x}_{t|t-1})^T\right\} H^T + E\left\{v_t v_t^T\right\} \end{aligned} \tag{4.43}$$

where $\hat{x}_{t|t-1}$ is the predicted value of x_t. The variance of the prediction $\hat{x}_{t|t-1}$ and x_t is given as (4.44)

$$P_{t|t-1} = [E(x_t - \hat{x}_{t|t-1})(x_t - \hat{x}_{t|t-1})^T] \tag{4.44}$$

Substitute Eq.(4.44) in to Eq.(4.43), then Eq.(4.43) can be rewritten as

$$\hat{C}_t = HP_{t|t-1}H^T + R \tag{4.45}$$

Finally, measurement noise covariance R is estimated as Eq.(4.46) recursively.

$$\hat{R} = \frac{1}{N}\sum_{i=k}^{N} \xi_i \xi_{i-k}^T - H_t P_{t|t-1} H_t^T \tag{4.46}$$

In a time-invariant system, the covariance of the innovation sequence $\hat{C}_t$ can be obtained through measurement value updates. The matrix $P_{t|t-1}$ can be defined by

the Kalman filter and the processing covariance Q.

4.4.2 Dynamic Integrated Kalman Filter and Phase Lock Loop

Adaptive Kalman filters can get rid of the prior information inaccuracy issue, however in vehicular environments, acceleration and jerk scenarios occur more often and critically. Simply use Kalman filter to replace loop filter, the performance of the carrier tracking loops is degraded. Therefore, in this paper we proposed a novel carrier tracking approach which dynamically integrates a Kalman filter and third order PLL since third order PLLs are particularly sensitive to jerk. The decentralized information sharing technique is used as the integration scheme.

The decentralized information sharing technique has been widely used in data fusion applications. The value of the information sharing factor can be obtained by the eigenvalues and the eigenvectors from the covariance matrix of each subsystem [61], therefore, the information sharing factor can represents the stability of each subsystem.

Figure 4.5 presents a block diagram of dynamic integrated carrier tracking loop using adaptive Kalman filter and third order PLL. Unlike the conventional Kalman filter based coarse to fine carrier tracking scheme, the proposed approach contains Kalman filter and 3rd order PLL working in parallel, the output of the phase discriminator is treated as the input of both the loop filter and the adaptive Kalman filter, then the filtered results are integrated by an information sharing block and feed back to the numerical control oscillator.

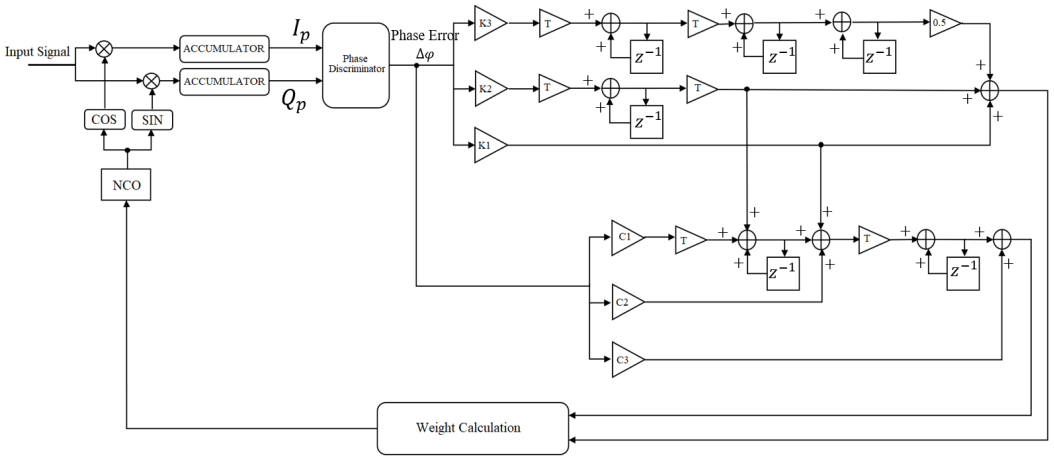

Figure 4.5: Generic Dynamic Integrated Carrier Tracking Loop

Since the sharing weight is decided by the stability (or covariance) of each subsystem the covariance matrix of the i_{th} subsystem P_i can be decomposed as Eq.(4.47)

$$P_i = \ell \Lambda_i \ell^T, \tag{4.47}$$

where $\Lambda_i = diag\{\lambda_{i1}, \lambda_{i2}, ..., \lambda_{in}\}$ and $\lambda_{i1}....\lambda_{in}$ are the eigenvalues of P_i. In order to avoid negative values of λ, ℓ, the eigenvector of P, can be replaced by $P_i^T P_i$ therefore

$$P_i^T P_i = \ell' \Lambda_i' (\ell'^T) \tag{4.48}$$

therefore, $\Lambda_i' = diag\{\lambda_{i1}^2, \lambda_{i2}^2, ..., \lambda_{in}^2\}$.

Finally, the information sharing factor β_i can be expressed as Eq.(4.49)

$$\beta_i \quad = \quad \frac{1}{N-1} \frac{\sum_{j=1}^{N} tr\Lambda_j - tr\lambda_i}{\sum_{j=1}^{N} tr\Lambda_j} \tag{4.49}$$

where N is the total number of subsystems and $j = 1, 2, 3, ..., N$. As Eq.(4.49) presents, a greater value of β_i relates to a more stable estimated subsystem that will take more weight on information sharing and have a larger impact on the entire system.

In our system, the covariance of the Kalman fitler based subsystem P_{KF} can be obtained directly. The covariance of the third order PLL can not be obtained directly, therefore, the covariance of the PLL can be calculated use Eq.(4.21), since the covariance of the PLL equal to the variance of the phase jitter.

$$P_{PLL} = \begin{bmatrix} \sigma_{PLL} & 0 & 0 \\ 0 & \sigma_{PLL} & 0 \\ 0 & 0 & \sigma_{PLL} \end{bmatrix} \tag{4.50}$$

4.5 Adaptive Unscented Kalman filter integrated 3rd Order PLL

Adaptive Kalman filter can self estimate the measurement noise covariance, however the linear model requirement is still a significant limitation of Kalman filter. Therefore, in this section, we proposed a adaptive unscented Kalman filter based carrier tracking loop to get rid of the linear model restriction.

4.5.1 Unscented Transform

It is an intuitive that to approximate a function's distribution is easier than its arbitrary nonlinear function [62]. The one of the most popular approach to approximate a distribution is called unscented transform (UT).The UT uses the calculated mean and variance of a random variable to propagate through a nonlinear function [63]. The UT processing is demonstrated as Figure 4.6, sigma points which are selected via the mean and variance capture the high order information of the distribution as expressed in the solid circle of Figure 4.6. Through the nonlinear propagation, the accuracy of the approximation can achieve up to the 2^{nd} order (Taylor series expansion) of nonlinearity as expressed in the dash circle [64] [65].

The UT process start from calculating the mean and variance of the random variable. A random variable x with L dimensions has mean and covariance represent as $\bar{x}$ and P_x presented as (4.51).

$$\begin{aligned} \bar{x} &= E[x] \\ P_x &= E[(x-\bar{x}_0)(x-\bar{x}_0)^T] \end{aligned} \tag{4.51}$$

Meanwhile a matrix X with L dimensions needs $2L+1$ of sigma vectors X_i to form its distribution, which are presented as Eq.(4.52):

$$\begin{aligned} X_i &= \bar{x}; \qquad for\ i=0 \\ X_i &= \bar{x} + (\sqrt{(L+\lambda)P_x})_i; \qquad for\ i=1,...,L \\ X_i &= \bar{x} + (\sqrt{(L+\lambda)P_x})_i; \qquad for\ i=L+1,...,2L \end{aligned} \tag{4.52}$$

where λ is a scaling parameter and can be obtained using Eq.(4.53)

$$\lambda = \alpha^2(L+\kappa) - L \tag{4.53}$$

where α decides the spread of the sigma points around $\bar{x}$, and α is usually a small positive value like 0.001 and κ is another scaling parameter that is normally set to zero [66]. After propagating the sigma vectors X_i through the nonlinear function $f(x)$ we obtain the results as y_i

$$y_i = f(X_i); \qquad i=0,...,2L. \tag{4.54}$$

The mean and covariance of the transformed output y_i can be obtained by a weighted mean and covariance as Eq.(4.55) [64]:

$$\begin{aligned} \bar{y} &= \sum_{i=0}^{2L} W_i^m y_i \\ P_y &= \sum_{i=0}^{2L} W_i^c [(y_i - \bar{y})(y_i - \bar{y})^T] \end{aligned} \tag{4.55}$$

Where W_i represents the weights of each transformed vector. And their values can be calculated using Eq.(4.56) [64]

$$\begin{aligned} W_i^m &= \lambda/(L+\lambda) \qquad i = 0 \\ W_i^c &= \lambda/(L+\lambda) + (1+\alpha^2+\beta) \qquad i = 0 \\ W_i^m &= W_i^c = 1/2(L+\lambda) \qquad i = 1, ...2L \end{aligned} \tag{4.56}$$

where β is equal to 2 [64] since we consider our model to have a Gaussian distribution as studied in [10].

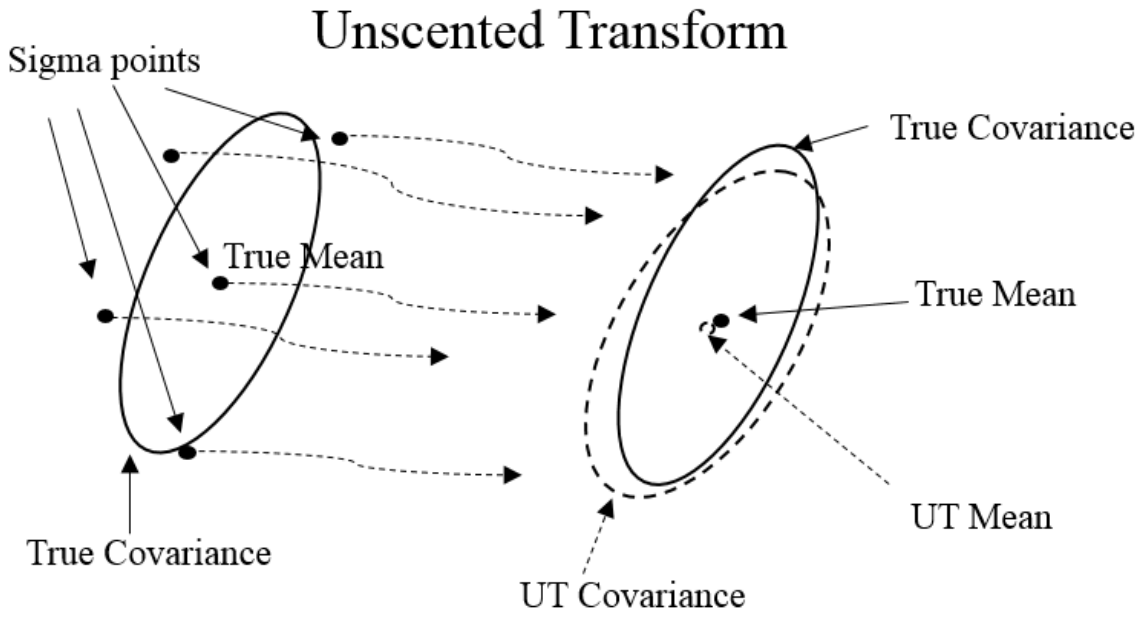

Figure 4.6: Procedure of Unscented Transform

4.5.2 Adaptive Unscented Kalman Filter and Implementation

The unscented Kalman filter is based on an expansion of the unscented transform. In the unscented Kalman filter based carrier tracking loop, the unscented Kalman filter is used to track the phase of the incoming carrier signal directly [12]. The phase of the incoming signal which is effected by Doppler shift can be represented as Eq.(4.57),

$$\Phi = \phi_c + \Delta t\omega_d + \frac{\Delta t^2}{2}\omega_a + \frac{\Delta t^3}{6}\omega_j \tag{4.57}$$

The state model of UKF based carrier tracking loop is formed as Eq.(4.57), in the matrix form Eq.(4.57) can be represented as Eq.(4.58a,4.58b).

$$\vec{x}_t = A\vec{x}_{t-1} + \Delta t\omega_{nco} + noise \tag{4.58a}$$

$$\begin{bmatrix}\phi_c\\ \omega_d\\ \omega_a\\ \omega_j\end{bmatrix}_t = \begin{bmatrix}1 & \Delta t & \frac{\Delta t^2}{2} & \frac{\Delta t^3}{6}\\ 0 & 1 & \Delta t & \frac{\Delta t^2}{2}\\ 0 & 0 & 1 & \Delta t\\ 0 & 0 & 0 & 1\end{bmatrix}\begin{bmatrix}\phi_c\\ \omega_d\\ \omega_a\\ \omega_j\end{bmatrix}_{t-1} + \Delta t\omega_{NCO} + diag(W_t) \tag{4.58b}$$

$$A = \begin{bmatrix}1 & \Delta t & \frac{\Delta t^2}{2} & \frac{\Delta t^3}{6}\\ 0 & 1 & \Delta t & \frac{\Delta t^2}{2}\\ 0 & 0 & 1 & \Delta t\\ 0 & 0 & 0 & 1\end{bmatrix} \tag{4.58c}$$

The state matrix $\vec{x}$ has four vectors which are $\vec{x} = [\phi_c \quad \omega_d \quad \omega_a \quad \omega_j]^T$, ϕ_e is the carrier phase, ω_d represents the Doppler frequency, ω_a is the first order of the Doppler frequency change rate and ω_j is the second order of the Doppler frequency change rate. A is the state transition matrix, Δt is the time interval, ω_{NCO} is the phase shift of the numerical control oscillator, W_t represents the processing noise with zero mean and its covariance is denoted as Q, $W_t \sim (0, Q)$. The incoming GPS signal are represents in I and Q form, after passing a low pass filter the high frequency components have been removed, the low frequency component are presented as

Eq.(4.59):

$$\begin{aligned} I_{p,t} &= AD(t)[\cos((\phi_c + \Delta t\omega_d + \frac{\Delta t^2}{2}\omega_a + \frac{\Delta t^3}{6}\omega_j)] \\ Q_{p,t} &= AD(t)[\sin((\phi_c + \Delta t\omega_d + \frac{\Delta t^2}{2}\omega_a + \frac{\Delta t^3}{6}\omega_j)] \end{aligned} \tag{4.59}$$

Directly using I_p and Q_p as the measurement matrix vector can cause polarity reversal, thus in order to avoid polarity reversal of the navigation data, I_p and Q_p need to treated as Eq.(4.60)

$$\begin{aligned} I_{p,t}^2 - Q_{p,t}^2 &= A^2 D(t)^2 \cos(2\Phi) \\ 2I_{p,t}Q_{p,t} &= A^2 D(t)^2 \sin(2\Phi) \end{aligned} \tag{4.60}$$

where Φ is the phase of carrier signal. The normalized amplitude can be obtained through Eq.(4.61)

$$A_t^2 \; D_t^2 = \sum_{i=t-n}^{t} (I_{p,t}^2 + Q_{p,t}^2)/n \tag{4.61}$$

where n is the coherent integration time. Finally, the measurement matrix z can be represented as

$$\begin{aligned} z = \begin{bmatrix} I_z \\ Q_z \end{bmatrix} &= \begin{bmatrix} I_{p,t}^2 - Q_{p,t}^2 \\ 2I_{p,t} \times Qp,t \end{bmatrix} \qquad (\sum_{i=t-n}^{t} (I_{p,t}^2 + Q_{p,t}^2)/n)^{-1} \\ &= \begin{bmatrix} \cos(2\Phi) \\ \sin(2\Phi) \end{bmatrix} + diag(V_t) \end{aligned} \tag{4.62}$$

where the measurement noise, $V_t \sim (0, R)$, has zero mean and covariance R.

Starting from the estimated mean value of the state matrix $E(\hat{x}_{t-1})$ and the variance matrix P_{t-1} at time $t-1$. Nine sigma points ($i = 1, ..., 9$) are selected using Eq.(4.52) since our state matrix $x = [\phi_c \quad \omega_d \quad \omega_a \quad \omega_j]^T$ contains 4 vectors. These 9 points are mathematically expressed as Eq.(4.63.1) and then the covariance matrix $P_{t-1|t-1}$ is updated as in Eq.(4.63.2).

Substituting the output $\hat{x}_{t|t-1}^i$ into the measurement model equation $h(\cdot)$ as in Eq.(4.64a), $h(\cdot)$ is a nonlinear trigonometric function presented in Eq.(4.62). The weighted mean output value with respect to state and measurement models can be calculated as (4.63.3) and (4.64b). These values are used to obtain the covariance matrix $P_{\bar{y}\bar{y}}$ and $P_{\bar{x}\bar{y}}$, which are the covariance of the measurement function approx-

imation and the covariance of the state and measurement function approximation. Prediction stage and measurement stage are presented as Eq.(4.63) and Eq.(4.64).

Prediction stage:

$$\hat{x}^i_{t|t-1} = A\hat{x}^i_{t-1|t-1} + \Delta t\omega_{nco} \tag{4.63.1}$$

$$P_{t|t-1} = AP_{t-1|t-1}A + Q \tag{4.63.2}$$

$$\bar{x}_{t|t-1} = \sum_{i=0}^{2L} W_i^m \hat{x}^i_{t|t-1} \tag{4.63.3}$$

Measurement stage:

$$\gamma_{t|t-1} = h(\hat{x}^i_{t|t-1}) \tag{4.64a}$$

$$\bar{y}_{t|t-1} = \sum_{i=0}^{2L} W_i^m \gamma_{t|t-1} \tag{4.64b}$$

$$P_{\bar{y}\bar{y}} = \sum_{i=0}^{2L} W_i^c [(\gamma_{i,t|t-1} - \bar{y}_{t|t-1})(\gamma_{i,t|t-1} - \bar{y}_{t|t-1})^T] + R \tag{4.64c}$$

$$P_{\bar{x}\bar{y}} = \sum_{i=0}^{2L} W_i^c [(\hat{x}_{i,t|t-1} - \bar{x}_{t|t-1})(\gamma_{i,t|t-1} - \bar{y}_{t|t-1})^T] \tag{4.64d}$$

$$K_t = P_{\bar{x}\bar{y}} P^{-1}_{\bar{y}\bar{y}} \tag{4.64e}$$

$$P_t = P_{t|t-1} - K_t P_{\bar{y}\bar{y}} K_t^T \tag{4.64f}$$

$$\bar{x}_{t|t} = \bar{x}_{t|t-1} + K_t(y_t - \bar{y}_{t|t-1}) \tag{4.64g}$$

where $\bar{x}_{t|t}$ is the state matrix which contains optimal mean vectors of the carrier signal parameters at time t and these mean vectors can be used to select sigma points for $t+1$ time estimation.

Like the Kalman filter, the unscented Kalman filter will also suffer performance degradation if the prior information is mismatched with the real system. In our system, due to the linear processing model, the processing noise covariance Q could be recursively updated using the covariance matching method [67].

In the measurement update process, the covariance of the innovation sequence ξ_t, has proved to be independent of time and is approximated from its sampled

covariance [60], as given by Eq.(4.65a-c).

$$\xi_t = y_t - \bar{y}_{t|t-1} \tag{4.65a}$$

$$C_t \equiv Cov\ (\xi_t) \tag{4.65b}$$

$$C_t = \frac{1}{N} \sum_{t=k}^{N} \xi_t \xi_{t-k}^T, \tag{4.65c}$$

where k represents a delay of length k from t and N is the number of samples. In the state processing model, the processing noise w_t can be represented as Eq.(4.66)

$$w_{t-1} = x_t - A(x_{t-1}). \tag{4.66}$$

The Kalman filter estimation equation can be written as Eq.(4.67)

$$x_t - x_{t-1} = K_t(y_t - \bar{y}_{t|t-1}) \tag{4.67}$$

In our application, x_t and x_{t-1} are represented by their mean values, $\bar{x}_t$ and $\bar{x}_{t-1}$. Therefore, combining Eq.(4.66) and Eq.(4.67)

$$w_{t-1} = \bar{x}_t - \bar{x}_{t-1} = K_t(y_t - \bar{y}_{t|t-1}). \tag{4.68}$$

To estimate the innovation sequence covariance, the processing noise covariance can be obtained as Eq.(4.69)

$$Q_{t-1} = K_t C_t K_t^T. \tag{4.69}$$

In a time-invariant system with a high sampling frequency, variation within successive epoch is very small, therefore the successive variation of the Kalman gain element is small enough, thus $K_t \approx K_{t-1}$

$$Q_{t-1} = K_{t-1} C_t K_{t-1}^T. \tag{4.70}$$

4.5.3 Dynamic Integration structure

Benefiting from the strong capability of the nonlinear model's tolerance, the unscented Kalman filter could replace the phase discriminator and loop filter to directly track the carrier signal phase. However, this type of carrier tracking loop

works as a quasi open loop, an open loop could have a higher noise level compared to a closed loop. Therefore, a simple UKF based carrier tracking loop has a strong tracking ability but less sensitive to low C/N_o signal. To mitigate the noise level in an AUKF-based carrier tracking loop, we implement a conventional third-order phase lock loop and join the AUKF in parallel.

In our approach, the adaptive unscented Kalman filter and third-order PLL are considered as two independent subsystems. The covariance matrix P_{AUKF} can be obtained directly from AUKF processing and a standard Kalman filter needs to be implemented to estimate the processing covariance P_{PLL} of the third-order PLL. As mentioned in the previous section, covariace matrix P represents the stability of the system.

The integrated carrier tracking scheme in Figure.4.7 demonstrated two subsystems. The adaptive unscented Kalman filter algorithm that recursively estimates the processing noise covariance can track the incoming carrier signal in parallel with a third-order PLL and integrate the results using the information sharing factors. As

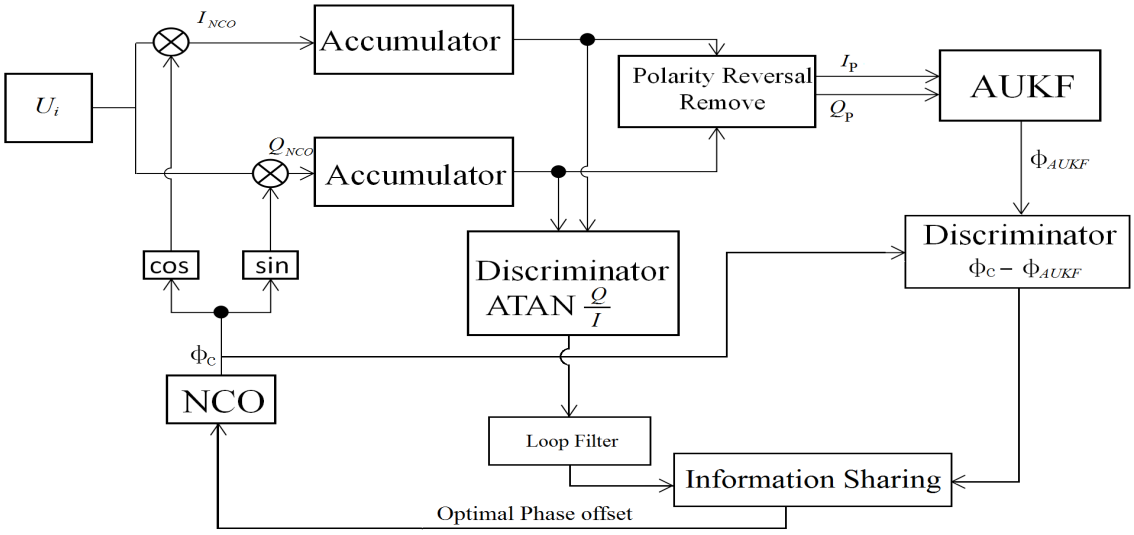

Figure 4.7: Procedure Diagram of the Proposed Approach

aforementioned, in order to avoid polarity reversal, the block named Polarity Reversal Remove performs the process as Eq(4.60), then the processed I and Q component are worked as the measurement input to the adaptive Unscented Kalman filter.

4.6 Experiment Setup and Results Analysis

In order to test the proposed carrier tracking approach, a field experiment is conducted to compare and analyze the tracking performance from the adaptive Kalman filter based Carrier tracking Loop and the proposed dynamic integration tracking scheme. The GPS raw data is collected from the real environment and post processed by MATLAB 2016b.

4.6.1 Robust GPS Carrier Tracking Loop using Hybrid Adaptive Kalman filter

4.6.1.1 Experiment Set up and Location

The experiment is setup as Figure 4.8 and conduct at the Devonshire Building car park, Newcastle University, UK as shown in Figure 4.9. This location is surrounded by buildings which can generate multipath effect and the open parking area is convenient for maneuvering a trolley. The experiment is undertaken for 3 consecutive days. A USRP (2^{nd} component in the figure) and a Leica AX1203+ GNSS antenna (1^{st} component in the figure) works as a front-end, the received center frequency is set to be 1575.42 MHz corresponding to the L1 band. The RF signal is down-converted to a baseband signal by the USRP and is then sampled at 5MHz. The recorded data type is a 16 bit integer, and this is the only option available from the USRP. Because of the large data type, 16-bits data is converted to be 8 bits. The baseband signal is then up-converted to an IF band at 2.5 MHz without any loss of signal characteristic and up-sampled at a rate of 10 MHz. An external precise atomic clock, the Symmetricom CSAC SA.45s (3^{rd} component in the figure), is used to provide a 10 MHz time source since the USRP uses a generic (TXCO) oscillator [68] and is not suitable for a highly dynamic environment. In order to simulate a non-stationary environment, all devices are powered by two 12V batteries (7^{th} component in figure) and place on the trolley. The tracking bandwidth is set to be 18 Hz which is the threshold value to retain a stable third order PLL. Under such a tracking bandwidth, the conventional 3rd order PLL contains a high level of noise, this will be further analysed in Figure 4.10 in the next section.

Figure 4.8: Experiment Setup

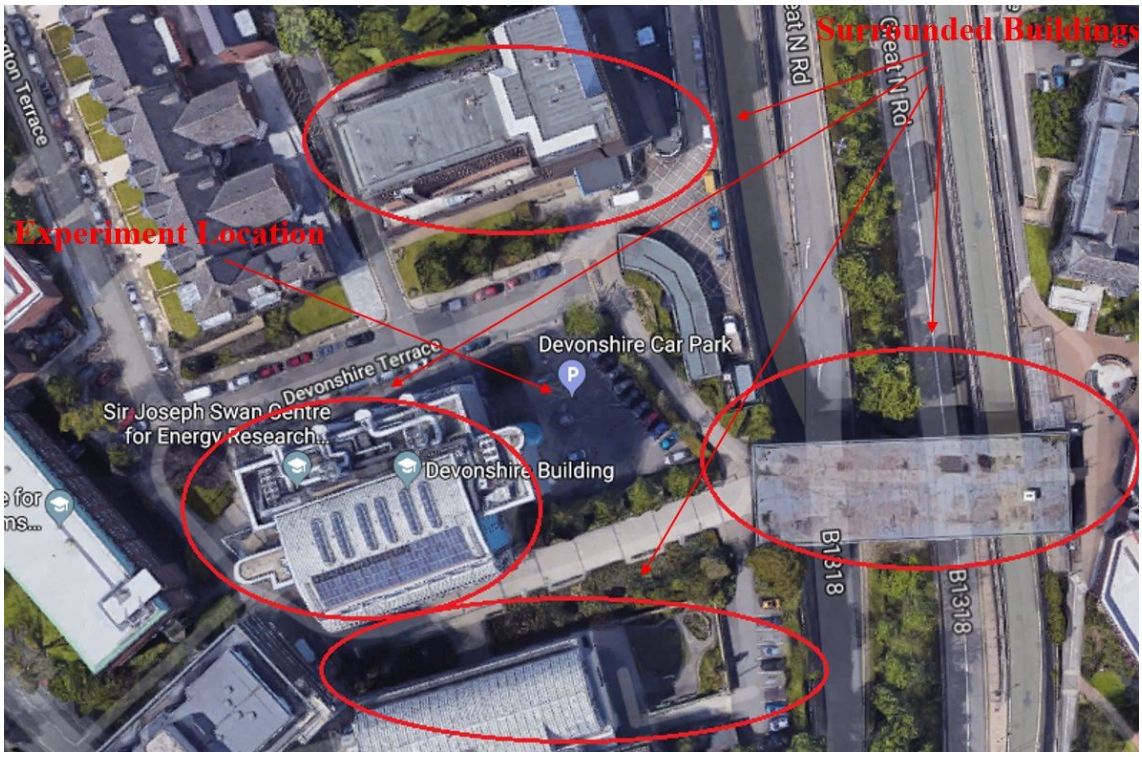

Figure 4.9: Experiment Location

4.6.1.2 Results and Analysis

Starting from a modified serial searching acquisition approach [69], 18 s of GPS raw data has been processed in order to allow a sufficient amount of data to be compared. As mentioned in the previous section, in a conventional 3rd order PLL the noise level is very high. As Figure 4.10 presents the C/N_o in conventional 3rd order PLL is only around 10 dB.

C/N_o is an important parameter since it can characterize the GPS receiver performance. The higher C/N_o indicates a better phase estimation and location determination. The C/N_o estimation in this experiment uses the Narrowband-Wideband power ratio method [70]. Considering the AKF based carrier tracking loop and the dynamic integrated tracking approach, the initial C/N_o is all around 23 dB, due to the reduced signal strength the C/N_o is reducing for the two approaches, however the decline rate of the proposed approach is slower compared to the AKF based approach. After 4 s, the C/N_o from the proposed approach start to increase and achieve approximately 25 dB which is around 10 dB higher than AKF based approach and 15 dB higher than conventional 3rd order PLL. Furthermore, this result proves that the proposed dynamic integrated tracking approach can meet the vehicular communication requirement, since vehicular communication is often faced with the GPS signal strength degradation challenge.

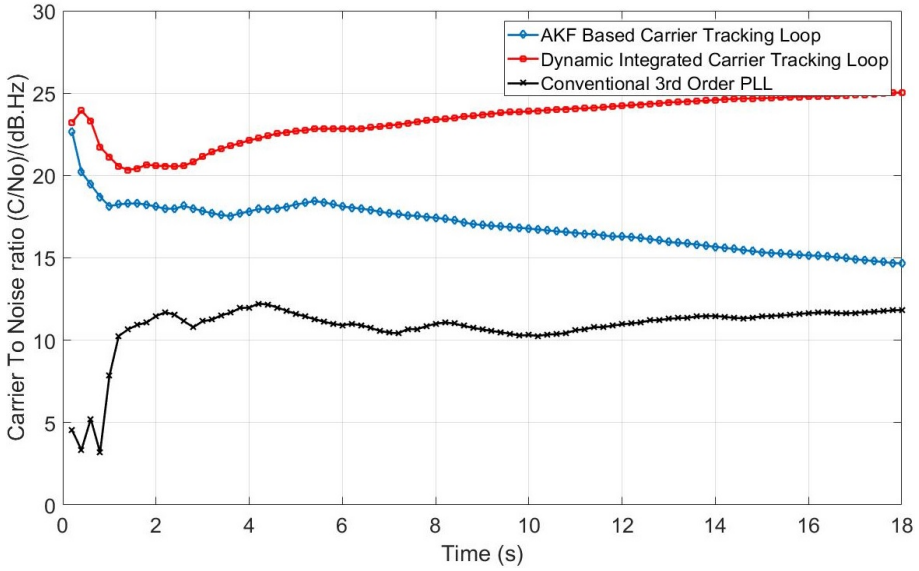

Figure 4.10: Carrier to Noise Ratio

GPS uses a binary phase shift keying (BPSK) modulation scheme, the optimal demodulation results will present a constant value in I and 0 in Q. As Figure 4.11

presents, neither AKF based carrier tracking loop nor conventional 3rd order PLL can filter the noise effectively, since Q component still contains a constant value. In contrast, the proposed method can significantly reduce the noise level, and make the demodulation possible.

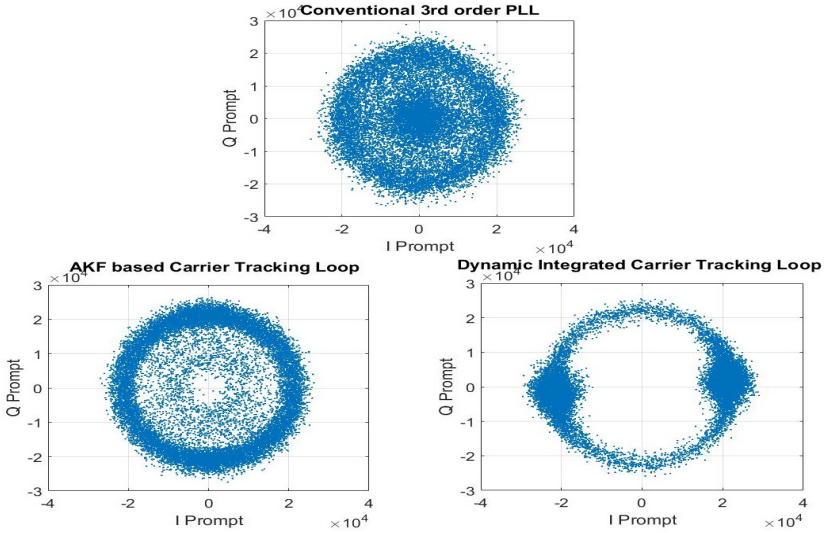

Figure 4.11: Discrete Scatter Comparison

Furthermore, the superior noise rejection performance can also be proved in the output of the phase discriminator as Figure 4.12 illustrated. As Figure 4.12 shows, after a few seconds, the output of the phase discriminator from the proposed method has been significantly reduced compared to the other two approaches. The output of the phase discriminator is approximate to be zero. Meanwhile, as Figure 4.13 presents, the phase variance in the proposed approach is stable and retain to a very small value.This proves that the proposed approach is more stable and robust. All the superior performances above are due to the novel dynamic integrated structure, the proposed carrier tracking approach can self adjust the weight of the AKF and third order PLL due to their variance. The more stable subsystem carries more weight within the entire tracking system.

The phase lock indicator presented in Figure 4.14 indicates the locking status of the carrier tracking loop. The optimal value is 1 or close to 1. This indicator results are mainly compared with the AKF based carrier tracking approach since conventional 3rd order PLL has a less significant result. The comparison result shows that in the first few seconds the two carrier tracking loops struggle to successfully lock the incoming signal, however after 2s the dynamic integrated carrier tracking loop starts to recover from the fluctuation, and retains the success eventually. The

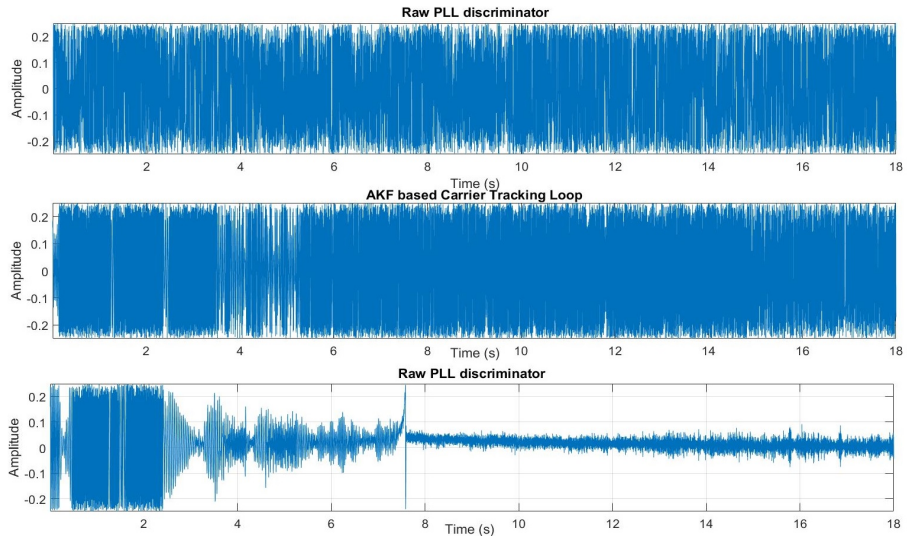

Figure 4.12: Phase Difference Comparison

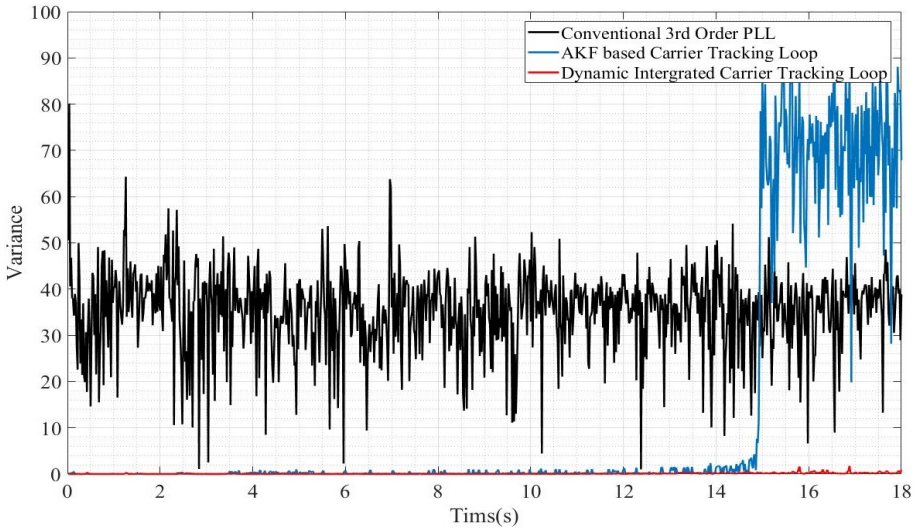

Figure 4.13: Phase variance

lock indicator has a strong relationship with the navigation message decoding.

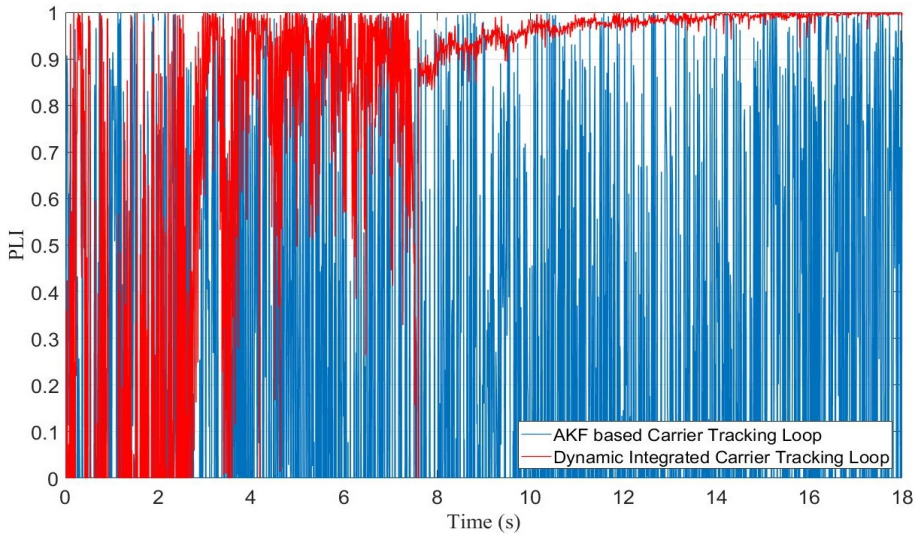

Figure 4.14: Phase Lock Indicator Comparison

The decoded navigation message is demonstrated in Figure4.15, it shows that the proposed approach can successfully demodulate the navigation message, in contrast the 3rd order PLL and the AKF based carrier tracking loop fails to demodulate the navigation message due to the high noise level.

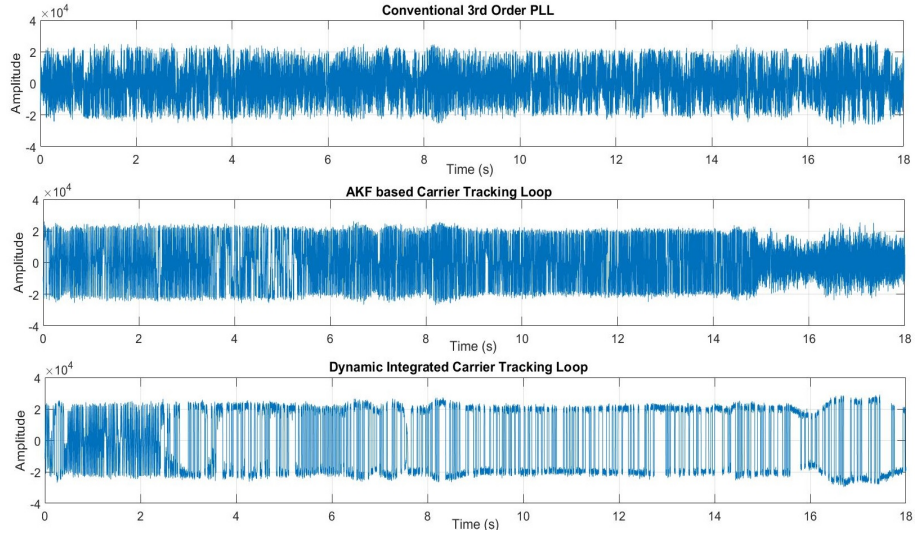

Figure 4.15: Navigation Bits Comparison

4.6.2 Robust GPS Carrier Tracking Model using Unscented Kalman Filter

In this tracking approach, we process 5s GPS raw data which is efficient and sufficient to test the performance of the proposed approach. The tracking bandwidth is

set to 12Hz, which is a relatively large bandwidth for a third-order PLL. Figure4.16 presents the phase lock indicator(PLI) comparison results between AKF based carrier tracking loop and the proposed approach. As can be seen in Figure4.16, both tracking approaches can lock the carrier signal successfully in general, but it can also be seen that the proposed method outperforms the AKF-based approach overall.

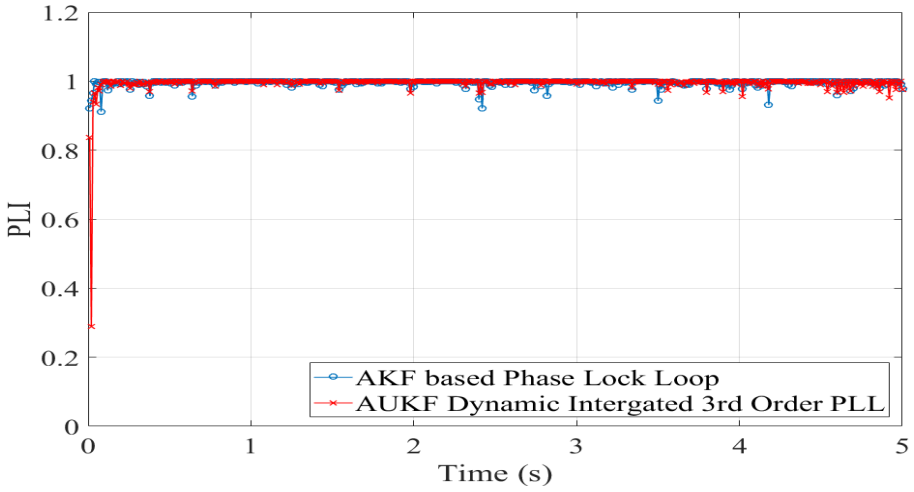

Figure 4.16: Phase Lock Indicator Comparison at Bandwidth 12 Hz

Due to the binary phase shift keying (BPSK) modulation used in GPS signals, the demodulated constellation map of the I and Q components are presented as Figure 4.17.

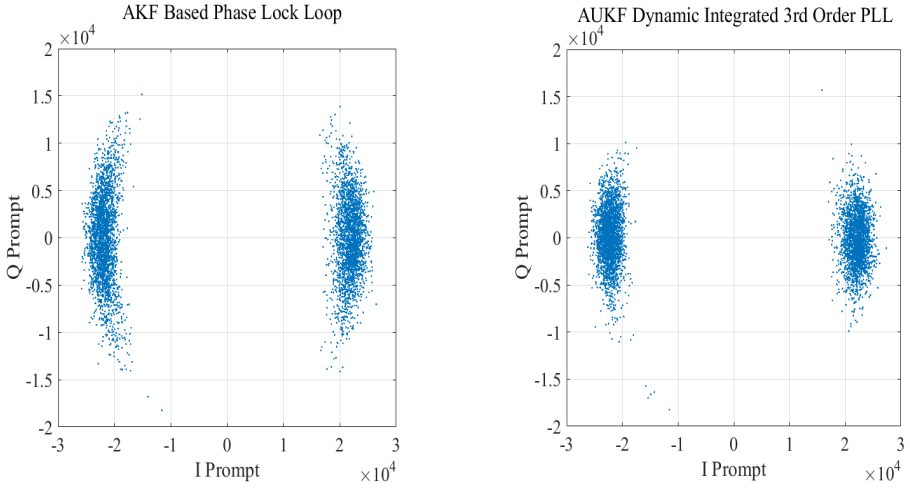

Figure 4.17: Processed I and Q at Bandwidth 12 Hz

As mentioned before, an ideal constellation map of BPSK, all the points have a constant value in the I component and 0 value in the Q component. In Figure4.17, all approaches can successfully demodulate both the I and Q components, however the Q component in the proposed method has a smaller variation compared to the

AKF based PLL, which means the noise level from the proposed method is lower than the AKF based PLL. This can also be proved in Figure4.18, where the output of the phase discriminator from the proposed approach is smaller than the AKF-based PLL. The phase variances from these two approaches are presented as Figure4.19. The phase variance from the AKF-based PLL approach is on average 1.5 however the phase variance of the proposed AUKF dynamically integrated 3_{rd} order PLL method has an average less than 1.

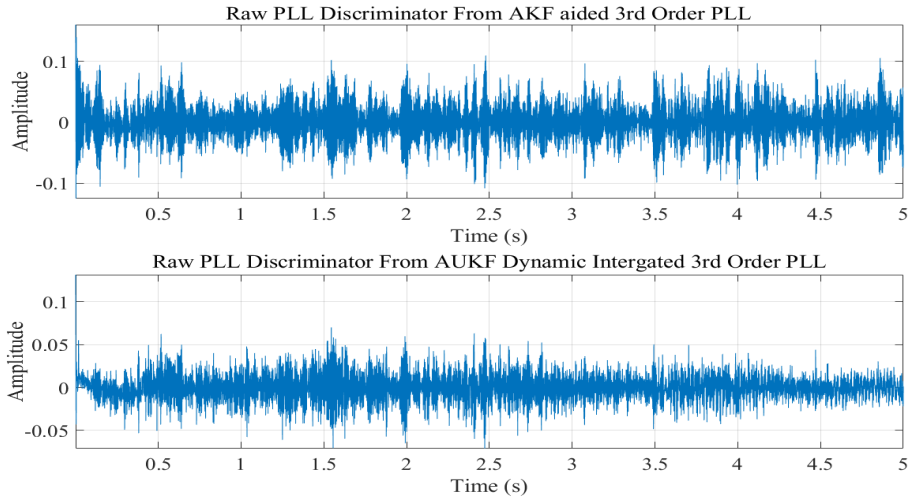

Figure 4.18: Phase Difference at Bandwidth 12 Hz

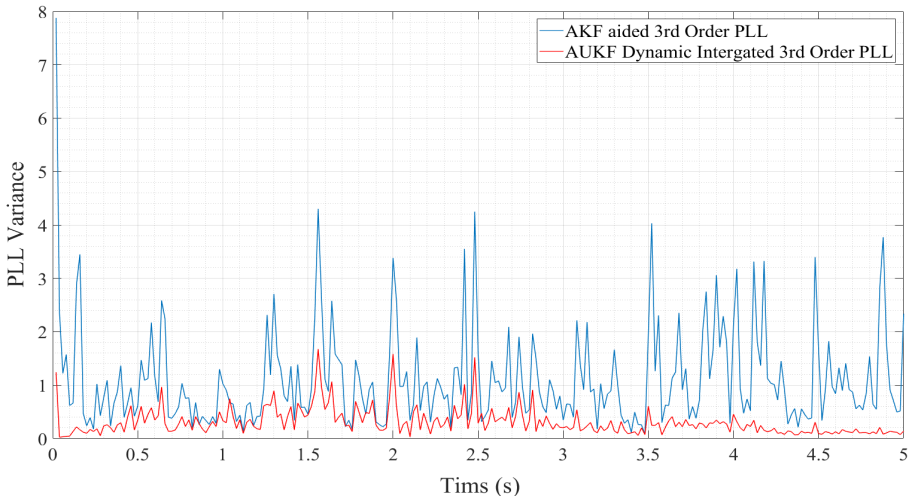

Figure 4.19: Phase variance Comparison at Bandwidth 12 Hz

As aforementioned, the sharing factor which is obtained form the convince matrix and it decides the sharing weight, the adaptive unscented Kalman filter and the third order PLL. The variation of two sharing factors are presented in Figure4.20, at the very beginning the sharing factor from the third order PLL β_1 is very high and the third order PLL dominates the entire loop because the adaptive unscented Kalman

filter needs to recursively estimate the covariance and reach a steady state. Then the sharing factor of the AUKF-based subsystem β_2 increases dramatically and starts to dominate the carrier tracking loop. Once the noise level reduces to a relevant level, β_2 tends to decrease and the tracking loop will be handed over to the third-order PLL.

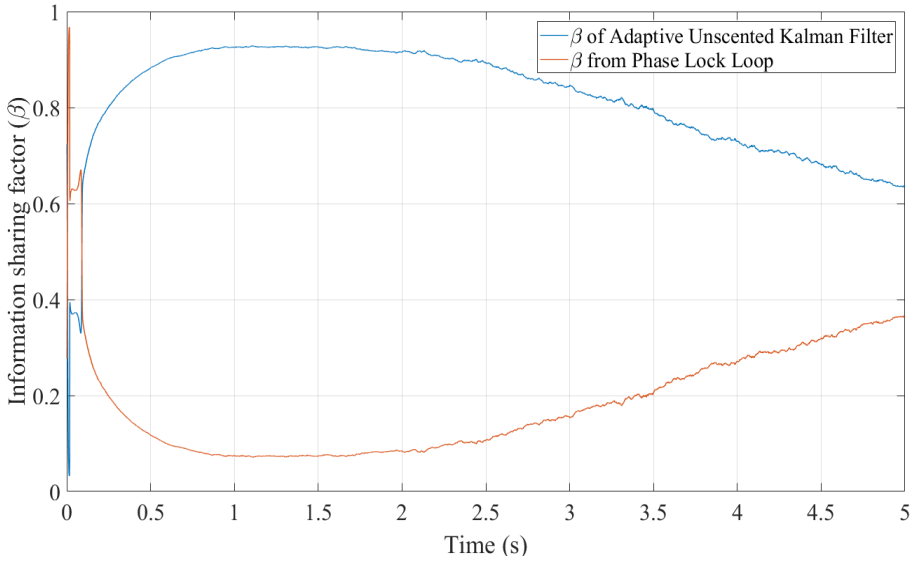

Figure 4.20: Decentralized Information Sharing Factors (β) at Bandwidth 12 Hz

Carrier-to-noise ratio (C/N_o) is an important parameter for describing the GPS receiver performance, where a higher C/N_o indicates a better phase estimation and location determination. The C/N_o estimation in this experiment uses the Narrowband-Wideband power ratio method [70]. The Comparison of C/N_o within these two methods are presents as Figure 4.21, the proposed method shows an improvement of 1.5 dB at the beginning, and 1 dB on average. The proposed approach does not show a significant improvement due of the relatively low tracking bandwidth.

The tracking bandwidth was increased to 13 Hz in order to increase the tracking range and improve the dynamic tracking capability. As Figure 4.22 presented, the AKF-based PLL has difficulty in locking the incoming signal phase and eventually loses the lock, yet the proposed adaptive unscented Kalman filter dynamically integrated third-order PLL can still retain the lock. As Figure 4.23 demonstrates, the constellation map for the AKF-based PLL struggles to distinguish the I and Q components because of the high noise level, however, the proposed tracking approach can still distinguish I and Q components clearly.

The output of the phase discriminator and phase variance are presented in Figure

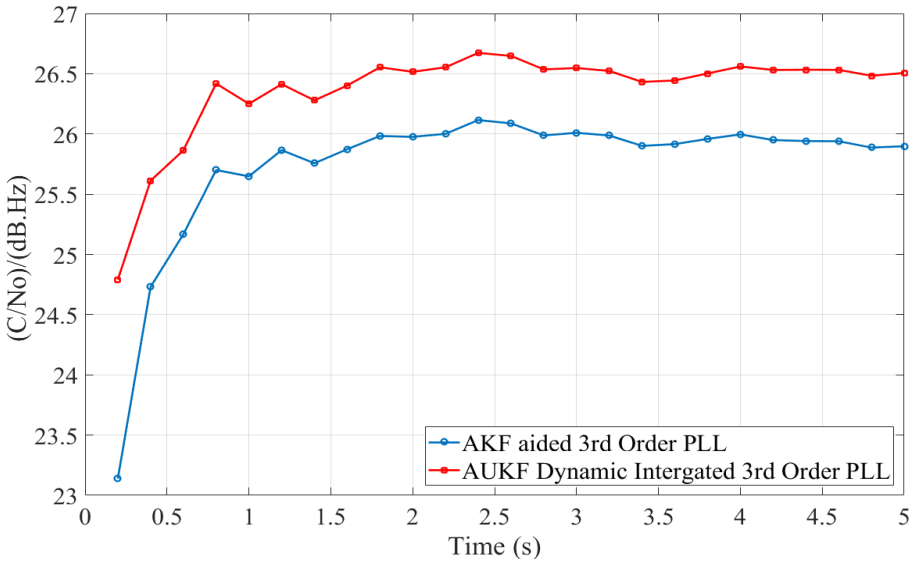

Figure 4.21: Carrier to Noise Ratio Comparison at Bandwidth 12 Hz

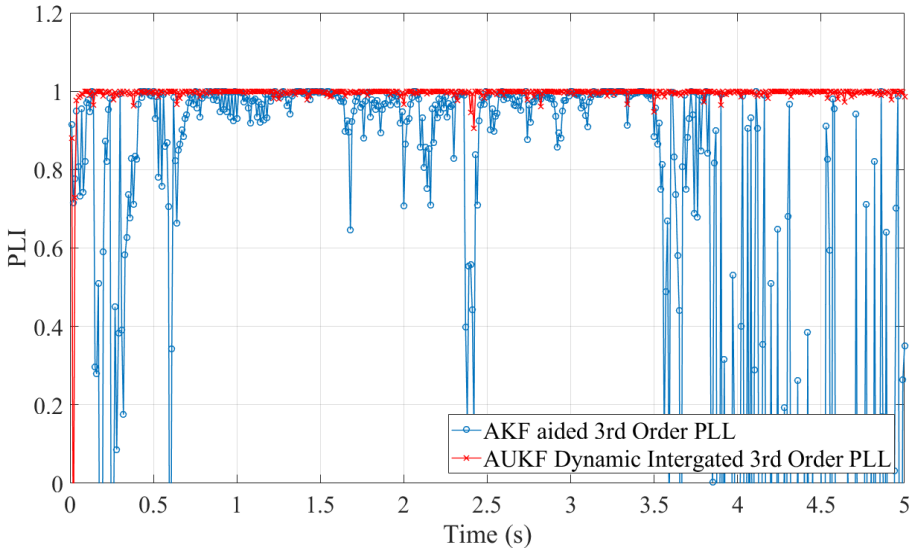

Figure 4.22: Phase lock Loop Indicator Comparison at Bandwidth 13 Hz

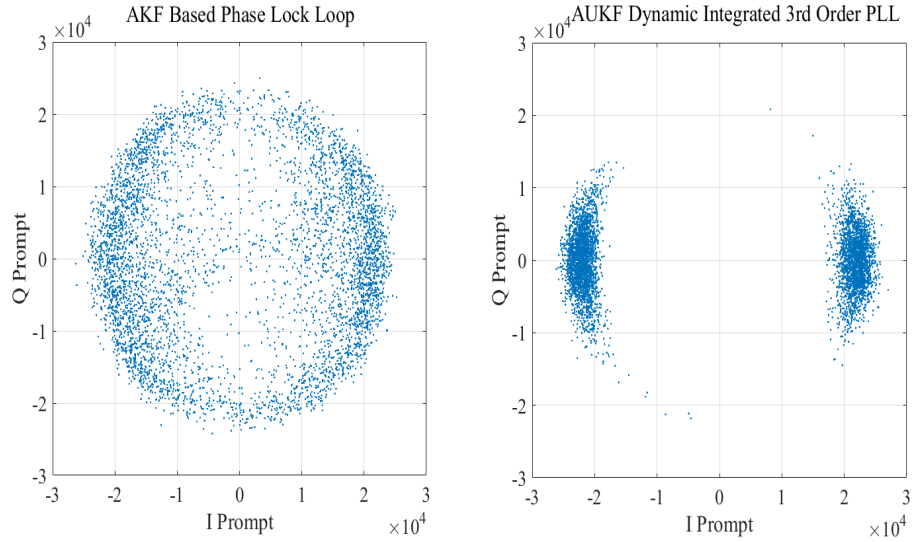

Figure 4.23: Processed I and Q at Bandwidth 13 Hz

4.24 and Figure 4.25 respectively. Under a larger tracking bandwidth, the AKF based PLL contains a relatively higher noise level, the high noise level from the output of the phase discriminator makes the AKF-based PLL carrier tracking loop unstable. However, the proposed approach has significantly better performance compared to the AKF-based PLL approach because of the dynamic integration structure. The information sharing factors are present in Figure 4.26.

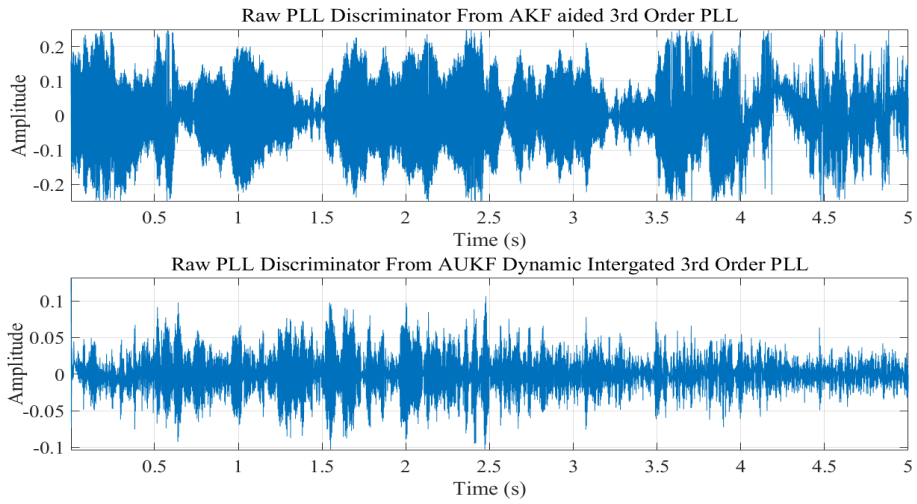

Figure 4.24: Phase Difference Comparison at Bandwidth 13 Hz

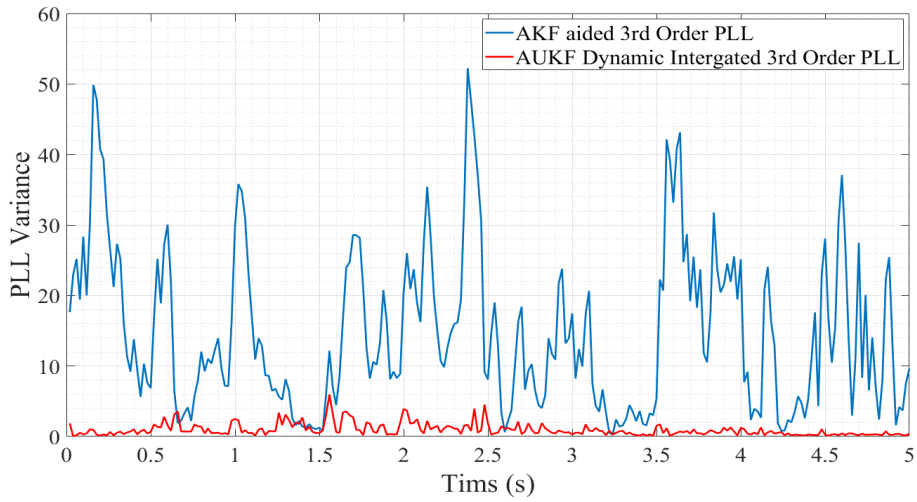

Figure 4.25: Phase Variance Comparison at Bandwidth 13 Hz

Comparing Figure 4.26 to Figure 4.20, the over all trends are similar, which proves the third-order PLL is more sensitive in this integrated system. However, the AUKF-based tracking loop is more robust and this explains why β_2 dominates the integrated system at most times. Furthermore, it is clear to see that the sharing factor in the AUKF-based tracking loop β_2 has a decreasing trend for both 12 Hz and 13 Hz tracking bandwidths, but the decreasing rate of β_2 under 13 Hz is lower

than 12 Hz, which means under a greater tracking bandwidth or higher noise level scenario, the AUKF tracking loop needs a longer time to process in order to track Doppler shift parameters and reduce the noise level. Unlike 12 Hz, under a 1 3Hz

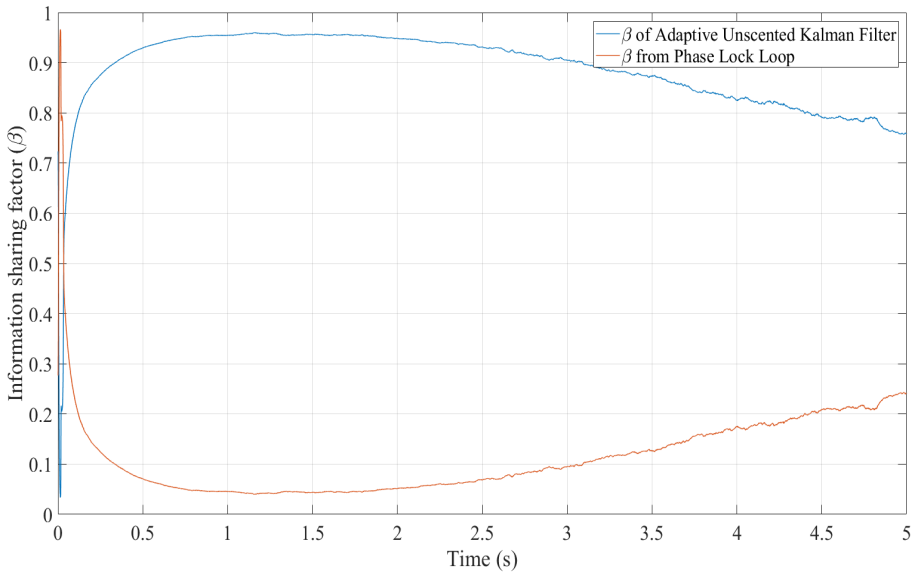

Figure 4.26: Decentralized Information Sharing Factors (β) at Bandwidth 13 Hz

tracking bandwidth the proposed approach has a significant improvement compared to the AKF-based carrier tracking loop, C/N_o has been improved 6 dB on average as Figure 4.27 illustrates. Comparing Figure 4.27 and Figure 4.21, C/N_o from the AKF based carrier tracking loop has dropped by up to 7 dB due to the increased tracking bandwidth, however this does not affect the proposed approach equally. The proposed approach exhibits a strong capability to maintain the C/N_o. As shown in Figure 4.28, the navigation message from the AKF-based carrier tracking loop contains a higher level of noise and eventually loses the lock as in Figure 4.22. In contrast, the proposed approach can still demodulate the navigation message successfully.

4.7 Summary

The carrier tracking loop is considered as the most important link in GPS signal processing and this chapter introduced the generic structure of the GPS carrier tracking loop. The robust and accurate carrier tracking loop can improve the performance of the GPS receiver in order to successfully decode the navigation message. To achieve this, this chapter presented two novel Kalman filter based carrier tracking loops to enhance the carrier tracking ability for GPS signal processing. An AKF uses dy-

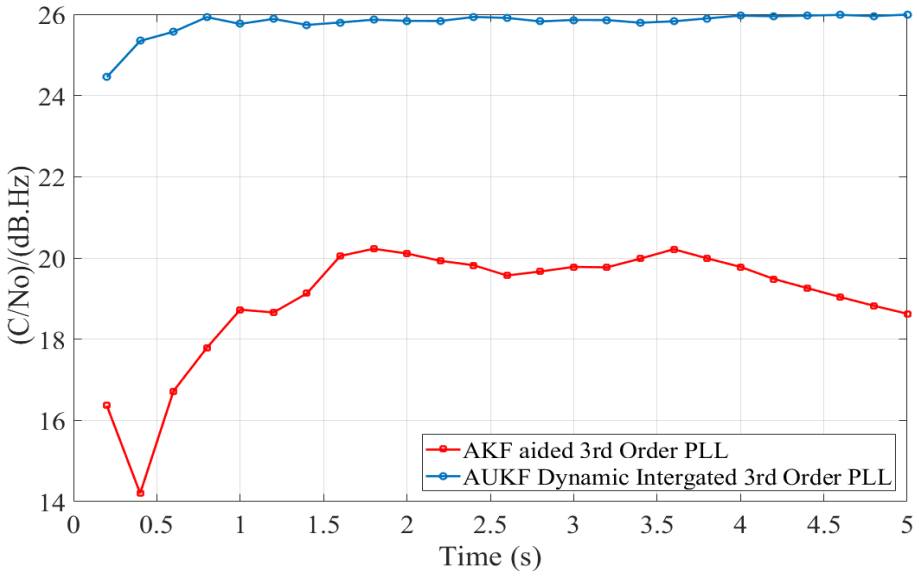

Figure 4.27: Carrier to Noise ratio Comparison at Bandwidth 13 Hz

Figure 4.28: Navigation bits at Bandwidth 13 Hz

namically integrated with a 3rd order PLL carrier tracking loop. The AKF replaces the conventional loop filter in order to dynamically adjust the tracking bandwidth based on the Kalman gain. Furthermore, a novel parallel connection structure has been implemented in this carrier tracking loop, in order to take the advantages of the 3rd order PLL to further reduce the noise level to improve the tracking accuracy.

An AUKF integrated third order PLL based carrier tracking loop has also been proposed. This approach take the unscented transform to linearise the carrier signal phase model so that the adaptive unscented Kalman filter can track the phase of the incoming signal directly. In this structured AUKF works as an open loop, which is more dynamic but the noise level is relatively high in open loop, thus the parallel connected 3rd order PLL is implemented to reduce the noise level generated by the greater tracking bandwidth. These two approaches can improve the tracking ability and retain the tracking accuracy.

The field experiment results indicate that, in a highly dynamic environment, the performance of the dynamic integration scheme is superior to the conventional Kalman filter based tracking loop. Furthermore, it benefits from the adaptive scheme and nonlinear approximation and the AUKF based carrier tracking loop has a significant improvement in highly dynamic and low C/N environments.

Chapter 5

LiDAR Aided IMU/GPS Integration Navigation

5.1 Introduction

Chapters 3 and 4 have proposed and implemented several methods to improve the GPS receiver acquisition and tracking ability. However, in a challenging environment, a GPS receiver alone is not capable of providing accurate and continuous positioning information. The common strategy to obtain a consistent and continuous precise positioning is to integrate GPS and INS [71]. In general, there are two main types of GPS/INS integration schemes. Directly integrating GPS position information with the INS output is named loosely couple [13] [72]. Loosely coupled integration is easy to implement and each sensor works independently, so if one sensor fails, another sensor can still operate and provide navigation information. However, the GPS receiver is required to successfully acquire and track at least four satellites to provide position information, and without a sufficient number of satellite the integration procedure will be terminated. Therefore, the availability of this type of integration is restricted by the GPS availability. Unlike loose integration, tight integration requires only the pseudorange and the pseudorange rate of change from the GPS receiver to provide information for INS [23] [24] [15], and this type of integration is more robust compared to loose integration. However, the model of tight integration is nonlinear, linearising the model can increase the computational cost.

Furthermore, in a GPS signal blocked environment, INS has to work alone to

provide the dead reckoning and attitude estimation [73] [74], a high cost tactical level INS can provide accurate position informations only for a short time, over a long period and the drift of INS can cause the error to increase. Therefore, an alternative sensor is required to reduce the INS drift in a GPS blocked environment. [17] and [18], proposed a digital compass and odometer to provide aiding information such as direction and velocity. However, unlike GPS receivers, these sensors can only provide aiding information in one aspect, so reference position information is required when GPS service is denied.

The LiDAR sensor scans the surrounding obstacles and measures the distance and angle between the obstables and the sensor. The simultaneous location and mapping (SLAM) scheme that provides the relative position can work as an alternative sensor when GPS signal is denied. LiDAR aided navigation system [75] has been successfully implemented for indoor navigation. In an indoor environment, due to the building structures, the feature is unitary and the light interference is weak, therefore, the performance of LiDAR is optimal. However, in the outdoor environment, the building feature, vehicle feature and pedestrian features are combined, so a particular feature is more difficult to extract. Furthermore, the light source outdoors varies and multiple light sources can generate interference and increase the LiDAR sensor measurement noise. [19] and [20] implement a hybrid matching algorithm and extended Kalman filter on LiDAR aided navigation system outdoors. Nevertheless, in both approaches, there is only one central integration filter and the robustness and the performance of the entire system can be degraded if any of the integrated sensors has poor performance.

To mitigate the aforementioned challenges and provide optimal positioning results we propose and implement a low cost 2D LiDAR aided GPS/IMU integration system, using modified feature extraction and a mapping scheme to obtain precise and continuous navigation information. Furthermore, in order to improve the robustness of the integrated navigation system, a novel dynamically integrated federated Kalman filter based integration scheme is proposed and implemented. A standard Kalman filter refers to a centralized filter, whereas federated Kalman filter refers as a decentralized filter. Unlike a standard Kalman filter which processes all the data in one step, a federated Kalman filter is a two stage filter. The first stage of the decentralized filter is to estimate the optimal results from the local data and filter, the second stage is to fuse each individual estimated results through a master

filter to achieve the global best results. Different from the other decentralized filters, federated Kalman filter contain a information sharing process. Through this process, the overall filter reduces the computational cost and increases the robustness.

5.2 General Line Extraction Schemes

In a LiDAR navigation processing, the extracted feature is used to provide the reference navigation and the lines are employed for the feature representation. Lines are the most common and repeatable features in urban environment. Identical line feature from two successive circular scans can be used to provide relative positioning information. Many line extraction algorithms have been proposed using range and angle data from the LiDAR measurement. In this section several common line feature extraction methods are reviewed.

5.2.1 Split and Merge

One of the most popular line extraction is called Split and Merge which is initial from computer vision for robot localization methods [76]. A success implementation in present the algorithm of Split-and-Merge as follow: start from a group of scanned points, the size of this group is predefined as N. Then fit a line from the current group to the next group, and calculate the distance from the point p to the next group. If the distance is less than a predefined threshold value, consider these two groups of data as a whole and fit a line to the next group of data. If the distance is greater than the predefined value, split these two groups at point p. Until all the points are checked, merge the collinear segments [77] .

5.2.2 Line Tracking

Line tracking is a simple line extraction approach which was proposed in [78]. Initially from the first 2 points and fit a line, join the third point and calculate the line parameters. If the line parameters are satisfied the predefined condition, join the next point and calculate the line parameters with the new point joined. If the line parameter is not satisfied the predefined condition, consider this point as a break point or the new point of the next line. Within this approach, the minimum size of a line need to be concerned base on the feature environment.

5.2.3 Random Sampling Consensus

Random sampling consensus also known as (RANSAC), is a generic segmentation method and can be used in many applications, and easy to implement [79]. Similar to Line tracking approach, start from two point and fit a line through these two points. Then calculate the distances of the other points to this line. Create a subgroup, if the number of the subgroup is large enough, recompute the line parameters and store this line.

5.3 LMS Based Line Tracking Approach

After reviewing the above line extraction scheme, we propose a line tracking based feature extraction approach. Since this type of line extraction is more efficient and easy to implement. The output of the LiDAR scanner is a group of the measurement of range and angle from the scanner to the obstacle. These measurements are denoted as ρ and α which are correspond to polar coordinate. The relationship between the Polar coordinate and Cartesian coordinate is expressed as Eq.(5.1).

$$\rho = \bar{x}cos(\alpha) + \bar{y}sin(\alpha) \tag{5.1a}$$

$$\alpha = \frac{1}{2}tan^{-1}(\frac{2 \cdot \sum_{i=1}^{N}(\bar{x} - x_i) \cdot (\bar{y} - y_i)}{\sum_{i=1}^{N}(\bar{y} - y_i)^2 - \sum_{i=1}^{N}(\bar{x} - x_i)^2}) \tag{5.1b}$$

$$\bar{x} = \frac{1}{N}\sum_{i=1}^{N} x_i \tag{5.1c}$$

$$\bar{y} = \frac{1}{N}\sum_{i=1}^{N} y_i \tag{5.1d}$$

where x and y are the coordinates of the scanning point in Cartesian coordinate, N is the total scanning points in a line. The line feature extraction starts from creating a line by joining the first two scanning points. The parameters of this line can be calculated using least mean square (LMS) [77].

Each successive scanning point is then joined to the line until either the Euclidean distance D_E between the new point to the line is greater than a threshold value or the standard deviation of the line σ_l with the new point is greater than the predefined threshold.

$$D_E = \rho - x_icos(\alpha) - y_isin(alpha) \tag{5.2}$$

where the standard devision of the distance between the scanning point to the extracted line is calculated as Eq.(5.3)

$$\sigma_l = \sqrt{\frac{\sum_{i=1}^{N} \rho - x_i cos(\alpha) - y_i sin(\alpha)}{N-1}} \tag{5.3}$$

This new joined point is consider as either a break point or the first point of the new line.

5.3.1 Line Mapping

It is important to identify a line in one scan is corresponded to the next scan in order to estimate the relative position and attitude of the LiDAR scanner. To address this identical lines, study [80] proposed to estimate the location of the intersection point regarding to the perpendicular line and the extracted line to identify the identical lines. However the computational cost of this method is high, in a very dense feature environment, this method is not efficient. Therefore, to reduce the computational cost and increase the processing speed, in this project, we map the corresponding lines using the least square criterion.

The extracted line feature is considered as a linear function. $a_n^j x_i + b_n^j y_i + c = 0$, where n and i represents the number of scanning circle and the number of points attached on j_{th} the line. The perpendicular distance between the scanning point and the extracted line can be obtained as

$$d_{i,j}^n = \frac{a_j x_i + b_j y_i + c}{\sqrt{a^2 + b^2}} \tag{5.4}$$

Total distance D

$$D_j^n = \sum_{i=1}^{S} \frac{a_j x_i + b_j y_i + c}{\sqrt{a_j^2 + b_j^2}} \tag{5.5}$$

where S is the total point in a line. Since the line is extracted by the LMS, the total distance of the attach point to the line is a unique value and retain the same within two scans. Therefore, if the criteria is $|D_j^{n+1} - D_j^n| \leq D_{threshold}$, then the two lines which are extracted in two times are considered as the same one.

5.4 Quaternion Based IMU Attitude Mechanization

Another sensor in our integration scheme is the IMU. The measurement of IMU is based on the body-frame, however the orientation of the platform is in n-frame. The transformation of the reference frame is the key component of attitude mechanization. In general, there are three transformation method which are Eular angles, Direct Cosine Matrix(DCM) and Quaternion [81]. In this project, we use quaternion based transformation method because of its computational efficiency and gimbal-lock avoidance. A quaternion Q can be defined as Eq.(5.6)

$$Q = q_0 + q_1 i_0 + q_2 j_0 + q_3 k_0 \tag{5.6}$$

The rotation matrix from body-frame to n- frame C_b^n can be obtained as Eq.(5.7) [82] [83].

$$C_b^n = \begin{bmatrix} q_0^2 + q_1^2 - q_2^2 - q_3^2 & 2(q_1 q_2 - q_0 q_3) & 2(q_1 q_3 + q_0 q_2) \\ 2(q_1 q_2 + q_0 q_3) & q_0^2 - q_1^2 + q_2^2 - q_3^2 & 2(q_2 q_3 - q_0 q_1) \\ 2(q_1 q_3 - q_0 q_2) & 2(q_2 q_3 + q_0 q_1) & q_0^2 - q_1^2 - q_2^2 - q_3^2 \end{bmatrix} \tag{5.7}$$

Denote rotation matrix C_b^n as

$$C_b^n = \begin{bmatrix} T_{11} & T_{12} & T_{13} \\ T_{21} & T_{22} & T_{23} \\ T_{31} & T_{32} & T_{33} \end{bmatrix} \tag{5.8}$$

The attitude Pitch, Roll and Yaw can be obtained from quaternion matrix as Eq.(5.9) [84]

$$\begin{aligned} Pitch(\Phi) &= sin^{-1}(T_{32}) \\ Roll(\Theta) &= tan^{-1}(-\frac{T_{32}}{T_{33}}) \\ Yaw(\Psi) &= tan^{-1}(\frac{T_{12}}{T_{22}}) \end{aligned} \tag{5.9}$$

The gyroscope is used to measure the angular velocity, to integrate the angular velocity can obtain the attitude information, however the external force and gravity

can significantly dilute the attitude estimation. Therefore, accelerometer which can measure the external forces is required. In our application, beside gyroscopes and accelerometer, a magnetometer is also implemented in order to provide azimuth aided information.

5.4.1 Quaternion From Gyroscope Reading

To implement Kalman filter, a state model is required, in our approach, the attitude quaternion is chosen as the sate vector, state matrix $Q = [q_0, q_1, q_2, q_3]$ can be model as Eq.(5.10) [85] [86] [87], Eq.(5.10) is the first order of quaternion kinematic equation.

$$Q_t = \frac{T_s}{2}\Omega(\omega)Q_{t-1} \tag{5.10}$$

where ω is the angular velocity measured by the gyroscope.

$$\omega = \begin{bmatrix} \omega_x \\ \omega_y \\ \omega_z \end{bmatrix} \tag{5.11}$$

$\Omega\times$ is the skew-symmetric matrix of the angular velocity presents as Eq.(5.12)

$$[\Omega\times] = \begin{bmatrix} 0 & -\omega_x & -\omega_y & -\omega_z \\ \omega_x & 0 & \omega_z & -\omega_y \\ \omega_y & -\omega_z & 0 & \omega_x \\ \omega_z & \omega_y & -\omega_x & 0 \end{bmatrix} \tag{5.12}$$

Where T_s is the time interval. Eq.(5.10) is commonly used as a state model in Kalman filter or Extended kalman filter [86] [88].

5.4.2 Quaternion From Accelerometer Reading

The output of the accelerometer could be used as the measurement value as research [84]. The output of the accelerometer measurement is denoted as $a = [a_x a_y a_z]^t$, through the rotation matrix Eq.(5.7), the acceleration can be expressed as

$$C_b^n \cdot \begin{bmatrix} 0 \\ 0 \\ 1 \end{bmatrix} = \begin{bmatrix} a_x \\ a_y \\ a_z \end{bmatrix} \tag{5.13}$$

expanding the multiplication, the Eq.(5.13) can be expressed as

$$\begin{aligned} 2(q_1q_3 + q_0q_2) &= a_x \\ 2(q_2q_3 - q_0q_1) &= a_y \\ q_0^2 - q_1^2 - q_2^2 - q_3^2 &= a_z \end{aligned} \tag{5.14}$$

In Eq.(5.14), it is obviously that the number of the solution is infinity, to avoid this problem, we choose $q_3 = 0$, since the vehicle runs on the ground, we can consider the upper velocity is zero. Then the simplified equation can be expressed as Eq.(5.15) present.

$$\begin{aligned} 2q_0q_2 &= a_x \\ -2q_0q_1 &= a_y \\ q_0^2 - q_1^2 - q_2^2 &= a_z \end{aligned} \tag{5.15}$$

To solve the above equations, we use the shortest path quaternion formulation [89], the result can be obtained as Eq.(5.16) present

$$q = \begin{bmatrix} \sqrt{\frac{a_z+1}{2}} \\ -\frac{a_y}{\sqrt{2(a_z+1)}} \\ \frac{a_x}{\sqrt{2(a_z+1)}} \\ 0 \end{bmatrix} \tag{5.16}$$

5.5 Dynamic Federate Kalman Filter Approach

As we mentioned before, IMU cannot provide an accurate navigation result for a long period in GPS denied environment, due to the error accumulation. The IMU error propagation model need to work alongside with the system motion model in order to further correct the error.

A 15 states vector which contain the errors of position δr_{xyz}, velocity δv_{xyz}, attitude ε_{xyz} and the bias of accelerometer δb_a and gyroscope δb_g are denoted as below:

$$x = [\delta r_{xyz}\ \delta v_{xyz}\ \delta \varepsilon_{xyz}\ \delta b_a\ \delta b_g] \tag{5.17}$$

As discussed in Section 2.6.2, the error model is used as a dynamic system model as Eq.(5.18)

$$\begin{bmatrix} \delta\dot{r} \\ \delta\dot{v} \\ \delta\dot{\varepsilon} \\ \delta\dot{b_a} \\ \delta\dot{b_g} \end{bmatrix}_t = \begin{bmatrix} F_{rr} & F_{rv} & F_{r\varepsilon} & 0_3 & 0_3 \\ F_{vr} & F_{vv} & F_{v\varepsilon} & C_b^n & 0_3 \\ F_{\varepsilon r} & F_{\varepsilon v} & F_{\varepsilon\varepsilon} & 0_3 & C_b^n \\ 0_3 & 0_3 & 0_3 & \beta_{ba} & 0_3 \\ 0_3 & 0_3 & 0_3 & 0_3 & \beta_{bg} \end{bmatrix} \cdot \begin{bmatrix} \delta r \\ \delta v \\ \delta\varepsilon \\ \delta b_a \\ \delta b_g \end{bmatrix}_{t-1} + \begin{bmatrix} C_b^n & 0_3 & 0_3 & 0_3 \\ 0_3 & C_b^n & 0_3 & 0_3 \\ 0_3 & 0_3 & I_3 & 0_3 \\ 0_3 & 0_3 & 0_3 & I_3 \end{bmatrix} \cdot \begin{bmatrix} \eta_a \\ \eta_g \\ \eta_{ba} \\ \eta_{bg} \end{bmatrix} \tag{5.18}$$

The differences of position, velocity and attitude between GPS, IMU and LiDAR are used in measurement model. The measurement value can be classified in two types which are IMU measurement and LiDAR measurement respectively.

The IMU measurement

$$z_{IMU} = \begin{bmatrix} r_{IMS} - r_{GPS} \\ v_{IMU} - v_{GPS} \end{bmatrix} \tag{5.19}$$

The LiDAR measurement

$$z_{LiDAR} = \begin{bmatrix} r_{LiDAR} - r_{IMU} \\ v_{LiDAR} - v_{IMU} \\ \varepsilon_{LiDAR} - \varepsilon_{IMU} \end{bmatrix} \tag{5.20}$$

It is an intuition that in the open environment, LiDAR extracted feature is rare but the GPS performance is the optimal. Under this scenario, GPS and IMU measurement are the mainly integrated. In the contrast, in the narrow environment, GPS performance is degraded, but the LiDAR feature is sufficient, then the IMU/LiDAR integration dominates the entire integration system.

The proposed integration scheme is inspired by this intuition, two federated Kalman filters are connected in parallel as in Figure 5.1 presented.

In time update:

$$x_t = F_t x_{t-1} \tag{5.21}$$

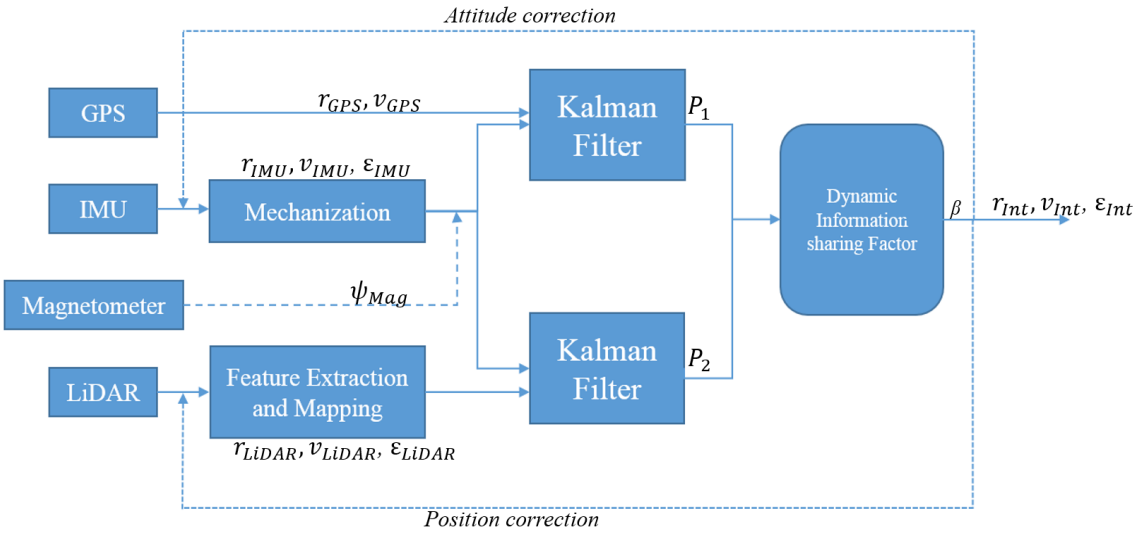

Figure 5.1: Integrated Federate Kalman Filter

where x is the interest state vector, F is the transient control matrix. The variance of the prediction $\hat{x}_{t|t-1}$ and x_t is given as Eq.(5.22)

$$P_{t|t-1} = [E(x_t - \hat{x}_{t|t-1})(x_t - \hat{x}_{t|t-1})^T] \tag{5.22a}$$

$$P_{t|t-1} = F_t P_{t-1|t-1} F_t^T + Q_t \tag{5.22b}$$

Q is the system process noise covariance can be obtained by the bias of the gyroscope and the accelerometer $Q = diag(\delta b_g, \delta b_a)$.

The IMU/GPS integration measurement equation is as Eq.(5.23)

$$\begin{aligned} z_{(IMU,t)} &= H_t^{IMU} x_t \\ H_t^{IMU} &= \begin{bmatrix} I_{3\times3} & 0 & 0 & 0 & 0 \\ 0 & I_{3\times3} & 0 & 0 & 0 \end{bmatrix} \end{aligned} \tag{5.23}$$

The IMU/LiDAR integration measurement equation is as Eq.(5.24)

$$\begin{aligned} z_{(LiDAR,t)} &= H_t^{LiDAR} x_t \\ H_t^{LiDAR} &= \begin{bmatrix} I_{3\times3} & 0 & 0 & 0 & 0 \\ 0 & I_{3\times3} & 0 & 0 & 0 \\ 0 & 0 & I_{3\times3} & 0 & 0 \end{bmatrix} \end{aligned} \tag{5.24}$$

The measurement update is processed as Eq.(5.25), and the covariance matrix $P_{t|t}$

can be updated as Eq.(5.26)

$$\hat{x}_{t|t} = \hat{x}_{t|t-1} + K(z - H_t\hat{x}_{t|t-1}) \tag{5.25}$$

$$P_{t|t} = P_{t|t-1} - K_t H_t P_{t|t-1} \tag{5.26}$$

where K is the Kalman gain. As in Eq.(4.44a) present, the value P represents the uncertainty of each federated Kalman filter. In our proposed dynamic integration technique, this P value is used to decide the weight of each subsystem.

The proposed dynamic integration filter is consisted in two subsystems. The covariance matrix of subsystem $i_{IMU/GPS}$ and $i_{IMU/LiDAR}$ can be estimated in each federated Kalman filter. The more stable subsystem will take more sharing in the integrated system. The integrated results need to feed back to the IMU and LiDAR measurement to correct their measurement results.

5.6 External Direction Aiding

The Yaw error which is generated by the IMU mechanization could be updated by the external sensor. Digital compass, magnetometer are the common sensors for direction measurement. In this project, we adopt a magnetometer to provide extra direction aiding. The IMU attitude error has been modelled as Eq.(5.27)

$$\delta\omega_{in}^{n} = [\frac{\partial\hat{\omega}_{in}}{\partial\hat{\varepsilon}}, \frac{\partial\hat{\omega}_{in}}{\partial\hat{V}}] \begin{bmatrix} \delta\varepsilon \\ \delta V \end{bmatrix} \tag{5.27}$$

The error of Yaw $\delta\Psi$ can be obtained by partial derivative of Eq.(5.27)

$$\delta\hat{\Psi} = \frac{\partial\hat{\Psi}}{\partial\varepsilon_E}\delta\varepsilon_E + \frac{\partial\hat{\Psi}}{\partial\varepsilon_N}\delta\varepsilon_N + \frac{\partial\hat{\Psi}}{\partial\varepsilon_U}\delta\varepsilon_U \tag{5.28}$$

The difference of the yaw measurement which obtained from IMU and magnetometer is equal to Eq.(5.29)

$$\delta\hat{\Psi} = \Big[\Psi_{IMU} - \Psi_{Mag}\Big] = H \cdot \delta x \tag{5.29}$$

where

$$H = \Big[0_{1\times6} \quad \frac{\partial\hat{\Psi}}{\partial\varepsilon_E} \quad \frac{\partial\hat{\Psi}}{\partial\varepsilon_E} \quad \frac{\partial\hat{\Psi}}{\partial\varepsilon_E} \quad 0_{1\times6}\Big] \tag{5.30}$$

where

$$\begin{aligned}\frac{\partial\hat{\Psi}}{\partial\varepsilon_E} &= \frac{\hat{T}_{12}T\hat{T}_{32}}{[\hat{T}_{22}]^2+[\hat{T}_{12}]^2}\\ \frac{\partial\hat{\Psi}}{\partial\varepsilon_N} &= \frac{\hat{T}_{22}\hat{T}_{32}}{[\hat{T}_{22}]^2+[\hat{T}_{12}]^2}\\ \frac{\partial\hat{\Psi}}{\partial\varepsilon_U} &= \frac{\hat{T}_{22}T_{22}+\hat{T}_{12}T_{12}}{[\hat{T}_{22}]^2+[\hat{T}_{12}]^2}\end{aligned} \tag{5.31}$$

The magnetometer measure the local magnetic field, and the orientation can be estimated by the direction of the magnetic field. Through the output of the magnetometer $(x_{mag}, y_{mag}, z_{mag})$ the orientation Ψ can be obtained as Eq.(5.32) [90].

$$\begin{aligned}\Psi_{Mag} = atan2[&-y_{mag}\cdot cos(\Theta)+z_{mag}\cdot sin(\Theta),\\ &x\cdot cos(\Phi)+y\cdot sin(\Phi)sin(\Theta)+z\cdot sin(\Phi)cos(\Theta)]\end{aligned} \tag{5.32}$$

5.7 Experiment Setup and Results Analysis

To compare and analyse the proposed solution, several experiments are conducted. The following sections present the detail of the experiment and the analysis of the experiment results.

5.7.1 Experiment Setup

The connection diagram and the experiment set up are presented as Figure 5.3 and 5.2. A low cost 360 degree 2D LiDAR (the 1^{st} component in the figure) is used to scan the surrounded obstacles and measure the distance and the angle between the sensor and the obstacles. Its scanning frequency can reach to 5.5Hz with 6 meters scanning range. A USB 2.0 connector provide the connectivity to the data stream and power supply. The distance measurement resolution of this 2D LiDAR is $\leq 5mm$ in no more than 1% of the distance measurement and the angle measurement resolution is $\leq 1^{\circ}$. The GPS data is collected by an active antenna attach a Septentrio PolaRX5 GPS receiver (the 2^{nd} and the 3^{rd} component in the figure), the Septentrio PolaRX5 is a multi-constellation and multi-frequency reference receiver. In order to reduce the error which is generated by time misalign, a uniform time resource is required. The 1 PPS output port of the GPS receiver can work as a time reference in order to provide a precise time synchronization for GPS receiver and the other sensors. The

rigid body data is obtained from a xsens IMU (MTi-10) (the 4^{th} component in the figure). This low cost IMU contains three gyroscopes , three accelerometers and a magnetometer which can provide 9 degree of freedom rigid body information. The in-run stability of the gyroscope and the accelerometer are $18°/h$ and $15\mu g$, the bias error of the gyroscope and the accelerometer are $0.2°/h$ and $5mg$ receptively. The total RMS noise of the magnetometer is $0.5mG$ with the resolution is $0.25mG$. The sampling frequency of the IMU in this experiment is set to be 200 Hz. In order to simulate the vehicular environment, all the devices are placed on a trolley.

Figure 5.2: Experiment Setup

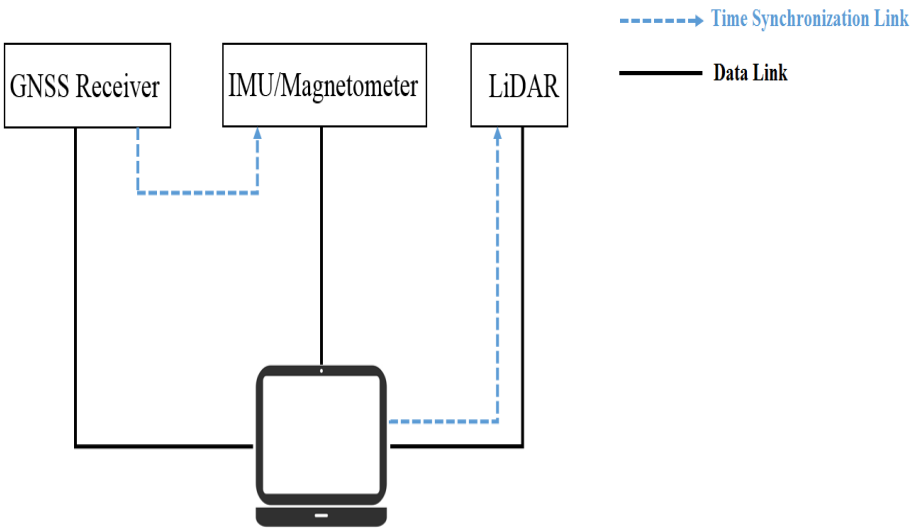

Figure 5.3: Connection Block Diagram

5.7.2 Synchronization Design

5.7.2.1 GPS Receiver and IMU Synchronization

As mentioned in the previous section, the 1PPS output port of the GPS receiver can work as a time reference in order to synchronize the IMU. The connectivity of the time synchronization is introduced in this section. Firstly, a CA-MP2-MTi and a CA-USB-MTi connectors are required, CA-MP2-MTi connector allow the full control of IMU (MTi-10) and hardware synchronization option. The lead of CA-MP2-MTi is presented as Figure 5.4 and its pin allocation is illustrated as Table 5.1 [91]

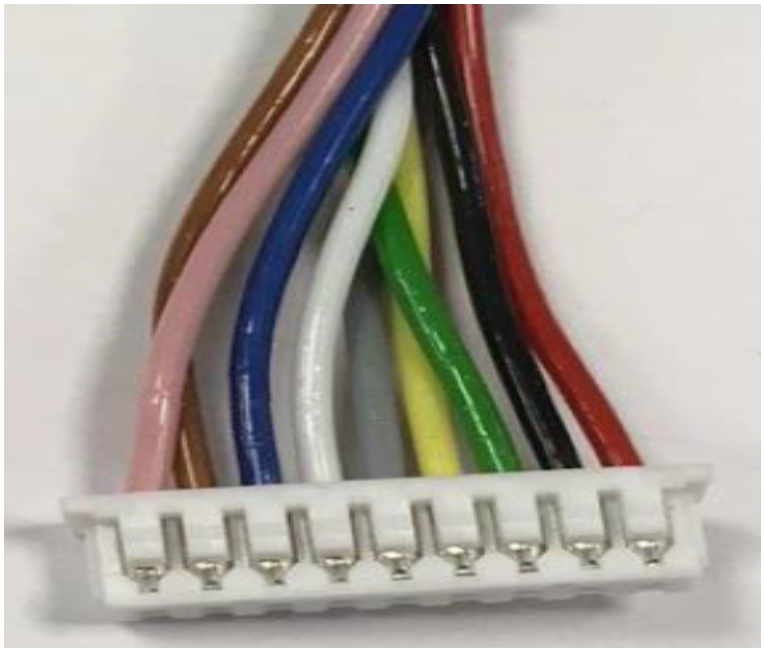

Figure 5.4: CA-MP2-MTi

Table 5.1: CA-MP2-MTi Pin Allocation

Function	**Wire colour CA-MP2**	**Fischer pin No.**	**Molex pin No.**
GND	Black	1	2
RS232 Tx	Yellow	2	4
RS232 Rx	Grey	3	5
Vin(4.5-30V)	Red	4	1
SyncIn	Blue	5	7
SyncOut	Pink	6	9
ClockSync	Brown	7	8
USB DP(D+)	Green	8	3
USBDM(D-)	White	9	6
Shielding	SH	SH	N/A

The CA-USB-MTi connection diagram is illustrated as Figure 5.5, it provide

the connectivity for the MTI-10 and the external device synchronization and power supply by PC USB port.

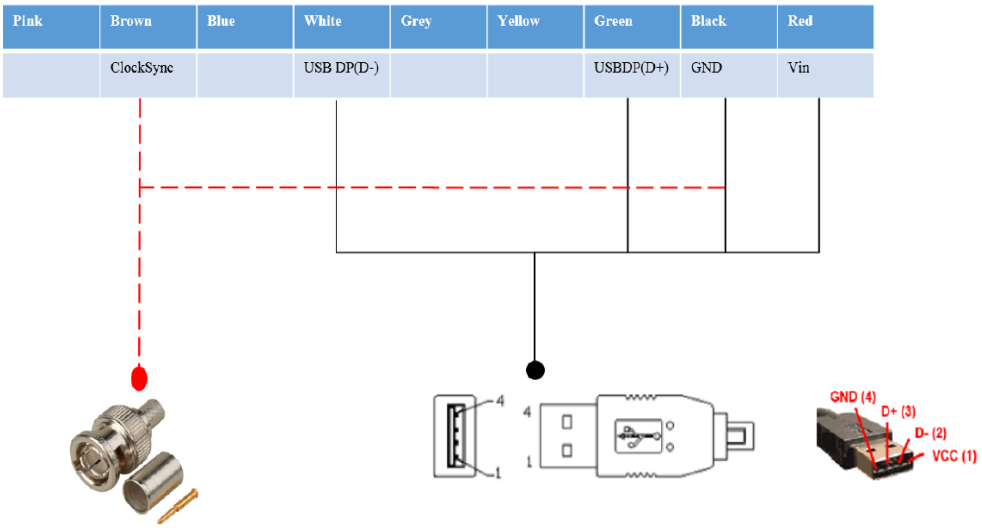

Figure 5.5: USBConnection

5.7.2.2 LiDAR Sensor Synchronization

Regarding to the LiDAR sensor time synchronization, the measurement of the LiDAR sensor contains a time tag from the PC using NTP(Network Time Protocol). Although the LiDAR sensor synchronization is not as precise as GPS/IMU, the low measurement frequency and data sampling frequency could reduce the effect which is caused by time misalign. In the experiment, as Figure 5.6 present, within a time interval of the LiDAR measurement, we calculate the instantaneous location which could align the results of the IMU/GPS measurement.

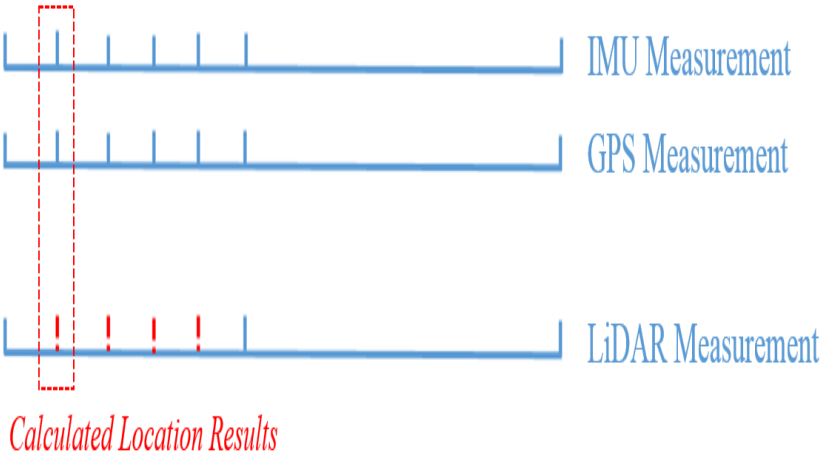

Figure 5.6: Multisensor Synchronization

5.7.3 Test Route and Scenario Design

The testing trajectory is carefully designed in order to evaluate the performance of the integrated system. To obtain the best location information, the testing route starts from an open view area where the GPS receiver can obtain the optimal performance. Therefore, the integration performance is mainly decided by the GPS receiver and the IMU coupling results, since LiDAR cannot obtain a sufficient location information. Then to evaluate the LiDAR aiding results, the following two scenarios need to be concerned. As Figure 5.7 presented, scenario 1 presents a trajectory which the trolley pass from an open view environment to a satellite signal deny environment and the scenario 2 presents a very narrow sky view which can generate a very dense multipath environment. These two scenarios are common to vehicular communication under urban environment which can degrade the GPS receiver position.

Figure 5.7: LiDAR Navigation

It is an intuition that under a unban environment the performance of the GPS positioning is poor. However, the LiDAR sensor can extract sufficient number of line features and operate as a GPS alternate. Figure 5.8 and Figure 5.9 present the data cloud from two successive times of LiDAR scanning. Feature 1,2,3 represent the identical lines from two scans. LiDAR sensor process relative navigation using these identical lines.

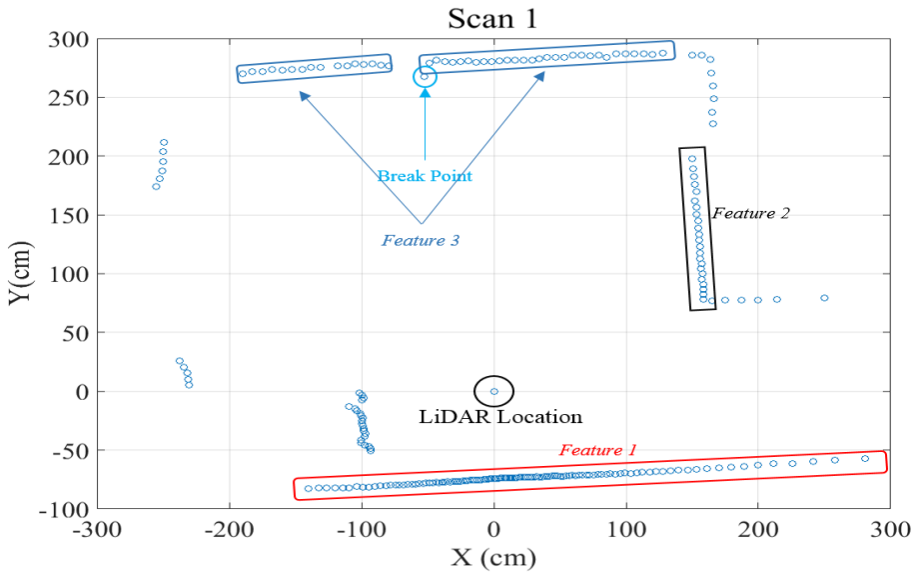

Figure 5.8: Line Feature extraction From 1^{st} scan circle

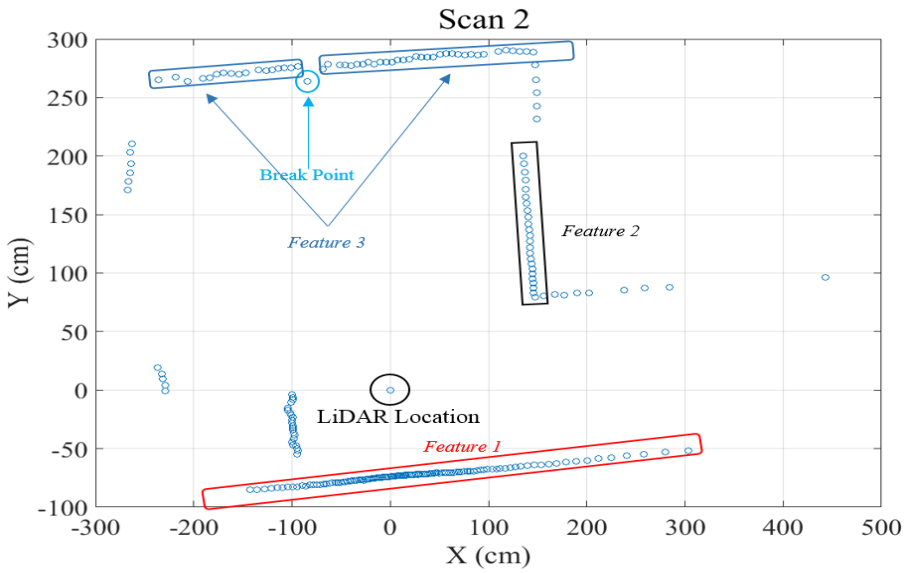

Figure 5.9: Line Feature extraction From 2^{nd} scan circle

5.7.4 Experiment Results and Analysis

The data from each individual sensor are collected and stored in a laptop for post processing. A MATLAB R2017a is used for data processing and analysing.

5.7.4.1 Location Results and Accuracy

The position results in this experiment are compared between LiDAR aided IMU/GPS based on Kalman filter and LiDAR aided IMU/GPS based on the proposed dynamic integration scheme respectively. Kalman filter based approach is a conventional multisensor data fusion scheme and widely used in various of applications, within this approach, Kalman filter works as a central filter to fuse the data from different receivers.

The experiment results mainly evaluate and compare the positioning consistency and accuracy. Figure 5.10 presents the number of satellites being tracked. In the beginning of the experiment, in an open view environment, the number of tracked satellites is 18 then the number decreased since the receiver enters to a building area. In the worst situation, the number of the tracked satellites is zero that would deny the positioning service completely. Due to this problem, the multisensor technique for positioning is essential.

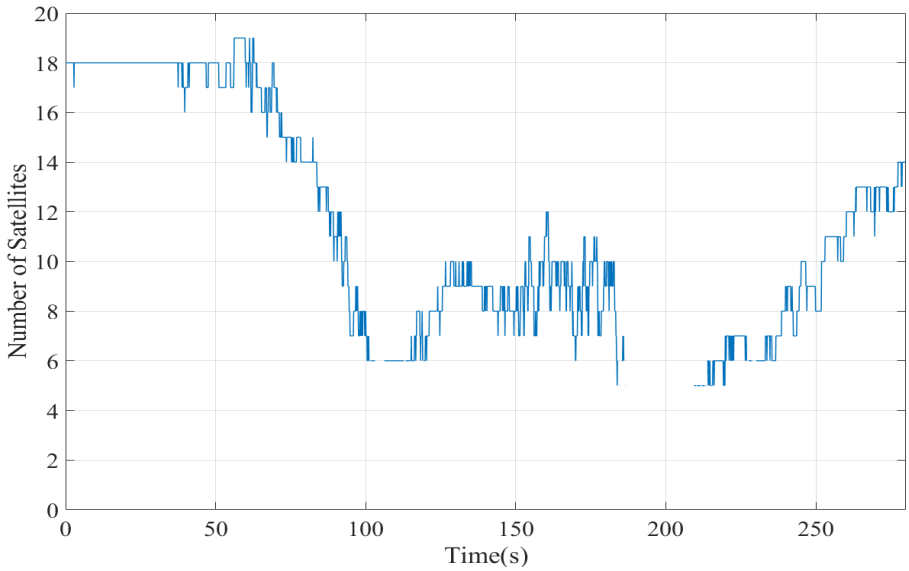

Figure 5.10: Number of Tracked Satellites

Figure 5.11 and Figure 5.12 present the longitude and latitude comparison results between two integration schemes and the reference. As the figures presented, the GPS receiver alone cannot provide a continuous measurement due to the signal

blockage and attenuation. Under this circumstance, the IMU corrected information is provided by LiDAR. With two integration approaches, the comparison results indicate that the dynamically integrated approach can obtain a better performance in general especially when GPS signal is not available. As the comparison results indicate the performance of the integration results are not consistent due to the change of the environment. This change is illustrated in Google map plot.

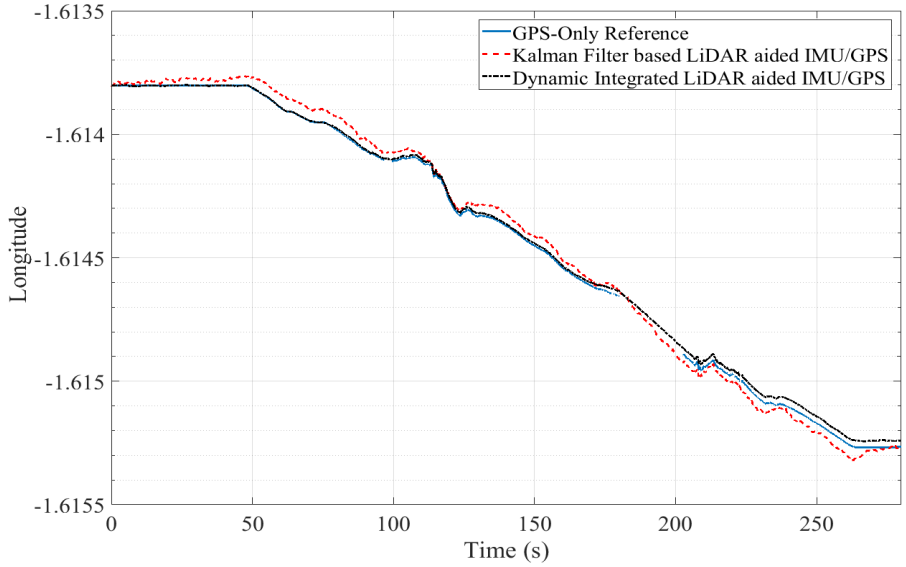

Figure 5.11: Longitude Results Comparison

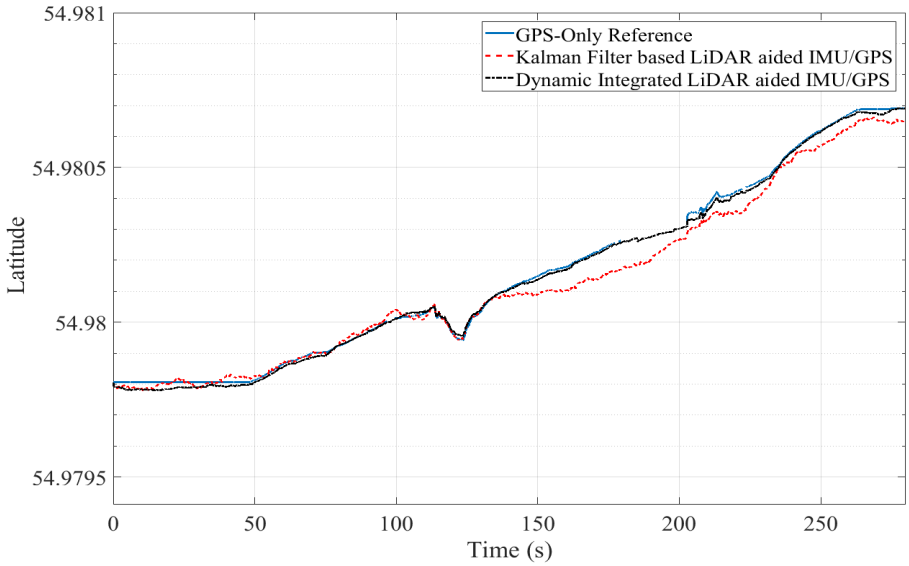

Figure 5.12: Latitude Results Comparison

Figure 5.13 presents the 2D trajectory on Google map. As the figure presents the experiment start in front of the Merze court where considered as an open view environment. Under this scenario LiDAR sensor cannot achieve an optimal per-

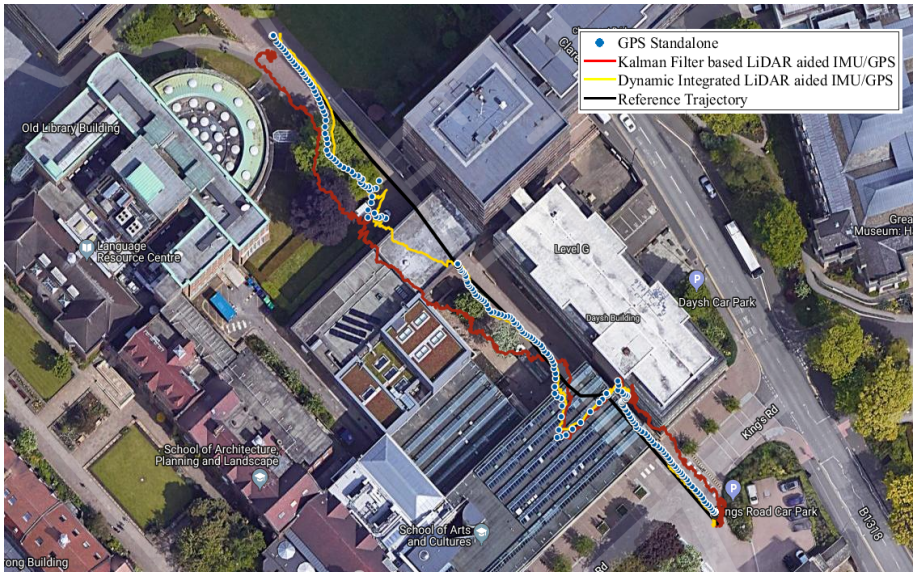

Figure 5.13: Trajectory Comparison

formance since the surrounded obstacles are further than the maximum scanning distance, therefore the LiDAR sensor contributes more noise than aiding information. Therefore, the IMU/GPS integration results should take more weight in the entire system and reduce the influence of the LiDAR. However, the conventional integrated Kalman filter uses the central filter and treat all sensor equally, this structure is less dynamic when the performance of one sensor is significantly poor.

It is clear to see that the overall integration results of Kalman filter based approach contain a systematic error which cause the results retain a constant bias from the reference trajectory, this systematic errors are mainly generated by each sensors. The results from the Kalman filter based approach indicate that the overall performance is not ideal in the beginning and the first part of the experiment especially when the trolley enters to a GPS signal denied environment. However, this approach can achieve a better performance in the last part of the experiment, this prove that the Kalman filter need a long time to converge the filtering results.

In contrast, the proposed integration scheme can overcome this challenge. The sharing factors within the proposed approach which are corresponded to each individual subsystem. These factors could minimize the contribution which made by the less stable subsystem in order to improve the entire system and reduce the systematic error which generated by the unstable sensor. LiDAR sensor could normally achieve a better performance since the extracted features are sufficient when the system is operating under a GPS signal denied environment. Under this scenario, we prefer the LiDAR/IMU integration could take more percent and reduce the effect

of GPS receiver. The result figures show that the proposed method could retain the positioning results in a relevant high accurate level especially when the satellites signal is completely lost. The experiment results indicate that the trees and buildings can affect the performance of the GPS receiver. At the last part of the experiment, the position accuracy drops significantly because of the tall buildings, the H shape of the tall building is the major challenge to the low elevation satellites signals, as it could block the low elevation satellites signals and dilute the accuracy of positioning

The standard deviation σ evaluate the accuracy of the position estimation between two algorithm. Within an epoch, smaller σ indicates the smaller vibration of the estimation results. In order to obtain an accurate standard deviation value, the epoch is one fifth of second. Figure 5.14 and Figure 5.15 represent the standard deviation of X and Y estimation with respect to two approaches.

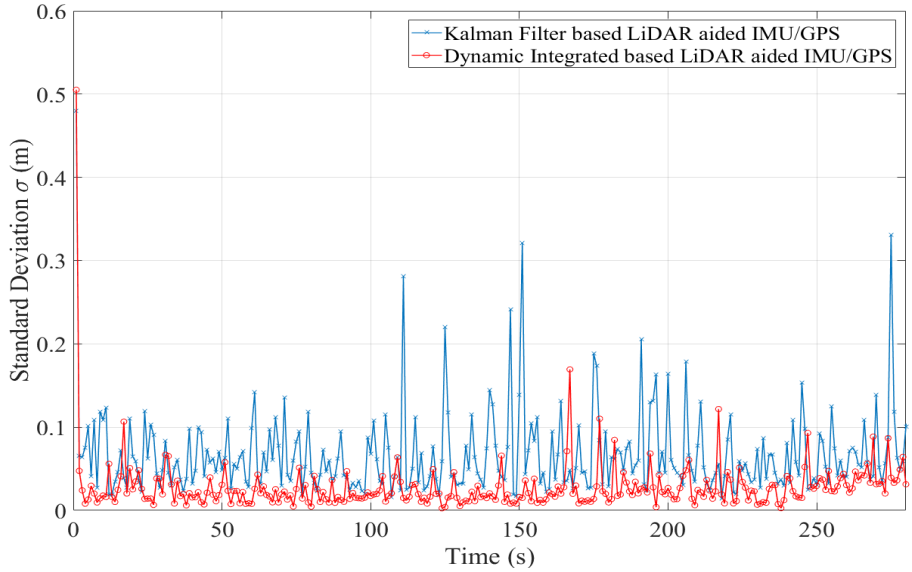

Figure 5.14: Standard Deviation of X

The comparison results show that the Kalman filter based approach has a relevant high variance within an epoch however the dynamic integrated approach gains a smaller σ which can indicate the proposed approach is more stable and accurate compare to the Kalman filter based approach. Figure 5.16 and Figure 5.17 present the position error status, namely meters and RMSE between two integration approaches regarding to the reference. The results indicate that the proposed approach is superior than the conventional Kalman filter based approach with respect in accuracy and resilience. Furthermore, the performance of the dynamic integrated approach is more robust compare to the conventional Kalman filter based method since the error increasing rate is much lower when the environment change.

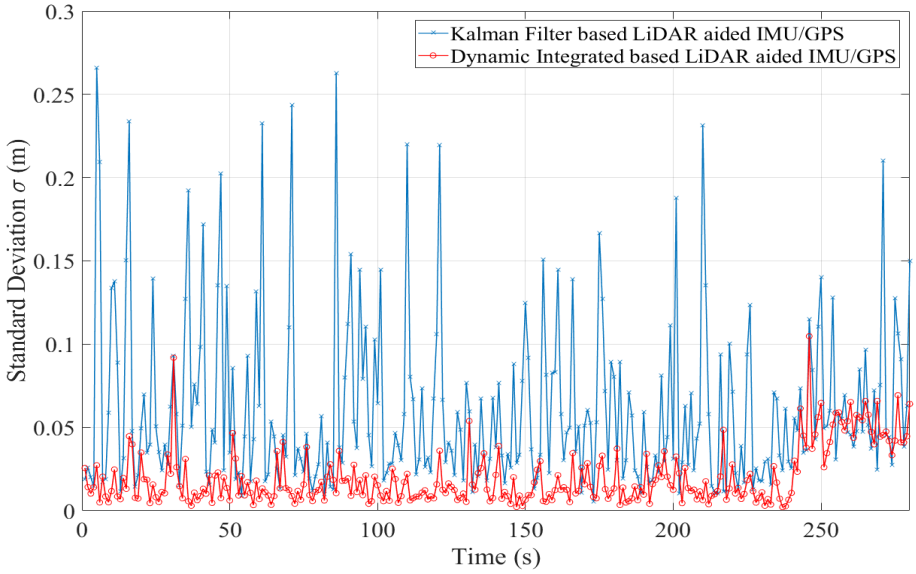

Figure 5.15: Standard Deviation of Y

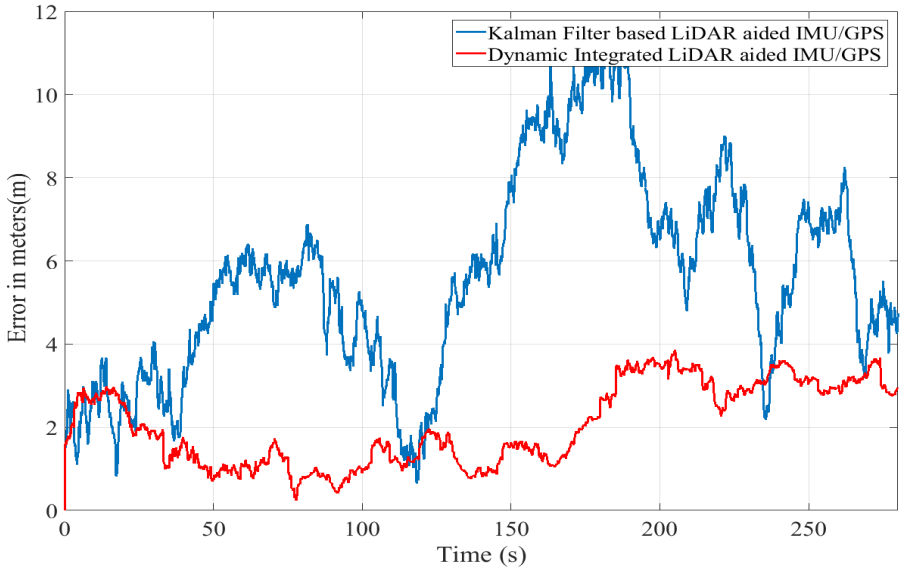

Figure 5.16: Error in Meters

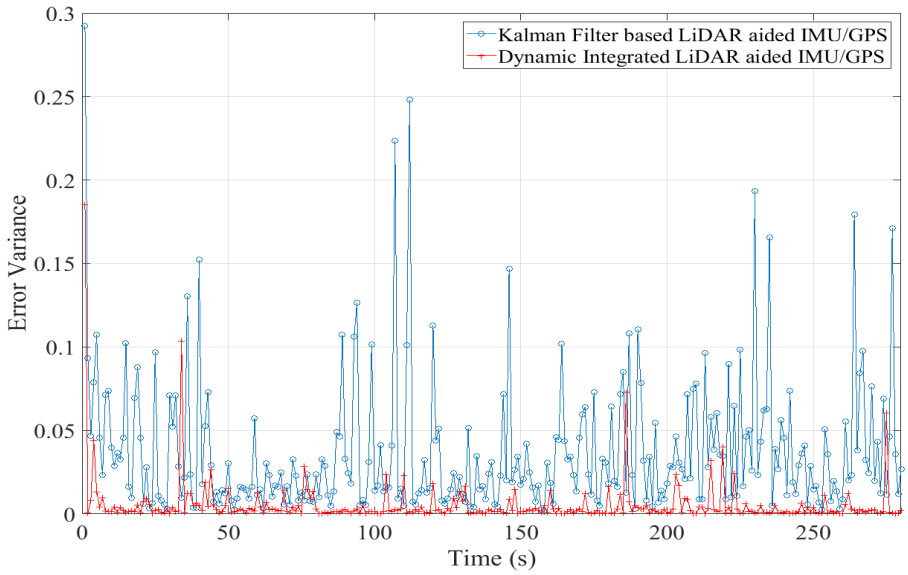

Figure 5.17: RMSE

5.8 Summary

This chapter presented a novel multisensor data fusion approach for continuous and accurate positioning. To efficiently use LiDAR navigation, several conventional LiDAR line extraction schemes have been reviewed and evaluated. Based on the comparison results a efficient line extraction approach is proposed and implemented for LiDAR navigation. This LMS based line feature extraction approach can significantly reduced the LiDAR processing time and improved the efficiency of the integration process.

To compare and analyse the performance of the novel approach against the conventional approach, a field experiment was conducted in Newcastle university. The experimental trajectory contains open an view environment, GPS signal blocked environment and narrow view environment. The field experiment results indicated that with the help of the dynamic integration scheme, the performance has been improved compare to the conventional Kalman filter based integration scheme. Due to systematic errors, the Kalman filter based approach contains a constant bias, and this bias takes time to be mitigated by the Kalman filter. This shows that the Kalman filter requires take time to converge. Nevertheless, the novel method can successfully provide an accurate, continuous and robust navigation approach in a challenging environment. These advantages proved that this new approach is more adaptive to vehicular communication applications.

Chapter 6

Conclusion and Future Works

GPS is a major satellite based navigation and positioning system and plays an important role in many applications. In vehicular communications, the precise, accurate, and continuous positioning and navigation information is in high demand. In urban environments, the low signal strength and the very dense multipath environment can significantly degrade the performance of GPS receivers or even deny the service completely. Furthermore, a highly dynamic environment is another challenge for the carrier tracking loop of GPS receivers, since the Doppler frequency shift will be increased.

To overcome these challenges, we proposed several novel methods in this thesis. To improve the acquisition ability of GPS signal processing, this thesis proposed a modified serial searching acquisition approach through a low cost dual polarization patch antenna to acquire LHCP GPS L1 band signals. The experimental results indicate that through this method extra satellites can be acquired in a very challenging environment. Furthermore, after successfully acquiring the GPS signal, two novel Kalman filter based carrier tracking loops are designed and implemented.

In order to obtain accurate and continuous positioning and navigation information, multiple sensors are required including a GPS receiver, IMU, and LiDAR. With three sensors, IMU and LiDAR require a series of algorithms to extract the position information. In order to reduce the computational cost of LiDAR mechanization, a novel line feature extraction approach has been proposed and implemented for LiDAR navigation. Then, a robust dynamic federated Kalman filter based multisensor integration approach is proposed and implemented at the end of this project.

6.1 Conclusion

This thesis firstly presented a novel step jumping serial searching acquisition method and designed a very low cost dual polarization patch antenna. Through simulation and field experiments, the results demonstrated that the novel searching approach is faster to the conventional approach and the acquisition results are superior than the commercial GPS receiver attached to an active antenna. The comparison results showed that the low cost dual polarization patch antennas that aim to collect the reflected LHCP GPS signals can be successfully implemented on both commercial GPS receivers and software based receivers. In the software GPS receiver, with the help of the step jumping serial searching acquisition method, the receiver is more sensitive to weak signals compared to the commercial GPS receiver which normally uses an FFT based parallel searching acquisition method.

Experimental results proved that the step jumping serial searching acquisition method can successfully acquire extra satellites via LHCP signals. The benefit of this novel acquisition method and antenna is to increase the total number of the acquired GPS satellite signals from both RHCP and LHCP antennas in order to improve the positioning accuracy under a very dense multipath environment.

In addition to designing and implementing a novel and efficient acquisition approach, this thesis also made a contribution to the carrier tracking loop design. The proposed carrier tracking loops consisted of a 3rd order PLL dynamically integrated with an adaptive Kalman filter and a 3rd order PLL dynamically integrated with an unscented Kalman filter. Firstly, the experiment compared the proposed 3rd order PLL integrated adaptive Kalman filter based carrier tacking loop against the conventional adaptive Kalman filter based carrier tracking loop in different aspects. The results indicated that the proposed tracking approach is superior in self adjusting and low C/N_o signal tracking. As the experimental results show, the C/N_o has been improved significantly compared to the conventional approach. Furthermore, for a large tracking bandwidth, the noise level of the output of the phase discriminator has also been reduced and that leads to the proposed tracking approach obtaining a better tracking accuracy.

To overcome the linear model requirement, an adaptive unscented Kalman filter and 3rd order PLL dynamically integrated carrier tracking loop is presented. As a quasi open loop, the unscented Kalman filter has a strong tracking ability

and makes the entire carrier tacking loop more robust. The parallel connected 3rd order PLL guarantees the tracking accuracy. Similar experiments were conducted and compared against an adaptive Kalman filter aided 3rd order PLL and the comparison results prove that the proposed approach can improve the carrier tracking capability. The carrier tracking trade-off issue between tracking bandwidth and accuracy has been tackled using the proposed approach and the field test confirmed that it can achieve a greater tracking range and still maintain the high accuracy. Comparison results indicated that this unscented Kalman filter integrated 3rd order PLL approach is more stable and robust with respect to phase variance and phase discriminator output. Phase variance comparison results showed that the proposed approach has a better steady-state response. Moreover, the phase discriminator output comparison results indicated that the proposed approach has a better noise rejection ability. This could also be observed in the C/N_o comparison.

For LiDAR navigation, the line feature extraction and mapping are the most important techniques. To improve the efficiency of the feature extraction, the thesis proposed a LMS based line extraction and mapping technique. Meanwhile, a GPS receiver, IMU and LiDAR integrated navigation system is designed by using a dynamically integrated federate Kalman filter approach. A field experiment is conducted to investigate the performance of the proposed approach. Experiment results indicated that the proposed GPS/INS/LiDAR navigation approach has a superior performance in terms of robustness and resilience. Via the dynamic information sharing factor within the proposed positioning approach, two subsystems can switch dynamically according to their performance, and because of this dynamic switching, the entire system can achieve more optimal results and provide precise and continuous navigation information.

In vehicular communication, especially in an urban scenario, the road condition can change rapidly and these changes can affect a particular sensor. Therefore, a robust and efficient multisensor navigation system is required. The proposed navigation method is reliable, robust and efficient. It can self adjust the contribution percentage of each subsystem and benefit the entire system to obtain precise continuous and consistent position and navigation information.

6.2 Future Work

The proposed modified serial searching approach is a member of the serial searching family, therefore, the processing speed is slower than parallel searching although it is more sensitive to a low SNR signal. However, in vehicular communication or highly dynamic environments, a rapid response and re-acquisition is equally important. The future work should focus on designing a more efficient acquisition approach and still retaining the same sensitivity level.

As we know, a highly dynamic environment can generate a strong Doppler effect and degrade the performance of the carrier tracking loop. INS or IMU can measure the inertial parameter and estimate the Doppler effect. With prior information of the Doppler effect, the performance of the carrier tracking loop can be significantly improved, therefore, the future research should also focus on the INS aided carrier tracking loop design.

Position information like latitude and longitude from the GPS receiver is restricted by the number of visible satellites. With less than 4 visible satellites, the GPS receiver will not be able to provide positioning information. However, instead of using positioning information, pseudorange, which is a distance measurement between the satellite and the receiver, is available even when there is only one satellite. By fusing the GPS pseudorange measurement with IMU and LiDAR one can achieve a more robust and accurate positioning result. Furthermore, besides GPS, IMU, and LiDAR, a cellular signal is another valuable location source which can provide a relevant position. Now, the world is entering an era of 5G, the cellular link will be more reliable and fast, and future research could also focus on the fusion of cellular signals for positioning and navigation.

For research purposes, in this project, all the collected data and algorithm implementations are achieved via post processing. Future research could focus on real time processing platform design and implementation.

References

[1] S. New, "Congestion crisis warning as vehicle numbers soar by 2.5 million," Saturday 28 July 2018, last accessed 13 September 2018. [Online]. Available: https://news.sky.com/story/congestion-crisis-warning-as-vehicle-numbers-soar-by-25-million-11451965

[2] W. H. Organization, "Road traffic injuries," 19 February 2018, last accessed 13 September 2018. [Online]. Available: http://www.who.int/news-room/fact-sheets/detail/road-traffic-injuries

[3] J. Andersen and S. Sutcliffe, "Intelligent transport systems (its)-an overview," *IFAC Proceedings Volumes*, vol. 33, no. 18, pp. 99–106, 2000.

[4] S. Li, Q.-m. Yi, M. Shi, and Q. Chen, "Highly sensitive weak signal acquisition method for gps/compass," in *2014 International Joint Conference on Neural Networks (IJCNN)*. IEEE, 2014, pp. 1245–1249.

[5] J. Wu and Y. Hu, "The study on gps signal acquisition algorithm in time domain," in *2008 4th International Conference on Wireless Communications, Networking and Mobile Computing*. IEEE, 2008, pp. 1–3.

[6] K. Palamartchouk, P. Clarke, and R. Tiwari, "Dual-polarisation gnss observations for multipath mitigation and better high-precision positioning," 2015.

[7] M. Usman and D. Armitage, "Acquisition of reflected gps signals for remote sensing applications," in *Advances in Space Technologies, 2008. ICAST 2008. 2nd International Conference on*. IEEE, 2008, pp. 131–136.

[8] E. Kaplan and C. Hegarty, *Understanding GPS: principles and applications*. Artech house, 2005.

[9] X. Niu, B. Li, N. I. Ziedan, W. Guo, and J. Liu, "Analytical and simulation-based comparison between traditional and kalman filter-based phase-locked loops," *GPS solutions*, vol. 1, no. 21, pp. 123–135, 2016.

[10] M. L. Psiaki and H. Jung, "Extended kalman filter methods for tracking weak gps signals," in *ION GPS 2002: 15 th International Technical Meeting of the Satellite Division of The Institute of Navigation*, 2002.

[11] N. I. Ziedan and J. L. Garrison, "Extended kalman filter-based tracking of weak gps signals under high dynamic conditions," in *Proceedings of ION GNSS*, vol. 2004, 2004, pp. 20–31.

[12] S. Han, W. Wang, X. Chen, and W. Meng, "Design and capability analyze of high dynamic carrier tracking loop based on ukf," in *Proceedings of the 23rd International Technical Meeting of The Satellite Division of the Institute of Navigation (ION GNSS 2010)*, 2001, pp. 1960–1966.

[13] G. Chang, "Loosely coupled ins/gps integration with constant lever arm using marginal unscented kalman filter," *The Journal of Navigation*, vol. 67, no. 3, pp. 419–436, 2014.

[14] Y. Liu, X. Fan, C. Lv, J. Wu, L. Li, and D. Ding, "An innovative information fusion method with adaptive kalman filter for integrated ins/gps navigation of autonomous vehicles," *Mechanical Systems and Signal Processing*, vol. 100, pp. 605–616, 2018.

[15] W. Fu-Mei and Y. Yuan-xi, "An extended adaptive kalman filtering in tight coupled gps/ins integration," *Survey Review*, vol. 42, no. 316, pp. 146–154, 2010.

[16] H. Yu, Z. Li, J. Wang, and H. Han, "Data fusion for a gps/ins tightly coupled positioning system with equality and inequality constraints using an aggregate constraint unscented kalman filter," *Journal of Spatial Science*, pp. 1–22, 2018.

[17] M. Ilyas, Y. Yang, Q. S. Qian, and R. Zhang, "Low-cost imu/odometer/gps integrated navigation aided with two antennae heading measurement for land vehicle application," in *Control and Decision Conference (CCDC), 2013 25th Chinese*. IEEE, 2013, pp. 4521–4526.

[18] P. Zhang, J. Gu, E. E. Milios, and P. Huynh, "Navigation with imu/gps/digital compass with unscented kalman filter," in *Mechatronics and Automation, 2005 IEEE International Conference*, vol. 3. IEEE, 2005, pp. 1497–1502.

[19] J. Tang, Y. Chen, X. Niu, L. Wang, L. Chen, J. Liu, C. Shi, and J. Hyyppä, "Lidar scan matching aided inertial navigation system in gnss-denied environments," *Sensors*, vol. 15, no. 7, pp. 16 710–16 728, 2015.

[20] Y. Gao, S. Liu, M. Atia, and A. Noureldin, "Ins/gps/lidar integrated navigation system for urban and indoor environments using hybrid scan matching algorithm," *Sensors*, vol. 15, no. 9, pp. 23 286–23 302, 2015.

[21] Y. Li, C. Rizos, J. Wang, P. Mumford, and W. Ding, "Sigma-point kalman filtering for tightly coupled gps/ins integration," *Navigation*, vol. 55, no. 3, pp. 167–177, 2008.

[22] K. Kim and C. G. Park, "Feedforward unscented kalman filter for ins/gps tightly coupled integration system," *IFAC Proceedings Volumes*, vol. 40, no. 7, pp. 545–550, 2007.

[23] Y. Li, J. Wang, C. Rizos, P. Mumford, and W. Ding, "Low-cost tightly coupled gps/ins integration based on a nonlinear kalman filtering design," in *Proceedings of ION National Technical Meeting*, 2006, pp. 18–20.

[24] G. Hu, S. Gao, and Y. Zhong, "A derivative ukf for tightly coupled ins/gps integrated navigation," *ISA transactions*, vol. 56, pp. 135–144, 2015.

[25] S. Charkhandeh, M. Petovello, and G. Lachapelle, "Performance testing of a real-time software-based gps receiver for x86 processors," in *ION GNSS*, 2006, pp. 2313–2320.

[26] W. Gurtner and L. Estey, "Rinex-the receiver independent exchange format-version 3.00," *Astronomical Institute, University of Bern and UNAVCO, Bolulder, Colorado.*, 2007.

[27] R.-S. IGS, "Rinex-the receiver independent exchange format (version 3.03)," 2013.

[28] G. A. Elango, G. Sudha, and B. Francis, "Weak signal acquisition enhancement in software gps receivers–pre-filtering combined post-correlation detection approach," *Applied Computing and Informatics*, vol. 13, no. 1, pp. 66–78, 2017.

[29] J. Farrell, "Ins error state dynamic equations," in *Aided navigation: GPS with high rate sensors*. United States of America: McGraw-Hill, Inc., 2008, ch. 11.4, pp. 392–396.

[30] J. Diebel, "Representing attitude: Euler angles, unit quaternions, and rotation vectors," *Matrix*, vol. 58, no. 15-16, pp. 1–35, 2006.

[31] P. Berner, R. Toms, K. Trott, F. Mamaghani, D. Shen, C. Rollins, and E. Powell, "Technical concepts: Orientation, rotation, velocity and acceleration, and the srm," *TENA (Test & Training Enabling Architecture) project by SEDRIS*, vol. 21, 2008.

[32] Y.-B. Jia, "Quaternions and rotations," *Com S*, vol. 477, no. 577, p. 15, 2008.

[33] O. J. Woodman, "An introduction to inertial navigation," University of Cambridge, Computer Laboratory, Tech. Rep., 2007.

[34] I. Definition, "Relationships with local geodetic systems," *National Imagery and Mapping Agency, Department of Defense World Geodetic System*, 1984.

[35] D. Manandhar, R. Shibasaki, and H. Torioto, "Prototype software-based receiver for remote sensing using reflected gps signals," in *ION Proceedings, GNSS*, 2005.

[36] F. Principe, G. Bacci, F. Giannetti, and M. Luise, "Software-defined radio technologies for gnss receivers: A tutorial approach to a simple design and implementation," *International Journal of Navigation and Observation*, vol. 2011, 2011.

[37] J. B.-Y. Tsui, *Fundamentals of global positioning system receivers: a software approach*. John Wiley & Sons, 2005, vol. 173.

[38] Q. Lei and L. Lei, "Gps signal acquisition based on fft," in *Information Technology and Computer Science (ITCS), 2010 Second International Conference on*. IEEE, 2010, pp. 110–113.

[39] J. Mondal, S. K. Ray, M. S. Alam, and M. M. Rahman, "Design smart antenna by microstrip patch antenna array," *International Journal of Engineering and Technology*, vol. 3, no. 6, p. 675, 2011.

[40] J. Aguilar, M. Beadle, P. Thompson, and M. Shelley, "The microwave and rf characteristics of fr4 substrates," in *Low Cost Antenna Technology (Ref. No. 1998/206), IEE Colloquium on.* IET, 1998, pp. 2–1.

[41] R. Garg, *Microstrip antenna design handbook.* Artech house, 2001.

[42] D. Bonefačić, J. Bartolić, and M. Germ, "Dual-band electronically switchable shorted patch antenna," *Frequenz*, vol. 61, no. 3-4, pp. 71–73, 2007.

[43] K. S. Aung and S. S. Mon, "Comparison of rectangular and truncated rectangular patch antenna for ku-band."

[44] M. L. Psiaki, "Smoother-based gps signal tracking in a software receiver," in *Proceedings of ION GPS*, vol. 2001, 2001, pp. 2900–2913.

[45] A. UmaMageswari, J. J. Ignatious, and R. Vinodha, "A comparitive study of kalman filter, extended kalman filter and unscented kalman filter for harmonic analysis of the non-stationary signals," *International Journal of Scientific & Engineering Research*, vol. 3, no. 7, pp. 1–9, 2012.

[46] Y. Shi and D. Yan, "A research on the relationship between kalman filter and phase locked loop," in *Control and Decision Conference (CCDC), 2016 Chinese.* IEEE, 2016, pp. 5106–5110.

[47] J.-H. Won, T. Pany, and B. Eissfeller, "Characteristics of kalman filters for gnss signal tracking loop," *IEEE Transactions on Aerospace and Electronic Systems*, vol. 48, no. 4, pp. 3671–3681, 2012.

[48] A. Patapoutian, "On phase-locked loops and kalman filters," *IEEE Transactions on Communications*, vol. 47, no. 5, pp. 670–672, 1999.

[49] P. W. Ward, "Performance comparisons between fll, pll and a novel fll-assisted-pll carrier tracking loop under rf interference conditions," in *ION GPS-98*, 1998, pp. 783–795.

[50] P. W. Ward, J. W. Betz, C. J. Hegarty *et al.*, "Satellite signal acquisition, tracking, and data demodulation," *Understanding GPS principles and applications*, vol. 5, pp. 174–175, 2006.

[51] E. Kaplan and C. Hegarty, *Understanding GPS: principles and applications*. Artech house, 2005.

[52] D. Gebre-Egziabher, A. Razavi, P. Enge, J. Gautier, D. Akos, S. Pullen, and B. Pervan, "Doppler aided tracking loops for srgps integrity monitoring," in *Proceedings of the 16th International Technical Meeting of the Satellite Division of The Institute of Navigation (ION GPS/GNSS 2003)*, 2001, pp. 2562–2571.

[53] M. Irsigler and B. Eissfeller, "Pll tracking performance in the presence of oscillator phase noise," *GPS solutions*, vol. 5, no. 4, pp. 45–57, 2002.

[54] D. B. Sullivan, D. W. Allan, D. A. Howe, and F. L. Walls, *Characterization of clocks and oscillators*. National Institute of Standards and Technology Technical Note, 1990.

[55] R. E. Kalman, "A new approach to linear filtering and prediction problems," *Journal of basic Engineering*, vol. 82, no. 1, pp. 35–45, 1960.

[56] R. G. Brown, P. Y. Hwang *et al.*, *Introduction to random signals and applied Kalman filtering*. Wiley New York, 1992, vol. 3.

[57] X. Sun, H. Qin, and J. Niu, "Comparison and analysis of gnss signal tracking performance based on kalman filter and traditional loop," *WSEAS Trans Signal Process*, vol. 9, no. 3, pp. 99–108, 2013.

[58] G. Yao, W. Wenqi, and H. Xiaofeng, "High dynamic carrier phase tracking based on adaptive kalman filtering," in *Control and Decision Conference (CCDC), 2011 Chinese*. IEEE, 2011, pp. 1245–1249.

[59] J. Sasiadek, Q. Wang, and M. Zeremba, "Fuzzy adaptive kalman filtering for ins/gps data fusion," in *Intelligent Control, 2000. Proceedings of the 2000 IEEE International Symposium on*. IEEE, 2000, pp. 181–186.

[60] R. Mehra, "On the identification of variances and adaptive kalman filtering," *IEEE Transactions on automatic control*, vol. 15, no. 2, pp. 175–184, 1970.

[61] N. A. Carlson, "Federated filter for fault-tolerant integrated navigation systems," in *Position Location and Navigation Symposium, 1988. Record. Navigation into the 21st Century. IEEE PLANS'88., IEEE.* IEEE, 1988, pp. 110–119.

[62] J. K. Uhlmann, "Simultaneous map building and localization for real time applications," Technical report, University of Oxford, 1994. Transfer thesis, Tech. Rep., 1994.

[63] S. J. Julier and J. K. Uhlmann, "New extension of the kalman filter to nonlinear systems," in *Signal processing, sensor fusion, and target recognition VI*, vol. 3068. International Society for Optics and Photonics, 1997, pp. 182–194.

[64] E. A. Wan and R. Van Der Merwe, "The unscented kalman filter for nonlinear estimation," in *Adaptive Systems for Signal Processing, Communications, and Control Symposium 2000. AS-SPCC. The IEEE 2000.* Ieee, 2000, pp. 153–158.

[65] ——, "The unscented kalman filter," *Kalman filtering and neural networks*, pp. 221–280, 2001.

[66] S. J. Julier, J. K. Uhlmann, and H. F. Durrant-Whyte, "A new approach for filtering nonlinear systems," in *American Control Conference, Proceedings of the 1995*, vol. 3. IEEE, 1995, pp. 1628–1632.

[67] R. Mehra, "Approaches to adaptive filtering," *IEEE Transactions on automatic control*, vol. 17, no. 5, pp. 693–698, 1972.

[68] R. Tiwari, H. Strangeways, and S. Skone, "Modeling the effects of ionospheric scintillation on gps carrier phase tracking using high rate tec data," in *26th International Technical Meeting of The Satellite Division of the Institute of Navigation (ION GNSS+ 2013), Nashville, Tenn*, 2013, pp. 2480–2488.

[69] J. Yin, R. Tiwari, and M. Johnston, "Low-cost dual polarized gps antenna for effective signal acquisition in multipath environment," in *Navigation Conference (ENC), 2017 European.* IEEE, 2017, pp. 359–365.

[70] B. Parkinson and S. J, *Global Positioning System, Volume 1 - Theory and Applications.* American Institute of Aeronautics and Astronautics, 1996.

[71] A. Angrisano, "Gnss/ins integration methods," *Dottorato di ricerca (PhD) in Scienze Geodetiche e Topografiche Thesis, Universita'degli Studi di Napoli PARTHENOPE, Naple*, vol. 21, 2010.

[72] G. Falco, G. A. Einicke, J. T. Malos, and F. Dovis, "Performance analysis of constrained loosely coupled gps/ins integration solutions," *Sensors*, vol. 12, no. 11, pp. 15 983–16 007, 2012.

[73] J. L. Marins, X. Yun, E. R. Bachmann, R. B. McGhee, and M. J. Zyda, "An extended kalman filter for quaternion-based orientation estimation using marg sensors," in *Proceedings 2001 IEEE/RSJ International Conference on Intelligent Robots and Systems. Expanding the Societal Role of Robotics in the the Next Millennium (Cat. No. 01CH37180)*, vol. 4. IEEE, 2001, pp. 2003–2011.

[74] R. G. Valenti, I. Dryanovski, and J. Xiao, "A linear kalman filter for marg orientation estimation using the algebraic quaternion algorithm," *IEEE Transactions on Instrumentation and Measurement*, vol. 65, no. 2, pp. 467–481, 2016.

[75] R. Li, J. Liu, L. Zhang, and Y. Hang, "Lidar/mems imu integrated navigation (slam) method for a small uav in indoor environments," *2014 DGON Inertial Sensors and Systems (ISS)*, pp. 1–15, 2014.

[76] T. Pavlidis and S. L. Horowitz, "Segmentation of plane curves," *IEEE transactions on Computers*, vol. 100, no. 8, pp. 860–870, 1974.

[77] G. A. Borges and M.-J. Aldon, "Line extraction in 2d range images for mobile robotics," *Journal of intelligent and Robotic Systems*, vol. 40, no. 3, pp. 267–297, 2004.

[78] A. Siadat, A. Kaske, S. Klausmann, M. Dufaut, and R. Husson, "An optimized segmentation method for a 2d laser-scanner applied to mobile robot navigation," in *Proceedings of the 3rd IFAC symposium on intelligent components and instruments for control applications*. Citeseer, 1997, pp. 153–158.

[79] M. A. Fischler and R. C. Bolles, "Random sample consensus: a paradigm for model fitting with applications to image analysis and automated cartography," *Communications of the ACM*, vol. 24, no. 6, pp. 381–395, 1981.

[80] A. Soloviev, D. Bates, and F. Van Graas, "Tight coupling of laser scanner and inertial measurements for a fully autonomous relative navigation solution," *Navigation*, vol. 54, no. 3, pp. 189–205, 2007.

[81] M. Kok, J. D. Hol, and T. B. Schön, "Using inertial sensors for position and orientation estimation," *arXiv preprint arXiv:1704.06053*, 2017.

[82] N. Trawny and S. I. Roumeliotis, "Indirect kalman filter for 3d attitude estimation," *University of Minnesota, Dept. of Comp. Sci. & Eng., Tech. Rep*, vol. 2, p. 2005, 2005.

[83] D. Gebre-Egziabher, G. H. Elkaim, J. Powell, and B. W. Parkinson, "A gyro-free quaternion-based attitude determination system suitable for implementation using low cost sensors," in *Position Location and Navigation Symposium, IEEE 2000.* IEEE, 2000, pp. 185–192.

[84] R. G. Valenti, I. Dryanovski, and J. Xiao, "Keeping a good attitude: A quaternion-based orientation filter for imus and margs," *Sensors*, vol. 15, no. 8, pp. 19 302–19 330, 2015.

[85] X. Jing, J. Cui, H. He, B. Zhang, D. Ding, and Y. Yang, "Attitude estimation for uav using extended kalman filter," in *Control And Decision Conference (CCDC), 2017 29th Chinese.* IEEE, 2017, pp. 3307–3312.

[86] S. Shan, Z. Hou, and J. Wu, "Linear kalman filter for attitude estimation from angular rate and a single vector measurement," *Journal of Sensors*, vol. 2017, 2017.

[87] V. Renaudin and C. Combettes, "Magnetic, acceleration fields and gyroscope quaternion (magyq)-based attitude estimation with smartphone sensors for indoor pedestrian navigation," *Sensors*, vol. 14, no. 12, pp. 22 864–22 890, 2014.

[88] M. Xu, N. Fan, and Z. Wang, "Study on extended kalman filtering for attitude estimation of micro flight vehicle," in *Measuring Technology and Mechatronics Automation (ICMTMA), 2011 Third International Conference on*, vol. 3. IEEE, 2011, pp. 457–460.

[89] W. Breckenridge, "Quaternions proposed standard conventions," *Jet Propulsion Laboratory, Pasadena, CA, Interoffice Memorandum IOM*, pp. 343–79, 1999.

[90] S. Kwanmuang, L. Ojeda, and J. Borenstein, "Magnetometer-enhanced personal locator for tunnels and gps-denied outdoor environments," in *Sensors, and Command, Control, Communications, and Intelligence (C3I) Technologies for Homeland Security and Homeland Defense X*, vol. 8019. International Society for Optics and Photonics, 2011, p. 80190O.

[91] X. T. B.V., *MTi User Manual*, Xsens North America, Inc, Pantheon 6a P.O. Box 559 7500 AN Enschede The Netherlands, Dec. 2017.